Universidad de La Laguna

Master's Degree in Astrophysics
2021-2022

The K-band spectrum of nearby Type 2 Quasars

Miguel Coloma Puga

Tutors: Cristina Ramos Almeida & José Antonio Acosta Pulido

San Cristóbal de La Laguna, 2022

Abstract

Las galaxias activas son aquellas caracterizadas por una fuerte emisión electromágnetica procedente de sus núcleos, que se denominan núcleos galácticos activos o AGNs. Esta emisión se produce en un enorme rango de longitudes de onda, desde ondas de radio a rayos X. Los núcleos de estas galaxias están compuestos por un agujero negro supermasivo rodeado de un disco de acreción a muy alta temperatura, y en ocasiones pueden presentar jets extendidos de materia relativista. Los AGNs son de gran importancia en el campo de la evolución galáctica, y actualmente se piensa que la mayoría de galaxias atraviesan fases de actividad nuclear. Este tipo de galaxias se clasifican según su emisión en radio, su luminosidad bolométrica y sus caraterísticas espectrales. Las diferencias observadas en los distintos tipos de AGN se han intentado explicar desde una perspectiva de unificación; variando el ángulo que forman el disco y el toro con nuestra línea de visión, se observarán los distintos tipos de AGN.

Los discos de acreción presentes en estas galaxias representan unos fenómenos altamente energéticos los cuales tienen un profundo efecto en la evolución de sus galaxias anfitrionas y, de hecho, se han observado correlaciones claras entre parámetros del bulbo y la masa del agujero negro central. La energía emitida por el disco de acreción da lugar a la aparición de vientos, enormes masas de gas que se separan del medio interestelar, impulsados o bien por presión radiativa causada por el propio disco de acreción o bien por los jets de materia relativista.

Se han observado una variedad de efectos debidos a los vientos; ya sea promoviendo la formación estelar al presurizar burbujas de gas frío y aumentando la fragmentación, o previniendo e incluso deteniendo la formación estelar al calentar y perturbar el ISM. Las dificultades y suposiciones necesarias para medir los parámetros característicos de los outflows hacen que el estudio de los mismos sea extremadamente complejo, a la vez que un campo de la astrofísica en constante movimiento y evolución. Los vientos pueden estudiarse en varias fases de gas; ionizado, atómico neutro y molecular. Dado que cada una de estas fases posee un espectro de emisión que cubre distintas partes del espectro electromagnético, la caracterización completa de los mismos suele requerir un enfoque en varias bandas espectrales.

En este contexto, los cuásares de tipo 2 o QSO2 son extremadamente relevantes. La región que emite líneas anchas o BLR está oscurecida en este tipo de AGN, por lo que las componentes anchas observadas se deben a la presencia de gas perturbado, es decir, vientos. Este proyecto hace uso de observaciones de una muestra de 40 AGNs en la banda K tomadas con el Espectrógrafo Multiobjeto Infra-Rojo (EMIR), para caracterizar simultáneamente las fases ionizada y molecular de sus vientos.

Los AGNs seleccionados para este proyecto son un subconjunto de QSOFEED. Los objetos se seleccionaron en base a su luminosidad bolométrica ($L_{Bol} > 10^{45.6}\ erg\ s^{-1}$) y su redshift (z<0.14). Los espectros de la muestra completa fueron reducidos y calibrados en flujo, y 6 de estos objetos se eligieron en base a la presencia de componentes anchas en líneas ionizadas y presencia de líneas moleculares para el estudio en profundidad de sus espectros. Las observaciones se llevaron a cabo usando el instrumento EMIR, instalado en el Gran Telescopio Canarias, situado en el Observatorio del Roque de los Muchachos. Los datos se obtuvieron desde mayo del 2018 a junio del 2020, divididos en cuatro semestres de observaciones. Todos los espectros se tomaron en el filtro K, que extiende desde 1.97 μm a 2.43 μm. Para los 6 objetos elegidos, estas observaciones se complementaron con espectros en el rango ópticos extraídos del Sloan Digital Sky Survey.

La reducción de datos consistió en la corrección de efectos de flat-field y la substracción del cielo, que se llevaron a cabo con un script de Python, el cual hace uso de la implementación de IRAF en este lenguaje, *Pyraf*, y el módulo de *lirisdr* de la misma. Los espectros se extrajeron utilizando dos tamaños de apertura; una del tamaño del seeing de la observación y otra de 3", el cual es el tamaño utilizado en las observaciones espectroscópicas de SDSS. La calibración en flujo también se llevo a cabo usando *Pyraf*, así como la corrección por absorción telúrica, para la cual se utilizaron tanto estrellas de comparación como modelos teóricos generados por el software *Skycalc*.

La muestra completa presenta una gran variedad en las características espectrales de los objetos, desde espectros con pocas líneas de emisión estrechas a espectros muy ricos en líneas, las cuales presentan componentes con variedad de anchuras y longitudes centrales. También observamos variedad en la forma del continuo de los objetos: algunos son completamente planos mientras que otros caen conforme aumenta la longitud de onda. Como cabe esperar en la banda K, en estos espectros observamos líneas de ionización baja (Pa α, Br γ y δ) y líneas de alta ionización o coronales ([SiVI] y [SiX]), asi como líneas moleculares debidas a transiciones cuadrupolares de la molécula de H_2.

La caracterización de vientos requiere un análisis multicomponente de las líneas de emisión, ya que las diferentes líneas y sus componentes se mezclan dando lugar a perfiles complejos, compuestos de la suma de varios perfiles gaussianos. Estos perfiles se caracterizaron utilizando el módulo *modeling* de Astropy para Python. En primer lugar se ajustaron las líneas de los espectros de SDSS, ya que presentan líneas aisladas cuyas componentes son más sencillas de modelar sin información a priori. A partir de los parámetros cinemáticos (FWHM y velocidad relativa de las componentes) obtenidos en estos ajustes se analizaron las líneas ionizadas observadas en el infrarrojo. Debido a que no se observan en el óptico, las líneas moleculares se analizaron sin información previa sobre su cinemática. La velocidad relativa de las distintas componentes del gas en nuestra línea de visión se estima haciendo uso del efecto Doppler, para el cual consideramos que la componente estrecha de las líneas ionizadas marca el sistema en reposo dentro de la galaxia observada.

Tras analizar los distintos perfiles de las líneas de emisión detectadas, encontramos vientos en todos los objetos en al menos una fase del gas. Estos vientos presentan distintos niveles de perturbación, con anchuras desde 500 km/s a 2600 km/s, y velocidades desde 70 km/s a 980 km/s. Encontramos vientos ionizados en todos los objetos,

mientras que solo detectamos un viento molecular en un solo objeto, y de manera tentativa, posiblemente debido a la baja señal que presentan las líneas moleculares, lo cual dificulta en gran medida la detección de componentes anchas de baja amplitud. Observamos que cada uno de los objetos presenta tanto un número de vientos distinto como variedad en las características de los mismos, a la vez que estudiamos las ligaduras y parametrizaciones que es necesario llevar a cabo en los ajustes de las distintas líneas. Aprovechamos también dos objetos que ya se han estudiado, uno de ellos en el NIR y otro en el óptico, para comparar nuestros resultados y comprobar que nuestro procedimiento ha sido correcto.

La continuación de este proyecto se basará en las medidas de la masa del viento, el ritmo de expulsión de masa del viento y la energía cinética del mismo. Estas medidas se pueden llevar a cabo con los datos que ya tenemos, utilizando líneas de los espectros ópticos en combinación con modelos de emisividad y fotoionización para estimar la densidad del viento, a la vez que los espectros de EMIR se pueden utilizar para constreñir la extensión del mismo.

Contents

1 Introduction

This section intends to give a comprehensive overview on active galactic nuclei, from their discovery and classification to their relevance in modern astrophysics, as well as an introduction into the kinematics and effects of gas outflows and the aims of this project.

1.1 Active galaxies: definition and history

Active galaxies are defined as galaxies characterized by strong emission from their cores, of the order of and sometimes larger than the emission from the rest of the galaxy. This emission ranges from radio to X-rays, both in the continuum and in emission lines, and can be variable. The nuclei of these galaxies, from here on referred to as AGN, are primarily comprised of a super massive black hole and an accretion disk around it which, formed by infalling material that heats up via friction, becomes the main source of AGN emission. Due to their highly energetic nature, they can also host extended jets of relativistic matter.

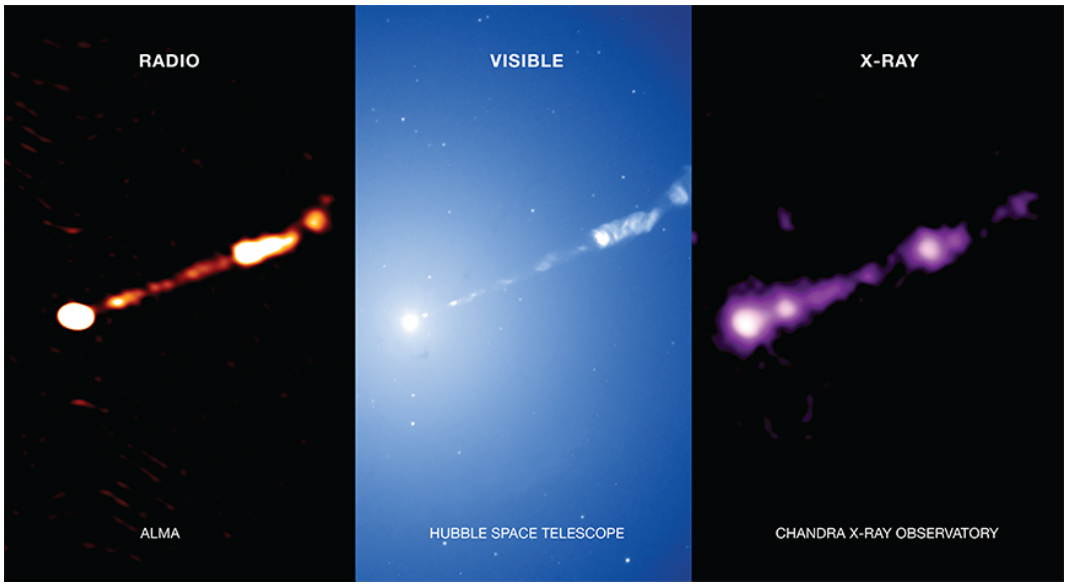

Figure 1: Multi-wavelength images of the M87 galaxy, taken from https://chandra.si.edu/photo/2021/m87/. Extended jet emission is observed at all wavelengths.

Even if only a relatively small fraction of galaxies in the local universe show signs of current nuclear activity, it has been hypothesized that all massive galaxies go through a short (0.1-100 MYr, see Schawinski et al., 2015 [1]) active phase at a certain point in their evolution. One could imagine such violent phenomena would have long-lasting aftereffects on their host galaxies' characteristics; as such, unveiling how galaxies and their central SMBH co-evolve, and how AGN emission affects their host galaxies is of the utmost importance in the field of galaxy evolution.

While observation of active galaxies hails as far back as the early 19th century, with the discovery of bright emission lines in the spectra of galaxies, these only become a true object of study with the birth of radio astronomy. Comparing radio sources to their optical counterparts, some of them were clearly extended objects, but others appeared to be point-like, mimicking stars. They, nonetheless, showed broad emission lines and flat spectra, meaning they couldn't possibly be so. As such, the name quasi-stellar object (QSO or quasar for short) was adopted for sources of this type.

1.2 Classification of AGN

Active galaxies are a very varied group of astronomical objects, particularly when we consider the wavelength range of the radiation they emit, from X-rays to radio. Based on the differences in their spectra (see figure 2 for examples), namely whether or not there is emission in radio wavelengths, their bolometric luminosity and the characteristics of their spectral features, active galaxies are classified in two main groups; radio-loud and radio-quiet, and within each of these groups, there is further classification in accordance to the rest of their characteristics.

1.2.1 Radio-quiet AGN

- **Seyfert galaxies:** Seyfert galaxies are name after Carl K. Seyfert, who pioneered the study of galaxies with active nuclei (C. Seyfert, 1943 [2]). While the nucleus of a Seyfert galaxy is observable, so is the rest of the stellar

component, as these nuclei aren't bright enough to drown out the rest of the galaxy's emission. As such, their spectra contain the typical emission lines characteristic of active nuclei as well as absorption features caused by stars. There exists a subdivision of type 1 and type 2 Seyfert galaxies; type 1 galaxies show strong and broad emission lines, while type 2 only present narrow lines.

- **Radio-quiet Quasars:** They are similar to Seyfert galaxies but differ in their nuclear emission, as its strength causes the absorption lines from the stellar component to be much weaker and sometimes undetectable. As Seyfert galaxies, they are also divided in 2 types, based on whether the permitted lines contain a broad component (Reyes et al., 2008 [3]).
- **Low Ionization Nuclear Emission-line Regions:** Also known as LINERs, these objects show nuclear emission characterized by enhanced narrow lines of weakly ionized atomic species. While some of these objects are confirmed as AGN, particularly those that show X-ray emission (González-Martín et al., 2009[4]), some objects classified as LINERs might not be active galaxies.

1.2.2 Radio-loud AGN

- **Radio galaxies:** These are analogous to Seyfert galaxies, albeit with radio emission in their spectrum. As such, they are also subdivided in Broad Line Radio Galaxies and Narrow Line Radio Galaxies (BLRGs and NLRGs) based on their spectral features. The brightest of these galaxies might be relatively dim radio-loud quasars.
- **Radio-loud quasars:** They behave identically to radio-quiet quasars with the addition of radio emission. This emission can be both nuclear as well as extended. The extended emission comes from jets of relativistic material which originate from the nucleus and generate synchrotron radiation as they move in the presence of a magnetic field. As it stands, there appears to be a correlation between BH mass and radio emission, as radio-loud quasars are found to be systematically larger than their radio-quiet counterparts (McLure & Jarvis, 2004)[5].
- **Blazars:** These objects are characterized by violent and rapid variations in their continuum emission. They usually show no spectral features, neither emission nor absorption, due to relativistic effects caused by a beamed component observed near the LOS. This beaming generates a similar effects as quasars do with stellar emission lines, drowning out the spectral features. BL Lac objects have a smooth continuum, while OVV quasars or Flat Spectrum Radio-Quasars (FSRQs) can show some emission lines, accompanied by variability.

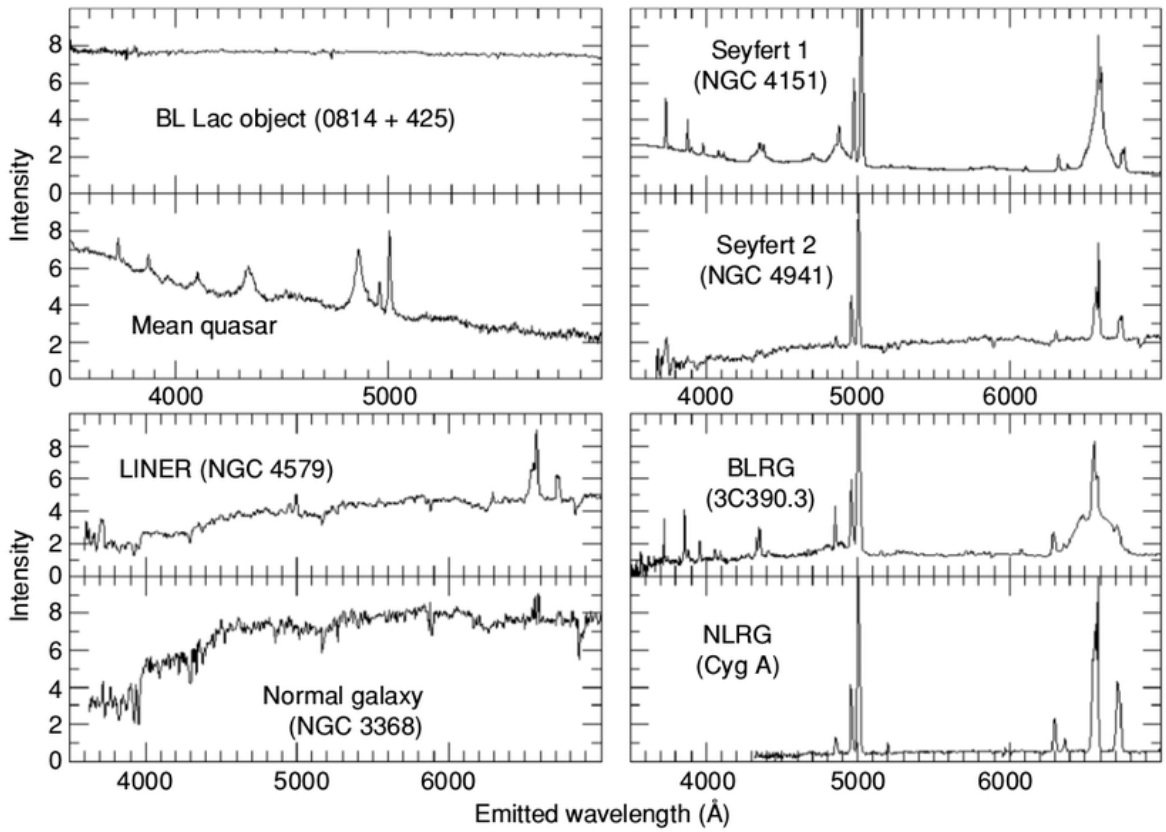

Figure 2: Examples of spectra of the different AGN types and a non-active galaxy for reference, taken from https://www.researchgate.net/figure/Typical-optical-spectra-of-AGN_fig1_306344484. Credit: Bill Keel

1.2.3 Unified model of AGN

One of the most widespread ways of understanding and justifying the differences between AGN types is the unified scheme (first proposed by Antonucci, 1993 [6] and Urry & Padovani, 1995, [7]). It suggests that the SMBH-powered accretion disk is indeed common to all AGN classes, and the perceived differences stem from observing these structures at a variety of angles. The paradigm of AGN structure at that time consisted of a central black hole, an obscuring and dense dusty torus encircling the black hole, gas clouds above and below the torus, and at times, jets of outflowing material. These clouds were divided in broad and narrow line regions (BLR and NLR respectively), based on their gas kinematics. This sort of axissymmetric structure would present considerably different appearances depending on the viewing angle, owing to the anisotropic character of AGN radiation.

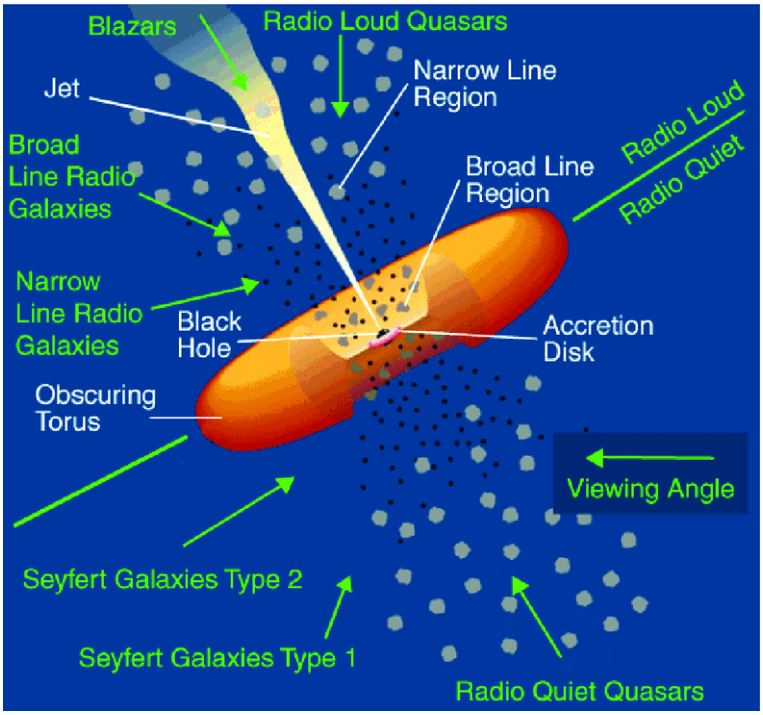

Figure 3: Representation of the unified model proposed by and taken from Urry and Padovani (1995). In this scheme, the presence of the jet and the viewing angle are the deciding factor in which type of AGN is observed.

In this scheme, radio loud quasars would be those presenting jets, and depending on the viewing angle of the observer, they could be identified as blazars (if the jet points towards the earth), type 1 quasars if the BLR and accretion disk were visible, type 2 quasars if only the NLR was visible (edge-on view), and BLRGs or NLRGs if their luminosity was lower. While this sort of unified model is certainly appealing from a physical standpoint, it is not without detriment. Besides the issues listed by Urry and Padovani themselves, such as the linear size of jets and dependence of quasar fraction with redshift, recent works (e.g. Chen & Hwang, 2017 [8]) show a relation between AGN types and their host galaxies, and a possible path to evolution from type 1 to type 2 AGN.

1.3 Gas kinematics of active galaxies: outflows

AGN-powered accretion disks represent massively powerful engines, be it via mechanical (jets) or radiative emission of energy. These enormous amounts of energy go beyond outshining their host galaxies, and are thought to play an essential role in regulating star formation, but the true relationships between different types of feedback, star formation and galaxy evolution are still to be fully understood.

SMBHs have been thought to co-evolve with their host galaxies, showing particularly strong correlations in the case of SMBH mass and bulge velocity dispersion, mass and luminosity (Kormendy and Ho, 2013 [9]). As it stood, it was hypothesized that the black hole and bulge regulated each other's growth, in a sort of feedback loop. It was also found that most of the central black hole mass was accreted during active phases, pointing to an AGN phase being common for most bulge-hosting galaxies (Shankar et al., 2004 [10]). While there is evidence for less related types of co-evolution, interaction of AGN with the interstellar medium can explain these observed relations via a strong co-evolution of SMBH and galaxy. For example, the observed molecular and ionized outflows of gas observed in active galaxies are too powerful to be driven by just the effect of SNe, highlighting the need for some type of AGN feedback, and simulations lacking AGN feedback produce universes with far too many star forming massive galaxies (Dubois et al., 2016 [11]).

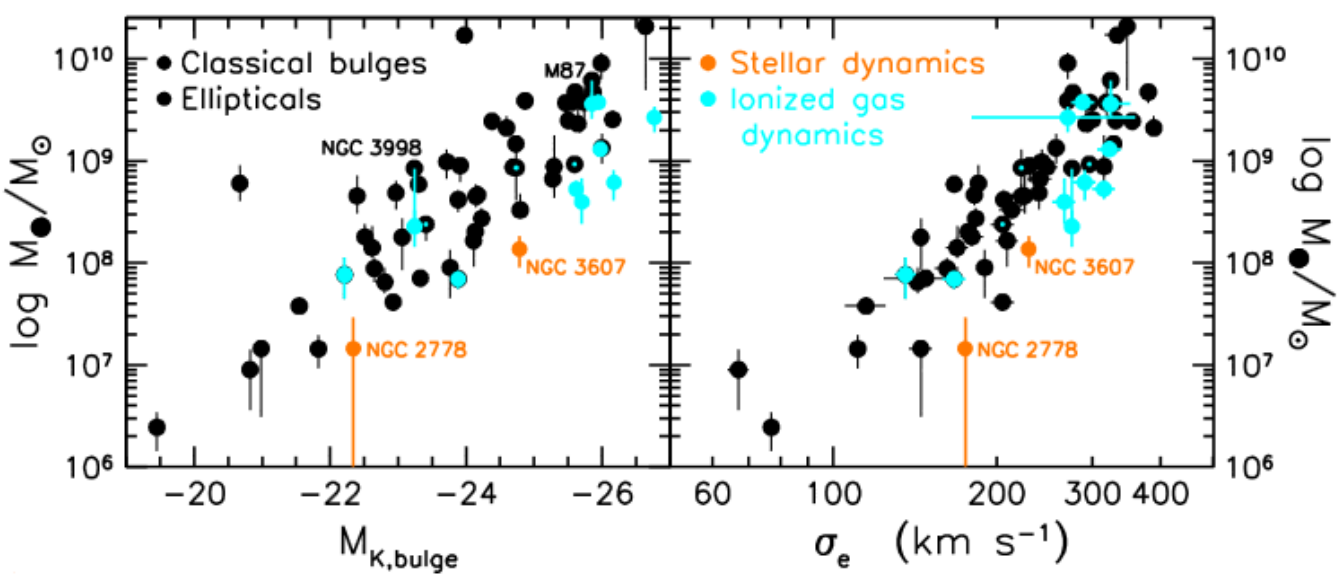

Figure 4: Correlations between BH mass (M•) and (left) the K-band absolute magnitude of the classical bulge or elliptical and (right) its effective velocity dispersion, taken from Kormendy & Ho (2013 [9]).

Currently, there are two known main modes of AGN feedback: radio (kinetic) mode and quasar (radiative) mode. The radio mode is usually, though not always, associated with powerful radio sources presenting poor radiative accretion efficiency. Hence, the main driver of feedback are extended jets injecting energy into the galaxy's ISM, heating up the gas and preventing star formation (McNamara & Nulsen, 2007 [12]). As the radiative accretion efficiency increases quasar mode takes over, with the radiation pressure driven by the AGN generating winds of ionized, atomic and molecular outflows from the circumnuclear gas (Fabian, 2012 [13]).

1.3.1 Outflows and feedback

The current understanding of AGN-driven outflows points to them having various effects on their host galaxies, as they can either promote star formation by pressurizing bubbles of cold gas and enhancing fragmentation, prevent star formation by disturbing and heating the ISM in zones where star formation hasn't yet triggered, and quenching ongoing star formation via the same principle. Recent works such as the one conducted by Bessiere & Ramos (2022 [14]) show that these effects can coexist on the same galaxy, pointing to a very complex and rich relation between outflow and galaxy characteristics.

Regarding the nature and morphology of outflows in general, much remains to be known at this point. Outflows are thought to be driven by either one of the energy emission modes of AGN, that is to say, radiative or mechanical (Harrison et al., 2018 [15]), so long as one of these modes is able to efficiently couple to the ISM surrounding the central black hole. The uncertainties involved in measuring their properties, and the assumptions required to estimate meaningful parameters from observation make the study of these phenomena extremely complex. Nonetheless, supported as it is by an ever-growing body of work, observational such as this project, and computational such as the simulations produced by Tanner & Weaver (2022, [16]), AGN outflows remain an exciting field of research.

As mentioned earlier, gas outflows are a result of AGN activity, and are composed of multiple phases; molecular, neutral atomic and ionized gas. Each of these gas phases make up different fractions of the total outflow mass rate, which seem to change with AGN luminosity. In the case of low to intermediate luminosity AGN ($L_{bol} \sim 10^{42-46}\ erg\ s^{-1}$), the molecular phase appears dominant(Fiore et al., 2017[17]), while at higher luminosity the ionized phase might become the leading fraction of outflowing gas (Fiore et al., 2017[17], Fluetsch et al., 2021,[18]). To fully characterize an outflow normally requires multi-wavelength studies (Fluetsch et al., 2021 [18]), as the tracers of the different phases tend to be spread out through the electromagnetic spectrum. However, depending on the redshift of the observed AGN, certain spectral bands can contain tracers of multiple phases, as is the case in this project, in which the K band is used for low redshift (z<0.14) type 2 quasars (reffered to as QSO2 from here on) in order to simultaneously characterize the ionized and molecular phases of the outflow.

1.3.2 Infrared spectrum of nearby Type 2 Quasars

It is this context in which QSO2 gain relevance, as the obscuration of the BLR and the AGN continuum due to the presence of the torus (Ramos and Ricci, 2017 [19]) makes them remarkable laboratories for studying outflows. The

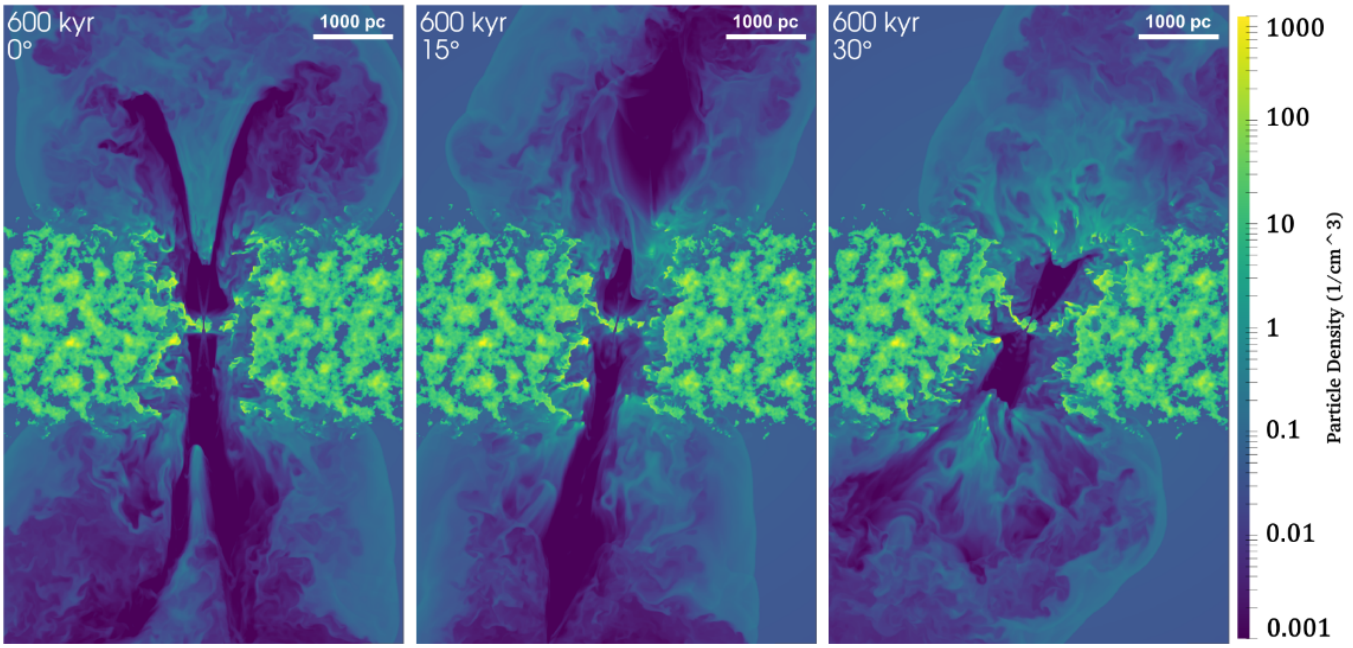

Figure 5: 3D relativistic hydrodynamical simulation of the effect of an AGN jet on a clumpy ISM for varying jet angles (0^{o}, 15^{o} and 30^{o} from left to right respectively), with AGN power $P_{AGN} = 10^{42}\ erg\ s^{-1}$. Taken from Tanner & Weaver (2022, [16]).

lack of broad lines produced in the BLR, which are obscured by the dusty torus, makes it possible to detect and characterize broad components associated with outflowing gas. Earlier we mentioned that the IR spectrum of these objects contains tracers of both the ionized and molecular phases of the outflow; in spite of this, as of the writing of this project, only 5 nearby ($z \leq 0.1$) QSO2s have been studied in the IR. These are F08572+3915:NW (Rupke & Veilleux, 2013 [20]), Mrk 477 (Villar Martín et al., 2015 [21]), J1430+1339 or the Teacup galaxy, (Ramos Almeida et al., 2017 [22]), J1509+0434 (Ramos Almeida et al., 2019 [23]) and J0945+1737 (Speranza et al., 2022 [24]). This project aims to double this sample size, both as a means to better our current understanding of this phenomenon as well as a way to build up a considerable sample of outflow parameters that can be compared, in the future, to those obtained in simulations.

In QSO2, the expected driver of AGN feedback is quasar mode, that is, radiation-driven winds from the accretion disk. However, one must not neglect radio mode, as low-powered jets ($P_{Jet} \sim 10^{44} erg\ s^{-1}$) can drive multi-phase outflows in active galaxies classified as radio-quiet (see Jarvis et al., 2019 [25]). In the same vein, quasar-mode driven outflows have been observed in radio loud sources (Speranza et al., 2021 [26]), meaning feedback is a complex and multi-faceted process which requires a case-by-case study basis to fully grasp.

The measurement of multi-phase outflow properties is made possible by the presence of molecular (H_2), low ionization (Paα, Brγ, Brδ) and high ionization/coronal([Si VI], [Si X]) lines in the K-band spectrum of nearby QSO2s. However, estimations of outflow mass and kinetic power require a measurement of the extension of said outflow, which, in the context of long slit spectroscopy, can be a tall hurdle to clear, as it requires very good observation conditions just to be able to spatially resolve and constrain the size of the outflow. An estimation of its density is also necessary, which can be done using the optical data from SDSS spectra, as the electron density can be measured using oxygen and sulphur emission lines, in tandem with a photoionization model.

Also worth noting is the fact that the observed molecular tracers, which in all cases correspond to weak quadrupolar transitions, only trace the warm molecular gas; this phase corresponds to a very small portion of the total molecular gas, and in fact, the observed hot-to-cold mass ratio for nearby LIRGs is estimated at $6{\times}10^{-5}$ (Emonts et al., 2017 [27]).

2 Data

2.1 Sample selection

For this project, all the studied objects are part of QSOFEED sample[1], which is in and of itself a fraction of the catalog published by Reyes et al. (2008) [3]. This catalog contains 887 type 2 quasars, selected through optical criteria

[1] http://research.iac.es/galeria/cra/qsofeed/

regarding their spectral features, namely, objects from SDSS which present high-ionization narrow emission lines. The Sloan Digital Sky Survey [28] provides public photometric and spectroscopic data covering $\sim 10000^2$ *deg* of sky.

From this sample, objects with $L_{[OIII]} > 10^{8.5} L_{\odot}$ (which is equivalent to $L_{Bol} > 10^{45.6}$ $erg\ s^{-1}$ using the bolometric correction of 3500 from Heckman et al., 2004 [29]) and z<0.14 were selected, leaving us with a final sample of 48 objects. The luminosity cut was to ensure the observed objects classified as QSO2, while the redshift cut made it so the molecular tracer $H_2$1-0 S(1) would always be detected in the K band. This sample, referred to as QSOFEED (see Ramos Almeida et al., 2022 [30] for details) is the final sample studied in this project, save for 4 objects which were only observed with either SINFONI (Spectrograph for INtegral Field Observations in the Near Infrared) or NIFS (Near-Infrared Integral Field Spectrometer) and another 4 objects which are yet to be observed. As such, the final size of the sample observed by EMIR consists of 40 QSO2. The spectral data for the entire sample was reduced and their spectra extracted and flux calibrated. Based on their spectral features, a subset of 6 objects was selected for further study, including telluric correction and line profile fitting. For this last sample, objects showing both molecular lines and ionized lines containing broad components were selected, since they would allow for simultaneous characterization of the ionized and molecular components of the outflow.

2.2 Data description

Table 1: Summary of the sample's observations. OB refers to the numerical order of the observation within the same block. The seeing values were measured using stars from the acquisition images and averaging out the FWHM of their brightness profiles.

Object	Block	OB	Seeing (")
J0052	2018A	1	1.0 ± 0.2
J0052	2019A	1	1.2 ± 0.2
J0052	2019A	2	0.6 ± 0.1
J0232	2018B	1	0.8 ± 0.1
J0731	2018B	1	0.6 ± 0.1
J0759	2018B	1	0.6 ± 0.1
J0802	2018B	1	0.6 ± 0.1
J0802bis	2018B	1	0.8 ± 0.1
J0805	2018B	1	0.6 ± 0.1
J0805	2019A	1	0.9 ± 0.2
J0818	2018B	1	0.8 ± 0.1
J0841	2018B	1	0.7 ± 0.1
J0858	2018B	1	0.7 ± 0.1
J0915	2018B	1	0.6 ± 0.1
J0939	2018B	1	0.9 ± 0.1
J0945	2018B	1	1.4 ± 0.2
J1010	2018B	1	0.7 ± 0.1
J1015	2018B	1	0.7 ± 0.2
J1016	2018B	1	0.7 ± 0.1
J1034	2019A	1	1.0 ± 0.2
J1036	2018B	1	0.8 ± 0.1
J1157	2020A	1	1.0 ± 0.1
J1218	2019A	1	0.9 ± 0.1
J1223	2020A	1	0.9 ± 0.2
J1241	2020A	1	0.8 ± 0.1
J1316	2018A	1	0.8 ± 0.1
J1347	2018A	1	0.7 ± 0.1
J1356	2018A	1	0.6 ± 0.1
J1356	2019A	1	1.0 ± 0.2
J1356bis	2020A	1	0.8 ± 0.2

Object	Block	OB	Seeing (")
J1405	2019A	1	0.8 ± 0.2
J1436	2018A	1	0.8 ± 0.1
J1436	2019A	1	0.7 ± 0.1
J1437	2019A	1	0.8 ± 0.1
J1440	2019A	1	0.8 ± 0.1
J1455	2018A	1	1.2 ± 0.2
J1455	2019A	1	0.8 ± 0.1
J1509	2018A	1	0.7 ± 0.1
J1517	2019A	1	1.0 ± 0.1
J1533	2018A	1	0.8 ± 0.1
J1533	2019A	1	0.6 ± 0.1
J1548	2018A	1	0.6 ± 0.1
J1558	2019A	1	0.8 ± 0.1
J1624	2018A	1	0.6 ± 0.1
J1624	2019A	1	0.8 ± 0.1
J1624	2019A	2	0.8 ± 0.2
J1624	2019A	3	1.0 ± 0.1
J1653	2018A	1	0.8 ± 0.1
J1653	2019A	1	0.7 ± 0.1
J1653	2019A	2	0.6 ± 0.1
J1653	2019A	3	1.0 ± 0.1
J1713	2018A	1	0.8 ± 0.1
J1713	2019A	1	1.0 ± 0.2
J1713	2019A	2	0.9 ± 0.1
J1713	2019A	3	1.1 ± 0.2
J2154	2018A	1	0.8 ± 0.1
J2154	2019A	1	1.2 ± 0.2
J2154	2019A	2	1.0 ± 0.1
J2154	2019A	3	1.0 ± 0.2

All observations were made using the NIR multi-slit spectrograph EMIR (Garzón et al., 2006 [31], 2014 [32]), installed in the Nasmyth-A focus of the 10.4m GTC, situated at the Roque de los Muchachos Observatory. EMIR's detector is a 2048x2048 Teledyne HAWAII-2 HgCdTe optimized for NIR observations, with a 0.2" pixel size. The data used in this work spans observations from May of 2018 to June of 2020, and is divided in four semesters. The combined observation clocks in at approximately 96 hours, with an average on-source time of 1900 s per object. Each observation contains

object, flat and spectral arc images for reduction and calibration, both for the science targets and comparison stars. The wavelength range covered by the observations varies from one to another, as the slit's position can be modified to suit each object depending on its redshift. All spectra were taken using the K grism, with the total range spanning from 1.97μm to 2.43μm, and a nominal spectral resolution of 4500 ($\sim$ 70 km/s at 2.2 μm).

3 Methodology

3.1 Spectra reduction

As many other forms of data collection in the field of astronomy, infrared spectroscopy requires a considerable amount of treatment before usable data can be extracted from the acquired spectra. In this particular case, the raw spectra will be corrected for pixel-to-pixel variations using flat field exposures, given that the detector's reading method already subtracts the bias and EMIR works at a temperature low enough to make dark currents a non-factor. As such, the only intrinsic sources of noise for the spectra will be pixel-to-pixel sensitivity differences and read noise.

Besides flat field correction, ground-based near-infrared observations make use of the "nodding" technique to minimize the effects of sky emission, since a black body at room temperature (air temperature in this case) emits a considerable amount of radiation at these wavelengths. The emission peak for the sky lies at around 10 μm, and the K band used for all of our observations goes from 2.0 μm to 2.4 μm. While mid-infrared observations tend to use both "chopping" and "nodding", the time scale of the flux variations in the NIR sky make chopping unnecessary.

3.1.1 Flat-field image generation

For flat field correction, 10 images are taken in groups of 5, with 2 different exposures, aimed at a blank, uniformly illuminated screen. For the so-called blue flats, the exposures are of 1.5 seconds, while the red flats use 6 seconds exposures. This difference stems from the filter transmittance being wavelength dependant, the flat lamp having its emission peak in the visible wavelengths and the red region requiring a longer exposure to accurately represent the pixel-to-pixel sensitivity of the detector. Consequently, these images will be combined and normalized separately in the blue and red groups, and then joined; blue flats being used from the 0th to the 1400th pixel (on the horizontal axis), and red from the 1401st onward.

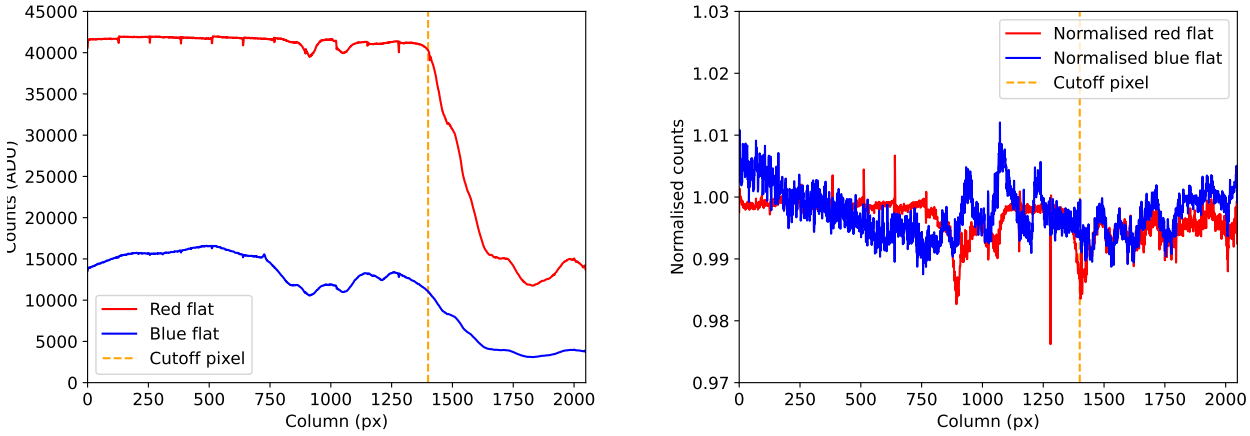

(a) Comparison between red and blue flats before correction and normalisation.

(b) Comparison between normalised and corrected red and blue flats

Figure 6: Spatial average of the combined red and blue flat images.

Before joining these two flats, however, a script is used to further reduce the effects of the spectral response function of the filter and the possible differences in illumination. This is done by estimating the average in the spatial direction, which yields the spectral response function, dividing each row by this response function, and then averaging in the spectral direction to estimate the illumination function, then dividing each column by it. This is all done in order to achieve an image that most closely captures the detectors' idiosyncrasies. Bad pixels are also taken into account and corrected; a bad pixel mask is created through IRAF's *ccdmask* task, using the quotient of the brightest and dimmest flat field images.

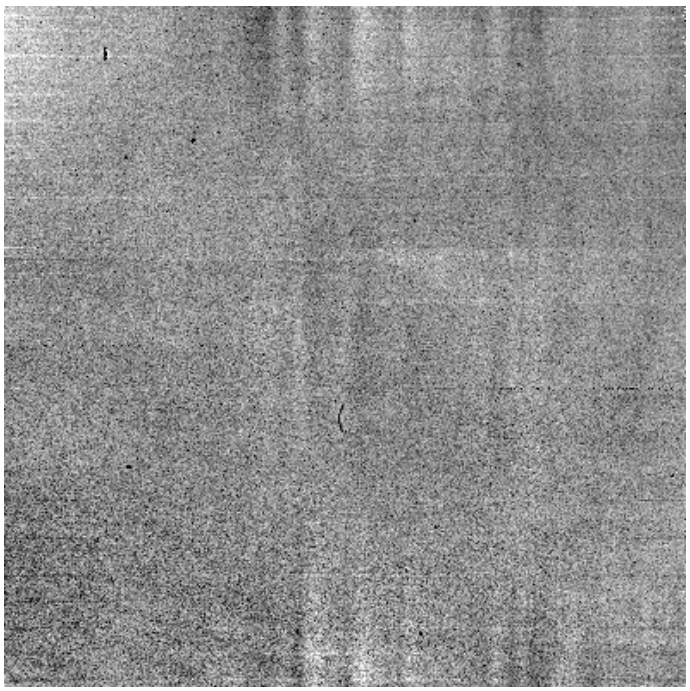

Figure 7: Combined flat field image. Darker areas represent less sensitive pixels, and the opposite for whiter ones.

3.1.2 Sky subtraction

The key to minimizing sky noise in NIR observations lies in the nodding technique. It consists of small telescope offset which allows the placement of the target at two different positions along the slit.

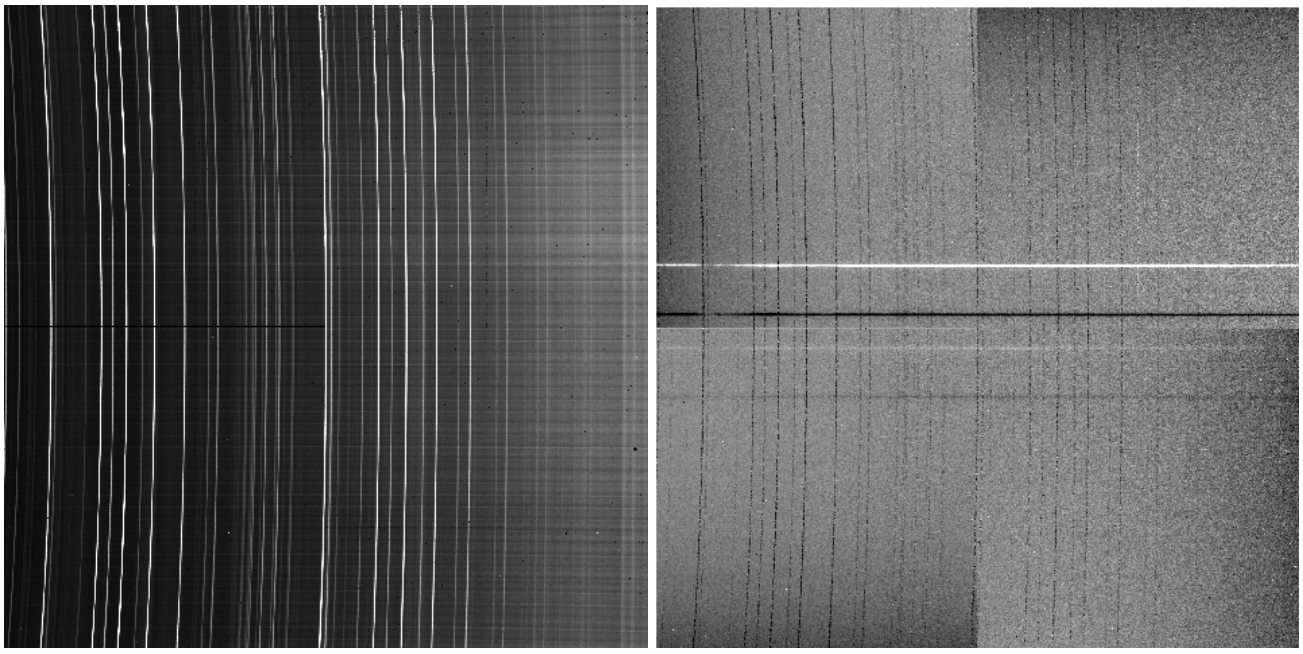

(a) Position A nod acquisition of J1440's spectrum.

(b) (A-B) spectrum from J1440.

Figure 8: Difference between single nod acquisition spectrum and nod subtraction spectrum for J1440. Sky emission is visibly reduced.

A complete NIR spectroscopic observation will consist of a number of spectra on nod A, and the same number on nod B. At minimum, there will be two A nods and two B nods, since the observation pattern used is ABBA. All A nods will be paired with B nods and we'll obtain from them both differences, that is;

$$(A-B)_n = Nod_{A,n} - Nod_{B,n} \quad (1)$$
$$(B-A)_n = Nod_{B,n} - Nod_{A,n} \quad (2)$$

Any one of these spectra should have the sky emission considerably reduced, although not completely. The variability of the infrared sky combined with the very long object exposures make it difficult to eliminate the sky background to a certain extent just by the use of nodding. However, the high contrast between emission lines and background means nodding is enough when dealing with the NIR sky in spectroscopy.

The residual background visible in these spectra will be minimized again by combining all of these subtractions into one final image via the use of the IRAF package's *lirisdr* task *lspnodcomb*. Since the subtraction means we will be moving the spectra along the slit, this is also the step where the images are wavelength calibrated. In the case of our data, wavelength calibration must be performed across the whole dimension of the detector (or rather, the slit). Different parts of the slit will differ slightly in how they disperse incoming light, meaning just one wavelength calibration isn't valid for its entirety, as is visible in figure 8, where the sky lines trace curves instead of straight lines. The same thing happens to the object's lines and as such, moving the spectrum along the slit without calibrating would result in a faulty final spectrum.

For the sake of this wavelength calibration, most observations come equipped with spectra of a set of element arc lamps. In the case of EMIR, they include helium, xenon and neon. These spectra are complemented by identfication charts of most every line included in the wavelength range of interest for every band. For a preliminary calibration, we make use of the IRAF task *identify*, which lets us mark all spectral features we deem necessary and assign them a wavelength. For this first calibration, the user chooses which rows will be used. This task is then complimented by *reidentify*, which propagates the line identification to the slit extent. This task works in groups of 20 rows each, combining them and searching for the spectral features marked earlier in a radius around the previous centroid. Each of these groups will be assigned a calibration of its own, and this process will be repeated until the entire detector has been characterised. With the calibration ready, the lines are "straightened" and the sky can be properly reduced by *lspnodcomb*.

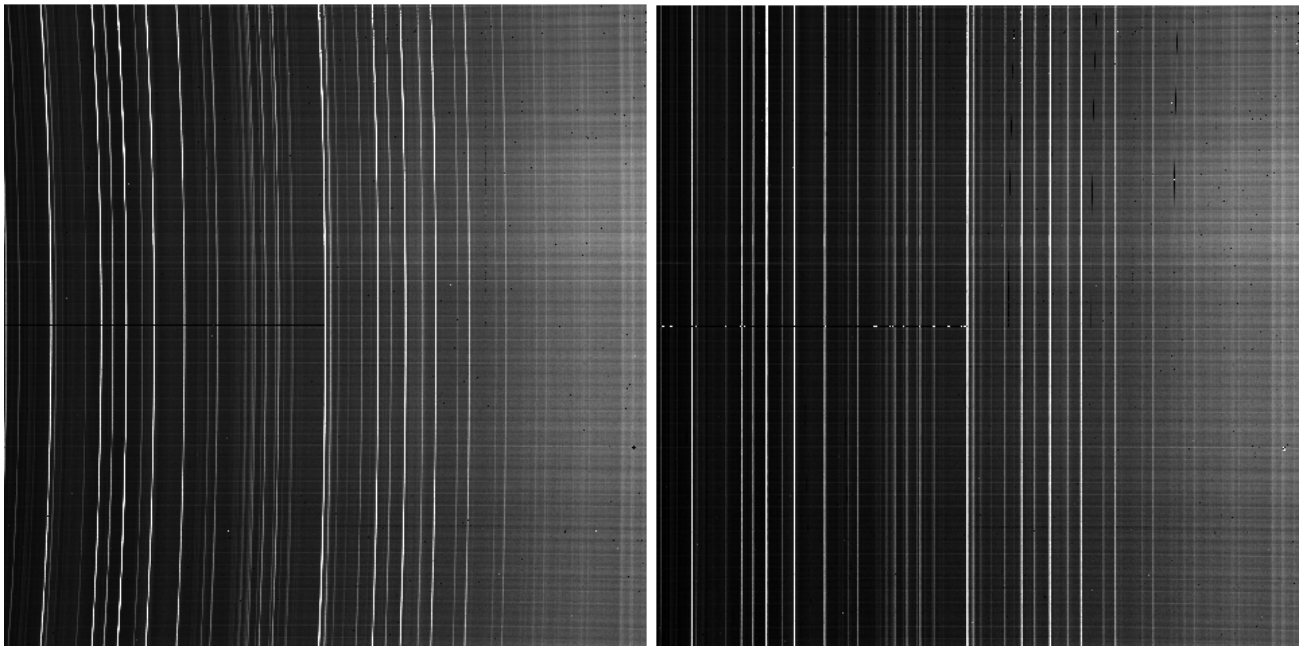

(a) 2D spectrum of J1440 prior to wavelength calibration. (b) 2D spectrum of J1440 after wavelength calibration.

Figure 9: Comparison between wavelength uncalibrated and calibrated spectra of J1440.

Once the spectra have been combined, we can advance to the extraction of 1-dimensional spectra. There is a stark contrast between any one of the nod subtractions and the final combined image, so this step is essential in obtaining a good signal-to-noise ratio. As the A and B nod place the source in different parts of the image, they need to be offset a certain amount at the time of combining. This can be done either by using the images' data header, as we do in our case, or through cross-correlation.

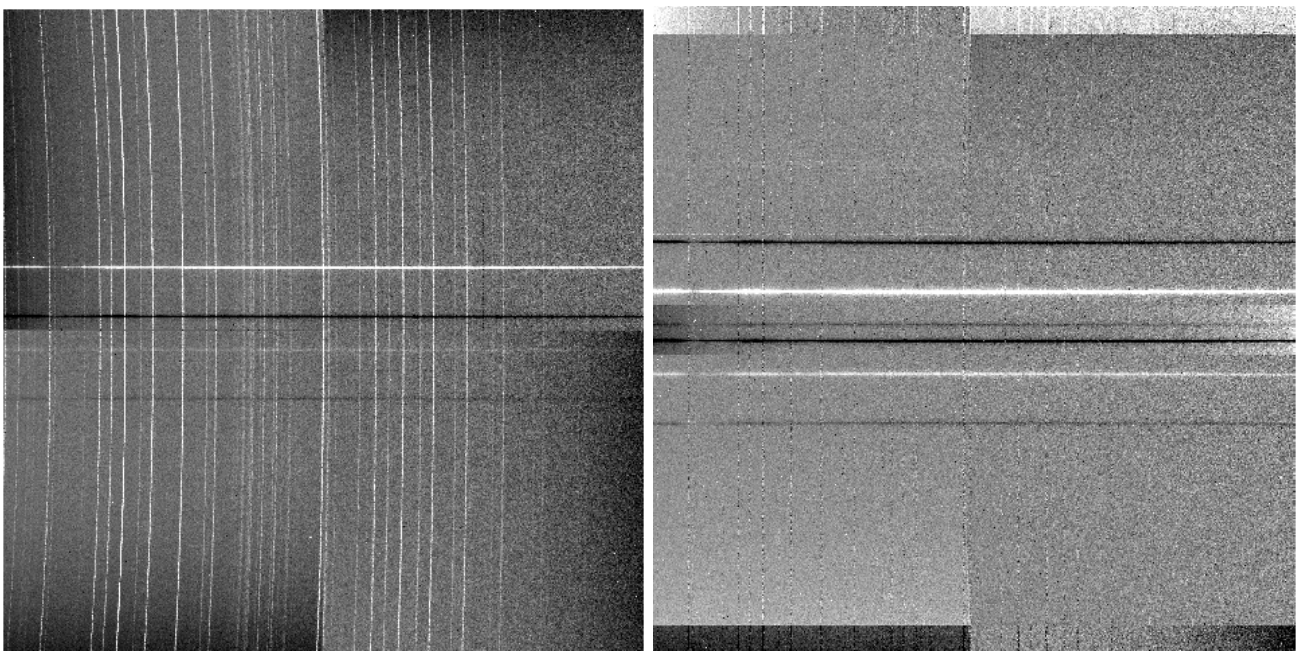

(a) (B-A) image of J1440.

(b) Combined image of J1440.

Figure 10: Comparison between single nod subtraction and final combined image of J1440. For the combined image, the object traces are much brighter and the sky lines and flat field effects are almost completely eliminated.

3.2 Spectra extraction

For the extraction of 1-dimensional spectra from these 2-dimensional acquisitions, we will make use of IRAF's *apextract* package, which includes the *apall* task. This task allows us to pick multiple apertures (although in this case we will use a single one), their size, the background to be subtracted, and the function used to trace the object's spectra through the detector.

For the aperture size, two different sizes were picked for each observation: a seeing-sized diameter, to minimize background noise, and a fixed diameter of 3 arcseconds. This size is equal to that of the one used in the observations of the Sloan Digital Sky Survey, and is used to ensure a fair comparison with their data is possible. The seeing is measured using IRAF's task *imexamine*, which allows for measuring the brightness profiles of different field stars. Observations include acquisition images without the dispersing elements, referred to as "open" grism images which are actually taken with the J filter and contain simple imaging of field stars.

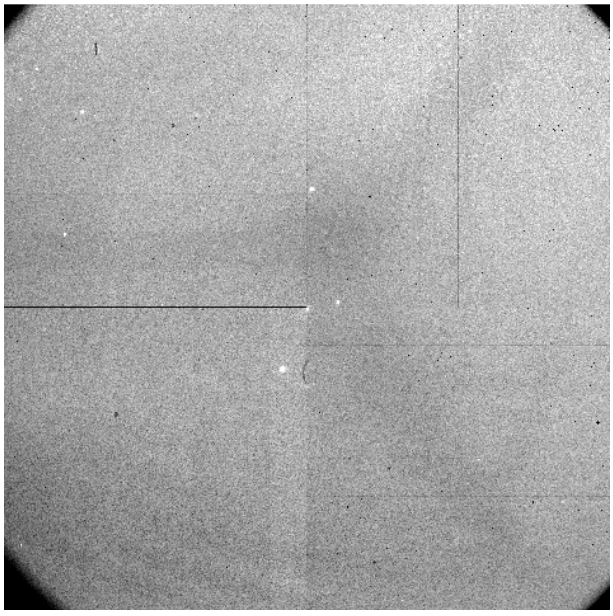

Figure 11: "Open" grism image for the J1440 observation block.

The object is traced across the 2D spectrum using a Legendre polynomial, usually of order 4 or lower. The background sections used for subtraction are the lower part of the spectrum and the section spanning between the positive trace and the upper negative trace. Normally both sections between the positive and negative traces would be used, but due to visual artifacts appearing in the space between the positive and lower negative trace, the lower part of the image is used in its stead. The background is modeled using an order 1 Chebyshev polynomial.

3.3 Flux calibration

The flux in all the spectra obtained up to this point is measured in ADUs/counts, meaning we need to perform a flux calibration in order to obtain meaningful information regarding the source object's brightness. To perform this transformation, we use field stars of known magnitude in the filter of interest (in this case, K) and known spectral type. From the spectral type, we can model the theoretical black body radiation emission of such a star, and combining it with the integrated magnitude in the K filter and the K filter's transmittance, we can obtain the SI flux equivalent to ADUs, that is, the flux calibration.

The stars used need to satisfy certain conditions, such as a low amount of spectral features in the wavelength interval of interest, relative proximity to the science target, a good signal-to-noise ratio, and some others such as their binary character or their proper motions. Few or easy to model spectral features are necessary to correctly model their continuum, while their proximity to the science target implies small differences in the air masses of their respective observations while minimizing the effect of large-scale differences in the atmosphere. A good signal-to-noise ratio is self-explanatory, and it's better to avoid stars with large proper motions due to further corrections being necessary otherwise.

The magnitudes and spectral types are obtained from the SIMBAD Astronomical Database[2]; every observation includes a Quality Control file, which contains the coordinates of the star observed for calibration and telluric correction purposes. After obtaining the relevant information, we make use of IRAF's *continuum* task to model the stars' continuum from its K-band spectra. Since the star is subject to telluric absorption, only the wavelength intervals in which radiation remain unaffected are used for the model. After that, the *standard* task uses the model to transform adimensional data units to SI units, and *sensfunc* yields the sensitivity function.

The outputs from *standard* and *sensfunc* are then used in the *calibrate* task to calibrate any given spectra from either the object or the field star, which includes the transformation from ADUs to $erg\ s^{-1}cm^{-2}\text{Å}^{-1}$.

3.4 Telluric correction

As our observations are ground-based, we will need to deal with contamination from atmospheric effects, which result in absorption lines and bands. This is known as telluric absorption, and in our window of interest, it is mostly caused by water vapour, carbon dioxide and methane. To correct for this effects, the process goes as follows: the telluric star's spectra is divided by the continuum modelled in the flux calibration (section 3.3) process, resulting in a spectrum which recreates the atmospheric transmittance for that given set of observations. The regions of unaffected (fully transmitted through the atmosphere) stellar continuum correspond to a value of 1 in this spectrum, with absorption features appearing between 1 and 0. Usually, it's preferable to perform this division after calibrating both spectra, since eliminating the curvature from the filter's transmittance should result in a clear continuum shape, meaning it's easier to check the correction.

Once this spectrum has been obtained, the IRAF task *telluric* is used. This task allows us to adjust the differences between the science object and telluric star's observations, such as the airmass and wavelength offsets. Both the airmass scale and the wavelength shift between spectra can be modified until a satisfactory correction has been achieved.

On certain occasions, due to higher noise levels in the absorption bands, it is necessary to follow an alternate procedure based on theoretical models for telluric absorption. These theoretical models are created using ESO's tool SKYCALC Sky Model Calculator (S. Moehler et al., 2014 [33]). It allows for custom modeling of transmission and radiance models. In our case, only the transmission components were modelled, using the wavelength range of the K-band, linear binning equivalent to the spectral dispersion of the EMIR Ksp grism, the closest value of precipitable water vapor to the one observed in ORM[3] and the source's observation airmass.

[2] http://simbad.u-strasbg.fr/simbad/
[3] https://www.iac.es/es/observatorios-de-canarias/calidad-del-cielo/parametros-de-calidad-del-cielo/vapor-de-agua-precipitable

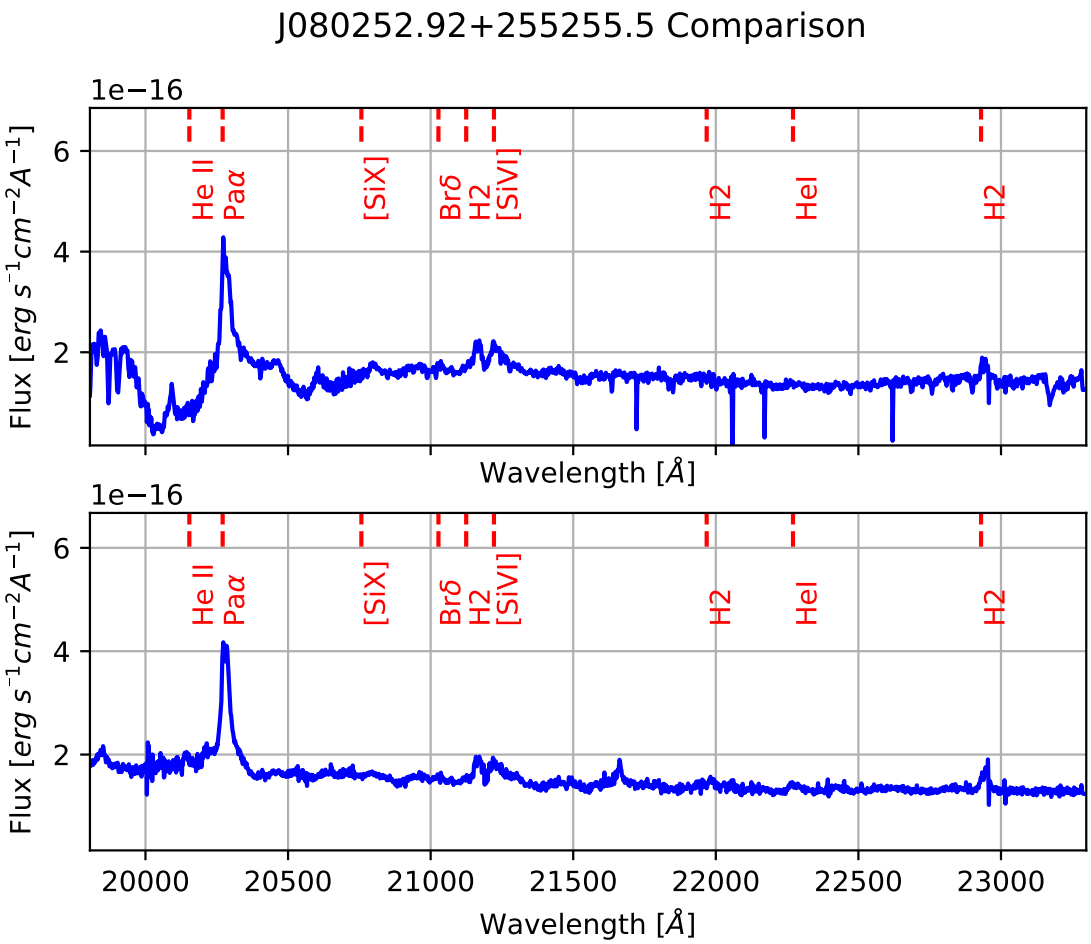

Figure 12: Comparison between the calibrated and corrected spectra of J0802+25. On the top, the calibrated image shows telluric absorption bands, while the corrected image on the bottom is rid of these features and presents a flat continuum.

This model is used to correct the spectrum of the comparison star, and this corrected spectrum is then used to obtain the flux calibration. Once the science target spectrum has been flux calibrated, the model is then used to perform the telluric calibration. While this process is somewhat slower due to it requiring the modelling of the observation conditions for both the comparison star and target source as well as performing two telluric corrections, it avoids the high noise present in the blue end of some observations as well as the need to eliminate stellar features from the telluric spectrum. Another option would have been to use the *Molecfit* (Smette et al., 2015 [34]) developed by ESO, which corrects the telluric absorption by directly fitting the Skycalc models.

3.5 Multi-component analysis

Once the entire sample had been reduced, extracted and calibrated, we used visual means to select a smaller subsample, comprised of a few objects which showed clear signs of outflows. This subsample, consisting of 6 objects, was then corrected for telluric absorption, meaning their spectra were ready for analysis. The Python-built *modeling* module from *Astropy* (Astropy Collaboration et al., 2013 [35], 2018 [36]) was used to fit these lines, while the *Specutils* module was used for fitting the continuum and general handling of spectra and their data.

All sources studied in this project have also been observed by SDSS, including their optical spectra. Due to the complexity and relatively low signal that some of the sample objects present in the K-band, the lines were first fitted to the SDSS spectrum of each object, which have a consistently and considerably higher signal-to-noise ratio, and the obtained fit parameters (namely the line FWHM and relative velocity) were later used for fitting the EMIR spectrum. This, however, only holds true for the ionized lines, since there are no molecular gas tracers in the SDSS spectra.

To perform the fit we first select two intervals, redwards and bluewards of whatever line(s) we're fitting at any given instance, to fit the continuum, as well as another interval containing the line(s). We can then define the initial parameters for the fit. We first fit the SDSS spectrum, which has considerably higher signal-to-noise ratio. The initial parameters in this case are just educated guesses, based on the shape of the line. At first, we always fit 3 components at the least, and from the resulting fit we can decide on adding another component if necessary. In whichever case,

the parameters are tweaked until flat residuals are achieved. The [OIII] lines at 5007 Å and 4959 Å are fit first, and H β is then fit using the resulting parameters. Usually the kinematics and widths of the H β fit will be tied to the values of the [OIII] fit, unless this results in a bad fit. For the [OIII] lines, the amplitudes are tied, since the relation between line amplitudes for these particular pair is well defined (Dimitrijevic et al., 2007 [37]), and the widths and relative velocities are also tied to their respective components, as both these lines trace the same gas.

The EMIR fit begins with the line with the highest S/N, which is either Pa α, or in case this line is not included in the spectrum, [SiVI]. Similar to the SDSS spectrum, the lines close to either Pa α or [SiVI] are fit using tied parameters, since these ionized lines trace the same gas components and as such, should have very similar kinematics. EMIR spectra can also include molecular H_2 lines, as is the case for all the objects studied in this project. Since these lines trace a different gas component, the fit is made with free parameters. Due to the molecular lines usually tracing a single component, fitting them is simpler than the ionized ones.

One might wonder why is it even necessary to analyse the profiles of lines for which we supposedly already know the kinematics; there are two reasons for this. The first is to check that the profiles observed in the optical and IR wavelengths are the same. This is not trivial and as a matter of fact, there is an object in our sample, J0802+25 (see section 4.1), for which there is a component observed in the IR spectrum which isn't present in the optical. The ionized gas phase is made up of different components at various temperatures; certain parts of the gas might be untraceable in certain wavelengths. The second reason is to be able to properly analyse molecular lines that are blended in with ionized lines, as is the case for H_2 1-0 S(3) and [SiVI].

The uncertainties of the parameters are measured using a Monte Carlo simulation. This simulation generates mock spectra by adding random values to the flux of each spectral element, which are taken from a distribution with an amplitude given by the pixel noise. The uncertainty of each parameter is estimated as the standard deviation of the value distribution of said parameter, computed using 100 mock spectra.

Tied parameters take their errors from the same fit they get their value from; their uncertainties will be marked with an asterisk from hereon. For example, if we fit both [OIII] lines with their amplitudes tied according to the aforementioned relation, the uncertainties for the amplitude of each component will be the same for both lines (see table 3 for an example). Fixed parameters have no uncertainties, given that they're taken as constant.

To estimate the relative velocities, we use the center of the narrow component of the brightest ionized line as the center of our reference system, since the narrow component comes from the NLR. Using the formula for the classical Doppler effect (outflow velocities are never close to c)

$$v = \left(\frac{\lambda_e}{\lambda_o} - 1\right) \cdot c \tag{3}$$

A negative velocity means the observed component moves in our direction, and a positive velocity will mean the opposite. The involved wavelengths are the emitted wavelength λ_e and the observed wavelength λ_o. For the reference lines ([OIII] 5007 Å, Pa α and [Si VI]), λ_e will be the central wavelength of the narrow component; from this wavelength, we estimate the redshift and use it to calculate the velocity shifts for the rest of lines and components. The uncertainties are calculated by using propagation of uncertainties on equation 3.

4 Results

For an overview of the characteristics of the entire sample, the spectra of all observations has been included in the Appendix. In this sample, we observe a large variety of QSO2 spectra; some present only one or two narrow ionized lines while others host a plethora of ionized and molecular lines with blended profiles and components. We also see variety in the continua of the sample; while some are entirely flat in the entire wavelength range of observations, others present a continuum level that decreases with increasing wavelength. The majority of the objects present a flat or close to flat continuum with very narrow ionized lines, as is expected for this class of AGN.

The selected subsample consists of 6 objects, 5 of which have not had their outflows simultaneously characterized in the IR yet. The selection process of these objects was based on visual methods, picking out those which showed clear signs of outflows. For each one of these objects, the EMIR observations were complemented by SDSS spectroscopic data on the optical range.

Table 2: Spectral features fitted in the sample objects. The number of components for both EMIR and SDSS is taken from the brightest line, and the number of ionized and molecular lines is taken from EMIR lines, since the SDSS spectra contained the same lines for all objects.

Object	No. of ionized lines	No. of molecular lines	No. of components (SDSS)	No. of components (EMIR)
J0802+25	4	2	4	4
J0945+17	5	1	3	3
J1034+60	3	3	4	4
J1440+53	4	4	3	3
J1455+32	5	1	3	3
J1713+57	5	3	3	3

4 of the 6 objects presented a narrow, intermediate and broad component in their ionized lines, while the remaining two had another component on top of those three. Between 6 and 8 total lines are fitted for each object. We can divide the observed lines according to which gas phase they are generated by; the fitted ionized gas lines are the low ionization Pa α, Br γ, Br δ, HeII(1.8637μm), HeI(1.8691μm) and HeI(2.0587μm) lines, while the high-ionization/coronal (ionization potential E_i=166.7 eV) [SiVI] line is also detected. The other coronal line, [SiX], while observed in some of the subsample spectra, couldn't be clearly fitted due to either low signal or high noise levels. The fitted molecular gas lines are all generated by weak quadrupolar transitions of the H_2 line, namely, H_2 1-0 S(0) through S(3).

We will now proceed to study the resulting fits to the lines, and the gas kinematics estimated from the parameters obtained therein.

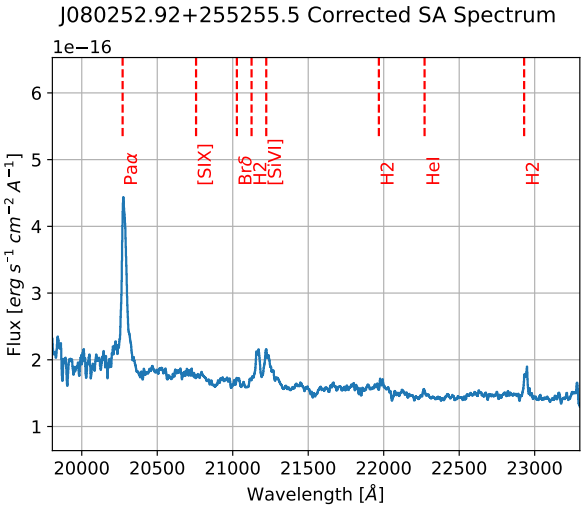

(a) J0802+25

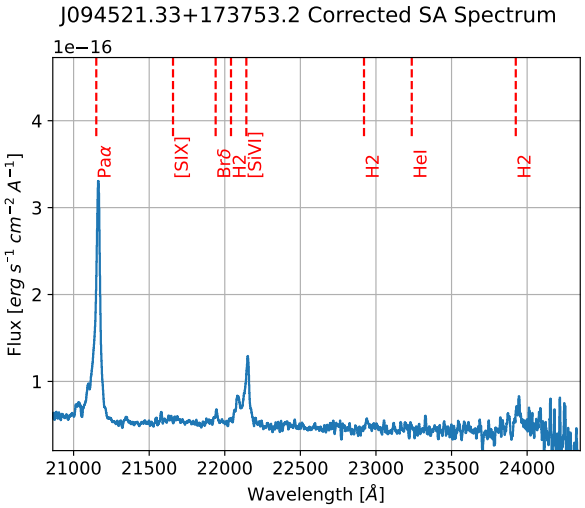

(b) J0945+17

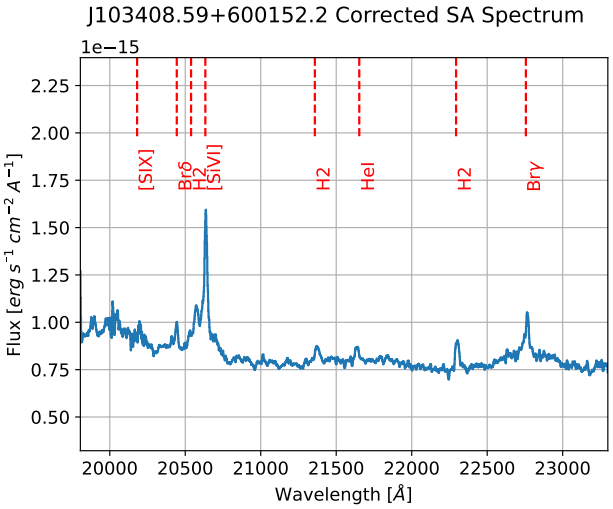

(c) J1034+60

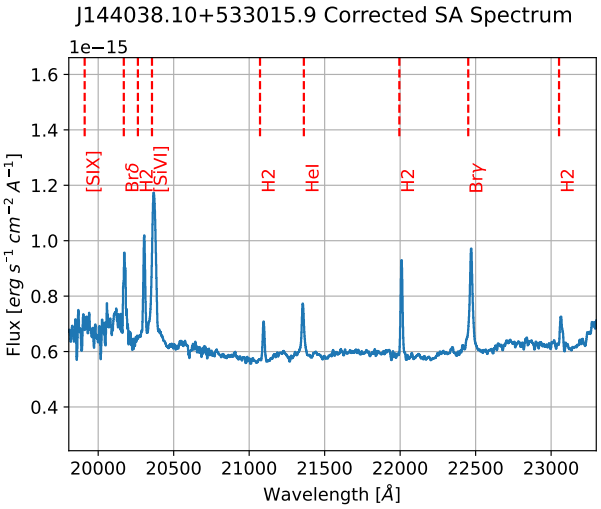

(d) J1440+53

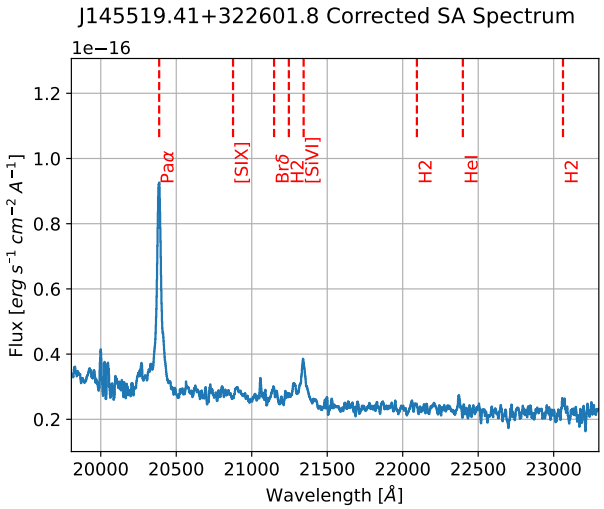

(e) J1455+32

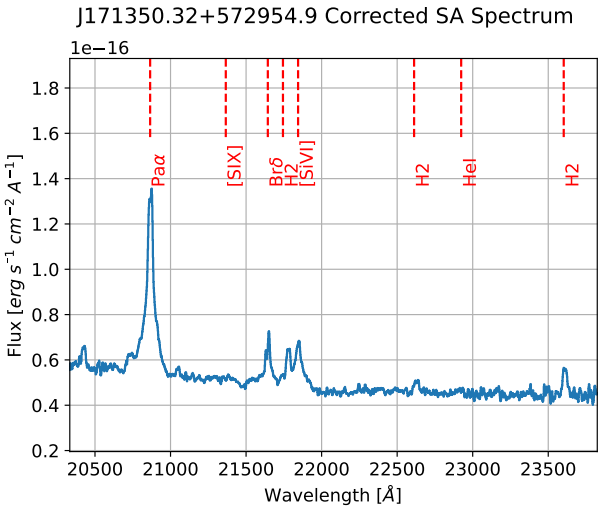

(f) J1713+57

Figure 13: Spectra for the subset of selected objects. All spectra have been flux calibrated, corrected for telluric absorption and smoothed using a 3rd degree Savitzky-Golay filter with a step size of 11 pixels.

For each object, there will be a short introduction including some relevant parameters, such as the morphological classification of the host galaxy, taken from Pierce et al., 2022 [38], and the bolometric AGN luminosity, estimated using the 3500 factor for correction from Heckman et al., 2004 [29] and using the [OIII] luminosity computed using the non-parametric fit from the catalog by Reyes et al., 2008 [3].

4.1 J0802+25

J0802+25 (SDSS identifier J080252.92+255255.6) is a QSO2 with a redshift of z=0.08093±0.00002, estimated from spectroscopic measurements from SDSS's 8th data release (Alam et al., 2015 [39]), and a luminosity of $L_{bol} = 10^{45.99}\ erg\,s^{-1}$. It is classified as a merger, currently in a stage of post-coalescence (Pierce et al., 2022 [38]). The seeing during its observation was 0.8". The star used for calibration was HD 76619, an A0 spectral type star.

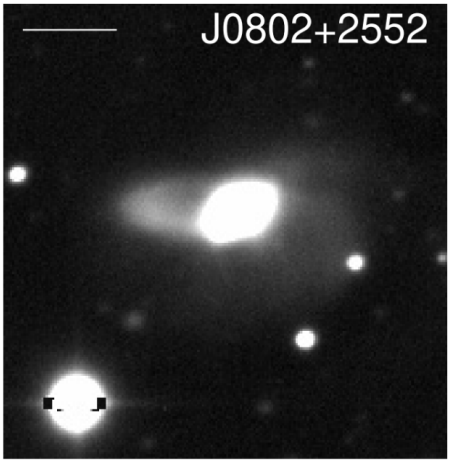

Figure 14: INT/WFC image of J0802+25 from J. Pierce et al., 2022[38]. Signs of disturbance are visible, such as the asymmetrical shape of the disk/halo.

J0802+25 was selected due to its lines being clearly asymmetrical, presenting a blueshifted broad component (see figure 13a). Upon further analysis, it was found that another blueshifted but considerably narrower component was necessary to fully characterize the lines. Multiple ionization lines were observed, and two molecular tracers, H_2 1-0 S(1) and H_2 1-0 S(3), were also present in the spectrum.

4.1.1 SDSS spectrum

The SDSS spectrum of J0802+25 was initially fitted with three components for each line, but it became apparent that another component was needed to correctly fit the line's profile. This component is referred to with the (e) identifier,

standing for "extra". The resulting fits are presented in figure 15, for both oxygen lines and Hβ, the latter of which very clearly reproduced the profiles fitted on the oxygen lines.

Table 3: Emission line properties measured from the J0802+25 SDSS spectrum. Uncertainties from tied parameters are marked with *.

Line	Center (Å)	Flux $\times 10^{-15}$(erg cm^{-2} s^{-1})	FWHM (km/s)	Velocity (km/s)
[*OIII*]5007Å(n)	5413.09± 0.01	24.8±0.3	210±1	0±1
[*OIII*]5007Å(i)	5415.46±0.02	78.1±0.5	487±2	131±1
[*OIII*]5007Å(b)	5410.42±0.06	72.3±0.7	1329±6	-148±4
[*OIII*]5007Å(e)	5397.84±0.10	2.88±0.16	348±14	-846±6
[*OIII*]4959Å(n)	5361.27±0.01*	8.26±0.08	211±1*	4±1
[*OIII*]4959Å(i)	5363.54±0.02*	26.0±0.2	492±2*	131±1*
[*OIII*]4959Å(b)	5358.55±0.06*	24.1±0.2	1343±6*	-148±4*
[*OIII*]4959Å(e)	5346.09±0.10*	0.96±0.05	351±14*	-846±6*
H β(n)	5255.66±0.08	1.40±0.06	192	24±5
H β(i)	5257.63	7.65±0.16	483	136
H β(b)	5252.63	4.58±0.25	1331	-150
H β(e)	5240.23	0.28±0.08	341	-858

The widths and relative velocities of [OIII]4959Å were tied to those of [OIII]5007Å, while for H β the widths of all components were fixed to the values from the [OIII] fit, and the centers of every component except the narrow one were also fixed relative to the center of [OIII]5007Å.

Regarding the estimated parameters, which are presented in table 3, we measure a broad component of the ionized gas as outflowing at a velocity of $\sim$ 150 km/s with very low uncertainties, as well as an outflow of the intermediate component of the gas. The "extra" component, which presents an FWHM of $\sim$ 350 km/s, between the narrow and intermediate components, is outflowing at a much greater speed of $\sim$ 850 km/s. Due to the very high signal-to-noise ratio of the SDSS spectrum, these measurements present very small uncertainties.

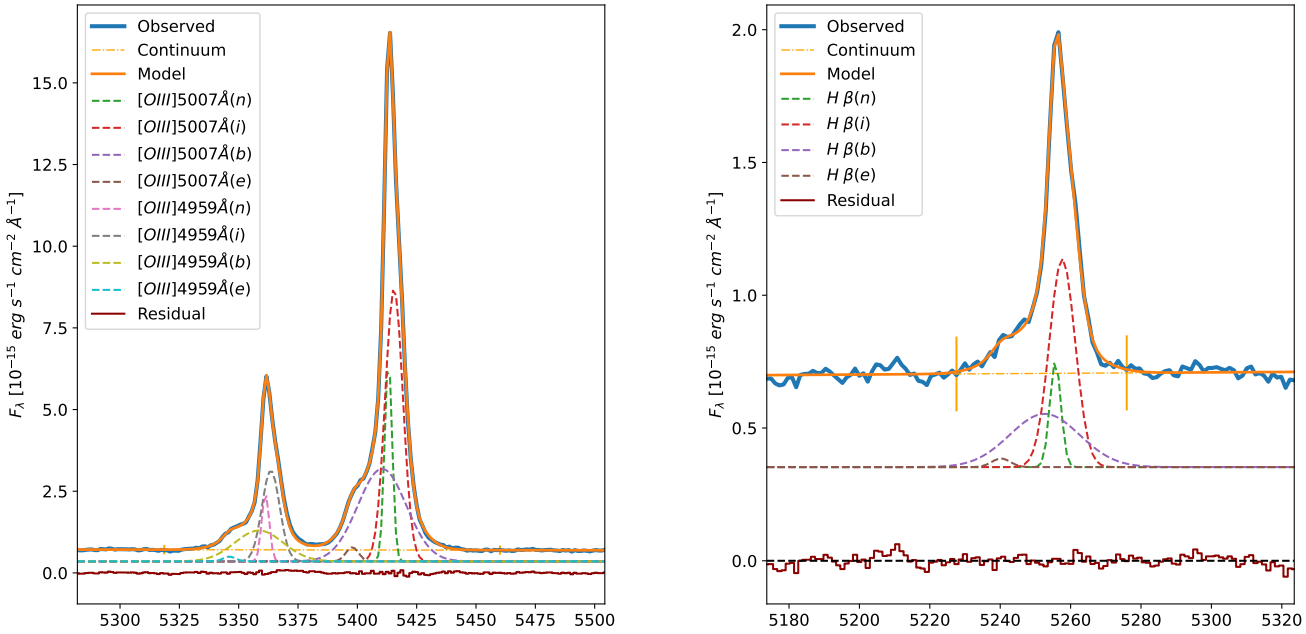

(a) Line profiles of OIII(4959Å) and OIII5007Å).

(b) Line profile of Hβ

Figure 15: Gaussian fits for the $H\beta$ and $[OIII]$ lines for the J0802+25 SDSS spectrum.

4.1.2 EMIR spectrum

The observed lines in the EMIR spectrum were the ionized gas tracers Pa α, HeI (1869.1nm), HeII (1863.7nm), [SiVI] and the molecular gas tracers H_2 1-0 S(3) and H_2 1-0 S(1) (see figure 13c). Regarding the fits of the ionized lines (see figure 16), we find a new component in the profile of Pa α. This component appears to be shifted quite far to the red of the central wavelength, and is responsible for the observed red wing of the line profile. This component is referred to as (d) in our analysis.

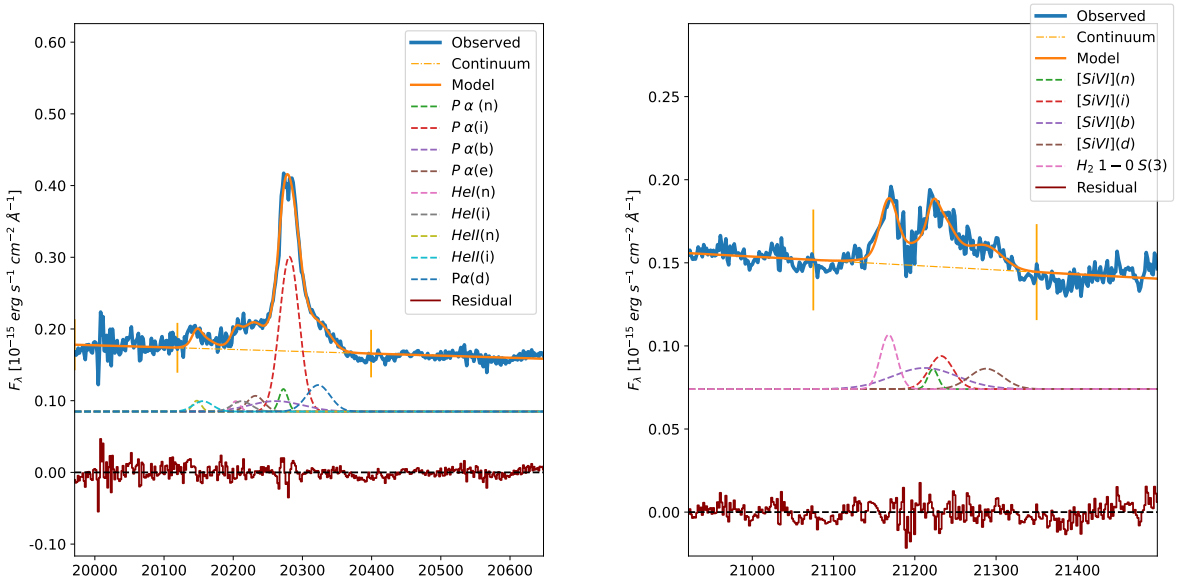

(a) Fits for Pa α, HeI (1869.1nm) and HeII (1863.7nm).

(b) Fits for [SiVI] and H_2 1-0 S(3).

Figure 16: Gaussian fits of Pa α, HeI[1869.1nm], HeII[1863.7nm], [SiVI] and H_2 1-0 S(3) for the J0802+25 EMIR spectrum.

Table 4: Emission line properties measured from the J0802+25 EMIR spectrum. Uncertainties from tied parameters are marked with *.

Line	Center (Å)	Flux $\times 10^{-15}$(erg cm^{-2} s^{-1})	FWHM (km/s)	Velocity (km/s)
Pa α (n)	20272.55±0.55	0.50±0.14	203	0±8
Pa α(i)	20281.20±0.55*	7.64±0.5	483	128±8*
Pa α(b)	20261.74±0.55*	1.40±1.13	1331	-160±8*
Pa α(e)	20232.00	0.66±0.54	414±233	-600
Pa α(d)	20322.92±2.67	1.58±0.3	585±84	744±39
HeI(n)	20203.60	0.23±0.04	204	19
HeI(i)	20212.21	0.51±0.04	485	147
$HeII$(n)	20147.38	0.24±0.04	204	-13
$HeII$(i)	20155.97	0.51±0.04	486	114
$[SiVI]\,(n)$	21222.3	0.19±0.05	192	-3
$[SiVI]\,(i)$	21232.3	0.7±0.1	483	139
$[SiVI]\,(b)$	21212.3	1.28±0.19	1331	-144
$[SiVI]\,(d)$	21287.66±3.42	0.63±0.09	678±74	919±48
$H_2\ 1-0\ S(3)$	21167.84±0.82	0.84±0.09	331±30	115±12
$H_2\ 1-0\ S(1)$	22943.98±0.63	1.19±0.07	409±19	124±8

This is not that rare of an occurrence in the context of spectra analysis of QSO2 outflows; components of a gas phase that aren't observed in certain wavelengths can be seen in others. It's worth remembering that while the distinction between gas phases made in this project has mainly been made about the ionized and molecular phases, these can be further subdivided, such as the warm and cold molecular gas. As an example, we might not be able to

see a cold molecular gas outflow in the K-band, but clearly see it when studying the CO emission of the quasar, and similar phenomena can occur in the ionized phase.

The estimated properties, presented in table 4, reproduce the results observed in the SDSS spectra (table 3) close to or within the uncertainty intervals, both the line width and relative velocity. The new measured extra component appears to be outflowing away from us at $\sim$ 770 km/s, and is estimated to be wider than the intermediate component, although with relatively large uncertainties. This same component is also detected in the [SiVI] line, with similar kinematics. The similarities between the velocities and widths of the (e) and (d) components suggest that they might be the receding and approaching sides of a biconical outflow, comprised of relatively undisturbed but very fast moving ionized gas.

The observed molecular component appears to be relatively narrow with an FWHM of $\sim$ 370 km/s if we average the values from both molecular lines, and is moving toward us with a velocity of $\sim$ 120 km/s, for which the estimates from both lines are in agreement. Given the fact that the molecular lines were fitted with a single component, and the relatively narrow width of the lines, we cannot confirm the presence of a molecular outflow, in spite of the line's centers suggesting a gas phase moving relative to the NLR.

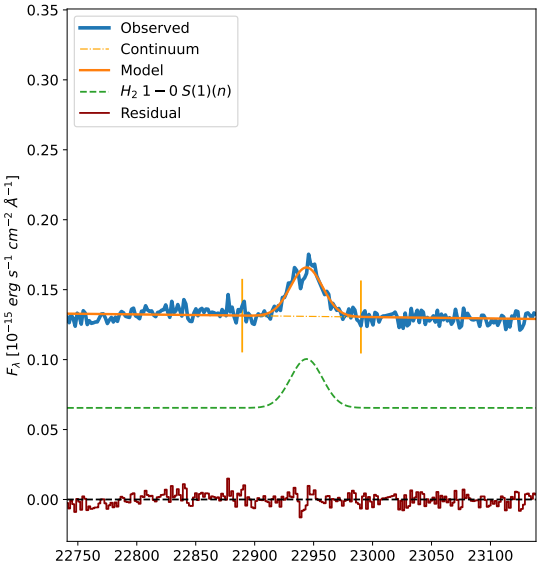

Figure 17: Gaussian fit of H_2 1-0 S(1) for the J0802+25 EMIR spectrum.

It's worth mentioning the difficulty of fitting this line profile due to the poor signal-to-noise ratio and very strong line blending; this results in the existence of multiple theoretical solutions that lead to similarly flat residuals. Consequently, most parameters had to either be tied or fixed altogether to prioritise solutions that reproduce what we observed in the SDSS spectrum. Nonetheless, the shape of the red wing of [SiVI] meant it was not possible to obtain a satisfying fit without adding a component that remains unobserved in the optical spectrum of J0802+25.

4.2 J0945+17

J0945+17 (SDSS identifier J094521.33+173753.2) is a QSO2 with a redshift of z=0.12834±0.00111 estimated from SDSS's 7th data release (Abazajian et al., 2009 [40]), and a luminosity of $L_{bol} = 10^{46.18}\ erg\,s^{-1}$. It's classified as a merging elliptical galaxy, and is now at the stage of post-coalescence (Pierce et al., 2022 [38]). The seeing during its observation was 1.4". The star used for calibration was BD+16 2159, an A2 spectral type star.

J0945+17 was primarily selected due to its ionized lines showing a clear blueshifted broad component, although it was also chosen due to it having been studied (Speranza et al. 2022, [24]) previously using the same spectrum. This means this object is interesting not only from a results standpoint, but also as a crosscheck. As the phase kinematics of this object were already known beforehand, studying this object will be a matter of being able to try and replicate those results.

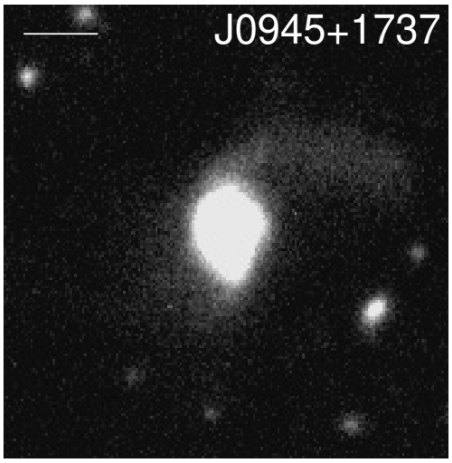

Figure 18: INT/WFC image of J0945+17 from J. Pierce et al., 2022[38]. There are visible signs of disturbance to the northeast of the galaxy's center.

4.2.1 SDSS spectrum

From the SDSS spectrum we observe both the intermediate and broad components to be blueshifted with respect to the narrow one (see figure 19).

Using the estimated parameters as initial guesses, a satisfying fit was quickly reached (figure 19), yielding an intermediate component of ionized gas outflowing at a velocity of $\sim$ 150 km/s, while the broad component appears to be faster, moving at $\sim$ 260 km/s. The width of the broad component is very large, clocking in at about $\sim$ 2000 km/s, so the gas it traces appears very perturbed. All parameters and their uncertainties are included in table 5.

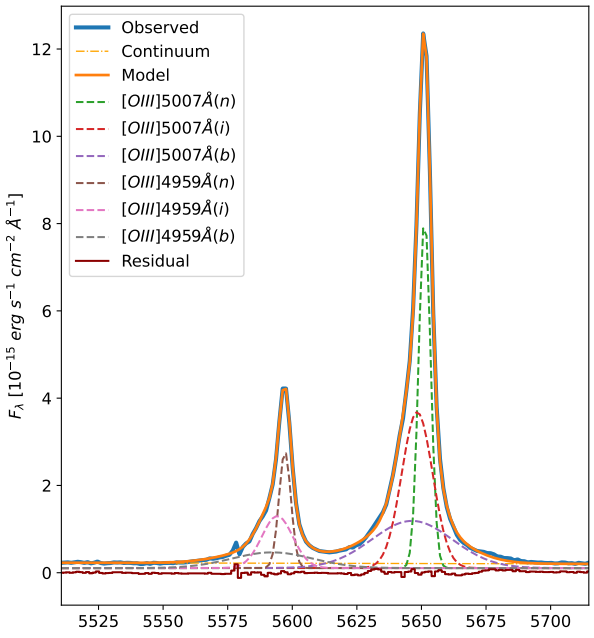

(a) Line profiles of OIII(4959Å) and OIII5007Å).

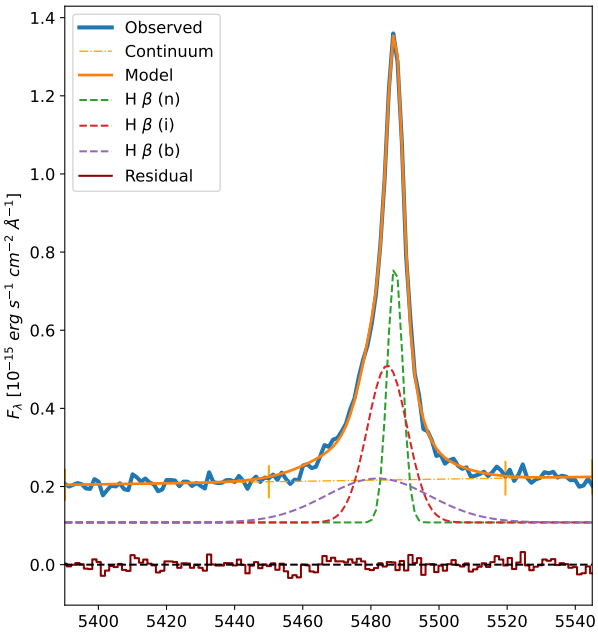

(b) Line profile of Hβ

Figure 19: Gaussian fits for the $H\beta$ and $[OIII]$ lines for the J0945+17 SDSS spectrum.

Table 5: Emission line properties measured from the J0945+17 SDSS spectrum. Uncertainties from tied parameters are marked with *.

Line	Center (Å)	Flux $\times 10^{-15}$(erg cm^{-2} s^{-1})	FWHM (km/s)	Velocity (km/s)
$[OIII]$ 5007Å(n)	5651.23±0.01	46.3±0.2	288±1	0±1
$[OIII]$ 5007Å(i)	5648.35±0.03	53.7±0.5	749±5	-153±2
$[OIII]$ 5007Å(b)	5646.34±0.08	42.2±1.1	1949±21	-260±4
$[OIII]$ 4959Å(n)	5597.16±0.01*	15.4±0.6	290±1*	5±1*
$[OIII]$ 4959Å(i)	5594.20±0.03*	17.9±0.2	757±5*	-153±2*
$[OIII]$ 4959Å(b)	5592.21±0.08*	14.1±0.4	1968±21*	-260±4*
H β(n)	5487.08±0.04	3.75±0.1	277	35±2
H β(i)	5484.82±0.14	5.88±0.2	747	-89±7
H β(b)	5481.98±0.58	4.30±0.2	1964	-244±32

For this particular case, only the widths of the H β components were fixed, since fixing the centers to the results obtained from the [OIII] estimates resulted in a bad fit. Although there are slight discrepancies between the results, specially in the case of the velocity of the intermediate component, they both suggest an outflowing ionized gas component.

4.2.2 EMIR spectrum

For the EMIR spectrum, the ionized tracers Pa α, HeI(1869.1nm), HeII(1863.7nm), [SiVI] and Br δ were observed, as well as the molecular line H_2 1-0 S(3) (see figure 13b). The line profiles are very similar to those observed in the SDSS spectrum, and a fit with three components similar to those observed in the optical results in flat residuals.

Table 6: Emission line properties measured from the J0945+17 EMIR spectrum. Uncertainties from tied parameters are marked with *.

Line	Center (Å)	Flux $\times 10^{-15}$(erg cm^{-2} s^{-1})	FWHM (km/s)	Velocity (km/s)
Pa α(n)	21163.99±0.18	3.77±0.19	274±9	0±3
Pa α(i)	21154.16±1.26	5.99±0.52	827±46	-139±18
Pa α(b)	21146.28	1.54±0.27	1340±235	-251
He I(n)	21093.98±4.08	0.38±0.15	275±10*	48±58
He I(i)	21084.19±5.00	0.59±0.35	830±47*	-92±71
He II(n)	21030.91±2.35	0.24±0.06	276±10*	17±34
He II(i)	21021.15±2.75	0.42±0.13	832±47*	-122±39
$[SiVI]$(n)	22152.87±0.63	0.57±0.13	166±28	-26±9
$[SiVI]$(i)	22143.38±2.94	1.80±0.38	565±82	-155±40
$[SiVI]$(b)	22134.40±0.63*	1.20±0.88	2094±852	-277±9*
Br δ(n)	21946.06±0.63*	0.20±0.05	168±28	-26±9*
Br δ(b)	21927.76±0.63*	0.30±0.24	2114±860*	-277±9*
$H_2\ 1-0\ S(3)$	22085.53±1.45	0.89±0.17	431±72	-51±20

This same spectrum was analyzed in Speranza et al., 2022 ([24]), and the resulting parameters (table 6) are in accordance to their results. The biggest discrepancy when compared to the SDSS spectrum is the width of the broad component of Pa α, although they are close to compatible results once the relatively large uncertainty of the measurement is taken into account.

Thanks in no small part to the remarkably good signal-to-noise ratio of this spectrum, particularly for Pa α, as well as the relatively weak blending of the H_2 line with [SiVI], it was possible to fit this profile with minimal constraints; no parameters besides the width of the broad component of Pa α were fixed, and only the broad component of [SiVI] and both components of Br δ were tied to other parameters.

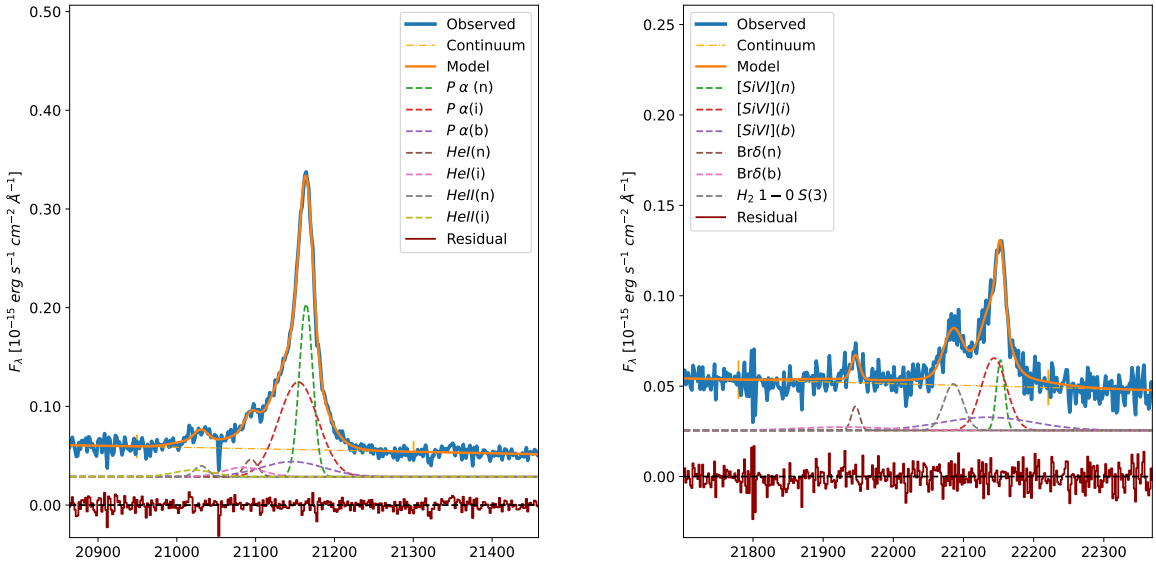

(a) Fits for Pa α, HeI (1869.1nm) and HeII (1863.7nm).

(b) Fits for [Si VI], Br δ and H_2 1-0 S(3).

Figure 20: Gaussian fits of Pa α, HeI[1869.1nm], HeII[1863.7nm], [Si VI], Br δ and H_2 1-0 S(3) for J0945+17.

The blueshifted intermediate and broad components are also observed in this spectrum (figure 20, and no additional components are seen in this case. With respect to the molecular line H_2 1-0 S(3), it has a measured width of $\sim$ 430 km/s and it traces a gas moving towards us with a velocity of $\sim$ 50 km/s, though this velocity measurement has an uncertainty of roughly half of its absolute value. Due to the molecular line being fit with a single component and its width being similar to that of the narrow component of the ionized lines, we report no clear outflowing warm molecular gas for J0945+17, as was reported by Speranza et al., 2022 ([24]).

Other observed discrepancies are those between the widths of the ionized components, since the narrow and intermediate component of [Si VI] are considerably more narrow than those of Pa α or the helium lines. These same discrepancies are also observed in aforementioned study.

4.3 J1034+60

J1034+60 (SDSS identifier J103408.57+600152.5) is a QSO2 with a redshift of z=0.05101±0.00117, estimated from spectroscopic measurements from SDSS's 7th data release (Abazajian et al., 2009 [40]), and a luminosity of $L_{bol} = 10^{45.98}\ erg\,s^{-1}$. It's morphologically classified as a merging elliptical, and is considered a post-coalescence system in terms of the visible disturbance. The seeing during its observation was 1". The star used for calibration was BD+60 1334, a G0 spectral type star.

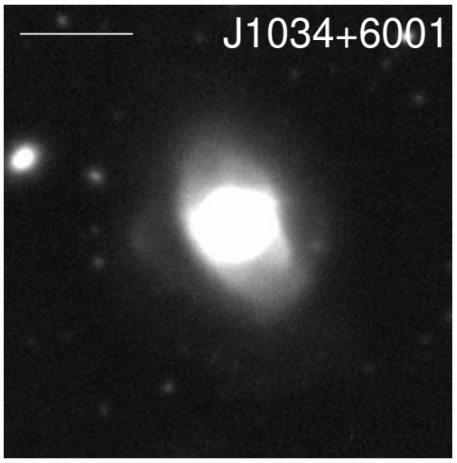

Figure 21: INT/WFC image of J1034+60 from J. Pierce et al., 2022[38].

This object was chosen due to the presence of broad ionized components and molecular lines in its spectrum (see figure 13c), as well as it having been studied in the optical range (P. Bessiere & C. Ramos, 2022 [41]). Aside from this, there was what appeared to be another component redwards of the center of the ionized lines, which appears as a visible bump in the red wing of the lines. The estimated velocities are similar for both the SDSS and EMIR spectra.

4.3.1 SDSS spectrum

The SDSS spectrum of J1034+60 was first fit using three components as per usual, but there was a noticeable bump corresponding to a relatively narrow line to the right of the center of the ionized line.

Table 7: Emission line properties measured from the J1034+60 SDSS spectrum. Uncertainties from tied parameters are marked with *.

Line	Center (Å)	Flux $\times 10^{-15}$(erg cm^{-2} s^{-1})	FWHM (km/s)	Velocity (km/s)
$[OIII]$ 5007AA(n)	5264.23±0.04	41.2±0.7	212±3	0±2
$[OIII]$ 5007AA(i)	5263.31±0.07	369±8	617±8	-53±4
$[OIII]$ 5007AA(b)	5259.17±3.22	42.8±9.2	1465±172	-289±184
$[OIII]$ 5007AA(e)	5280.48±5.27	15.3±0.1	487±332	924±299
$[OIII]$ 4959AA(n)	5213.80±0.04*	13.7±0.2	214±3*	2±2*
$[OIII]$ 4959AA(i)	5212.85±0.07*	123±3	623±8*	-53±4*
$[OIII]$ 4959AA(b)	5208.75±3.19*	14.3±3.1	1479±174*	-289±184*
$[OIII]$ 4959AA(e)	5229.79±4.12	5.1±3.7	492±334	920±236
$H\ \beta(n)$	5111.10	2.9±0.1	202	21
$H\ \beta(i)$	5110.20	32.8±0.1	615	-31
$H\ \beta(b)$	5107.40	4.48±0.27	1492	-196
$H\ \beta(e)$	5127.10	1.29	492	958

After adding a fourth component for both [OIII] lines and tying their amplitudes and widths, the resulting fit adjusted well to the line profile, and the same fit was used for H β, fixing the parameters to those found in the [OIII] lines. Some residuals remain around the center of [OIII]5007Å, but our model follow the line profile very precisely (figure 22).

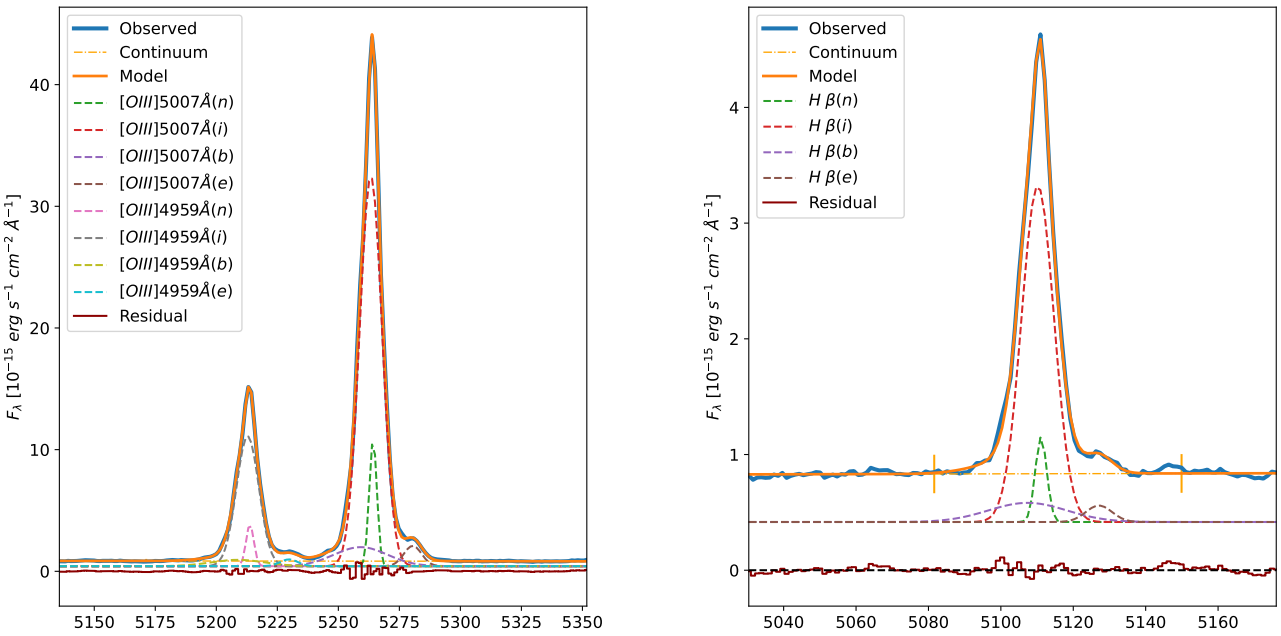

(a) Line profiles of OIII(4959Å) and OIII5007Å).

(b) Line profile of Hβ

Figure 22: Gaussian fits for the $H\beta$ and $[OIII]$ lines for the J1034+60 SDSS spectrum.

The estimated kinematics of the gas (see table 7) point to an intermediate component with an FWHM of $\sim$ 600 km/s, blueshifted with respect to the narrow line by about $\sim$ 50 km/s. The broad component's FWHM was measured at $\sim$ 1500 km/s, and it appears to be moving towards us at $\sim$ 200 km/s. The fourth component is receding from us at a velocity of $\sim$ 930 km/s and constitutes a relatively narrow line with and FWHM of $\sim$ 500 km/s. These measurements suggest an outflowing broad gas component moving in our direction, and a very rapid outflowing narrow component receding from us.

When comparing these results to the ones obtained by Bessiere & Ramos (2022, [41]), we need to account for the fact that the methodologies used in their study are considerably different, since they made use of integral field spectroscopy as opposed to the long slit spectroscopy utilized in this project. As such, the spectra we use, both optical and NIR, integrate all contributions from the entire galaxy into a single spectrum, while separating the emission into its spatial components results in a relatively different picture.

In spite of this, the outflow velocities reported in their study are considerably similar to our own, and the fact that we can observe gas both approaching and receding from us is in accordance to the estimated gas velocity maps; conversely, the width of the broad component is fairly smaller as according to their estimates (ranging from $\sim$ 700 km /s to $\sim$ 1000 km/s). This is due to our spectrum blending two narrow components into a single broader line, while what they refer to as the "broad" component is what we identify as the intermediate component in our data.

4.3.2 EMIR spectrum

For J1034+60, the observed lines in the EMIR spectrum were the ionized lines [SiVI], Br δ, Br γ, HeI(2058.7nm) and the molecular lines H_2 1-0 from S(1) to S(3) (see figure 13c). It was possible to fit the four observed components in the SDSS spectrum to the [SiVI] line (figure 23), which presented the highest signal of all lines in the EMIR spectrum. Conversely, the low amplitude observed in the profiles of Br δ and HeI(2058.7nm) meant it was only possible to fit the narrow component, while Br γ was fit using a narrow, intermediate and broad component. All three molecular lines appear to trace a single gas component.

The widths of the ionized components were fixed to the values estimated from the SDSS spectrum, in order to obtain a good fit and because they trace the same gas. The estimated kinematics (table 8) agree with the measurements from the SDSS spectrum (table 7) for all four components in the case of [SiVI]. The molecular lines trace a narrow gas (350-500 km/s) although there are considerable discrepancies and uncertainties in the measurements of their widths, in the case of S(1) and S(2) because of their relatively low signal and in the case of S(3) due to blending with [SiVI]. Nonetheless, they were all fit with a single gaussian function in order to produce flat residuals.

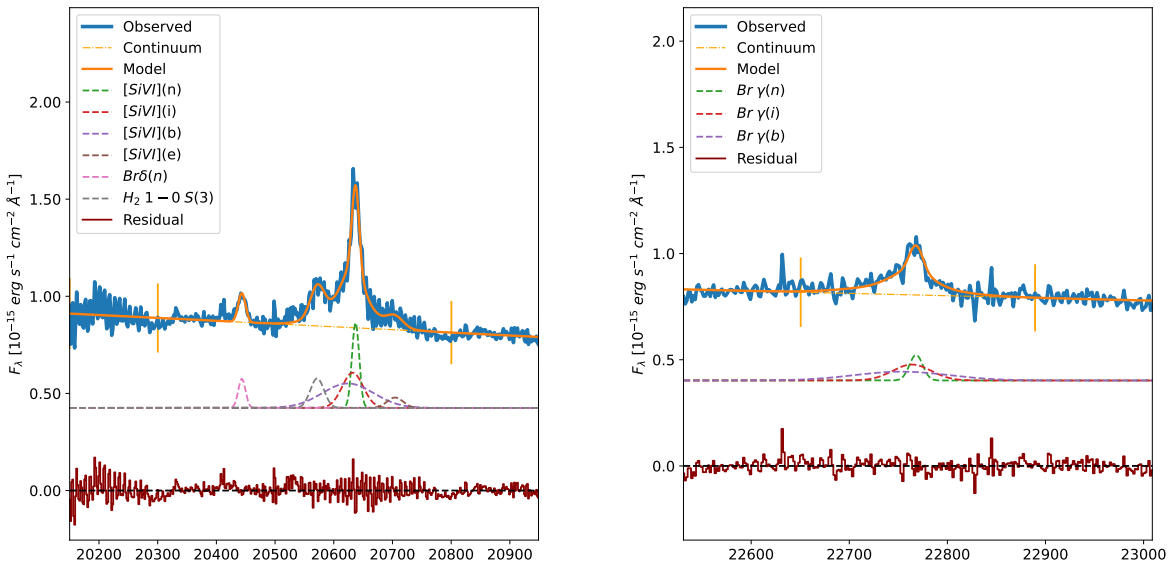

(a) Fits for Br δ, [SiVI] and H_2 1-0 S(3).

(b) Fits for Br γ.

Figure 23: Gaussian fits of Br δ, [SiVI] and H_2 1-0 S(3) and Br γ for the J1034+60 SDSS spectrum.

Table 8: Emission line properties measured from the J1034+60 EMIR spectrum.

Line	Center (Å)	Flux $\times 10^{-15}$(erg cm^{-2} s^{-1})	FWHM (km/s)	Velocity (km/s)
$[SiVI]$(n)	20637.13±0.49	6.8±0.5	192	0±7
$[SiVI]$(i)	20632.24±1.93	8.1±1.7	605	-71±28
$[SiVI]$(b)	20624.16	13.8±2.3	1492	-189
$[SiVI]$(e)	20704.45±6.72	1.83±1.14	458±218	976±97
$Br\delta(n)$	20443.38±1.35	2.31±0.3	194	-16±20
H_2 1 − 0 $S(3)$	20571.72±1.81	4.4±0.5	392	-63±26
H_2 1 − 0 $S(2)$	21374.57±1.64	3.3±0.5	519±68	-32±23
H_2 1 − 0 $S(1)$	22301.98±0.78	4.6±0.4	353±23	3±10
$Br\ \gamma(n)$	22768.09	2.1±0.3	211	6
$Br\ \gamma(i)$	22763.88	3.7±0.8	612	-49
$Br\ \gamma(b)$	22753.37	5.0±0.9	1495	-188
HeI	21637.50±1.38	2.22±0.3	367±38	-13±19

The measured velocities from the molecular gas present a similar situation, with the velocity estimation from H_2 1-0 S(1) being in discrepancy with the other two lines. Again, low signal and line blending are to blame for the large uncertainties. In this case, the narrow width of the lines ($\sim$ 400 km/s) and the very low velocities suggest this molecular emission is originated in the NLR and no warm molecular outflow is detected.

The brightest line in this spectrum, [SiVI], happened to lay in the middle of a telluric absorption band, which was subject to high frequency noise during our observations. Nonetheless, the correction allowed us to retrieve a line profile that faithfully represents what was observed in the SDSS spectrum, serving as proof of the correctness of our procedure.

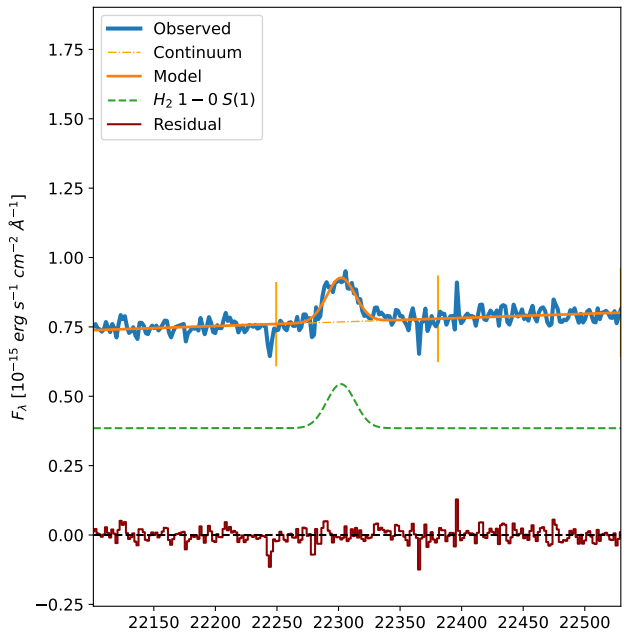

(a) Gaussian fit of H_2 1 − 0 $S(1)$.

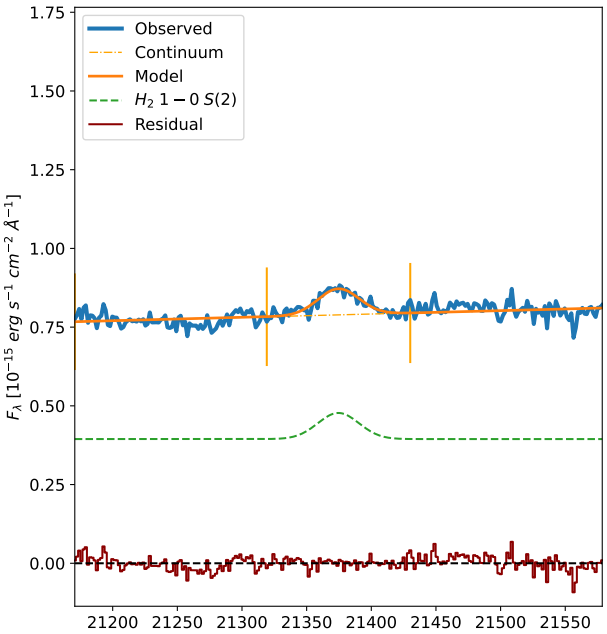

(b) Gaussian fit of H_2 1 − 0 $S(2)$

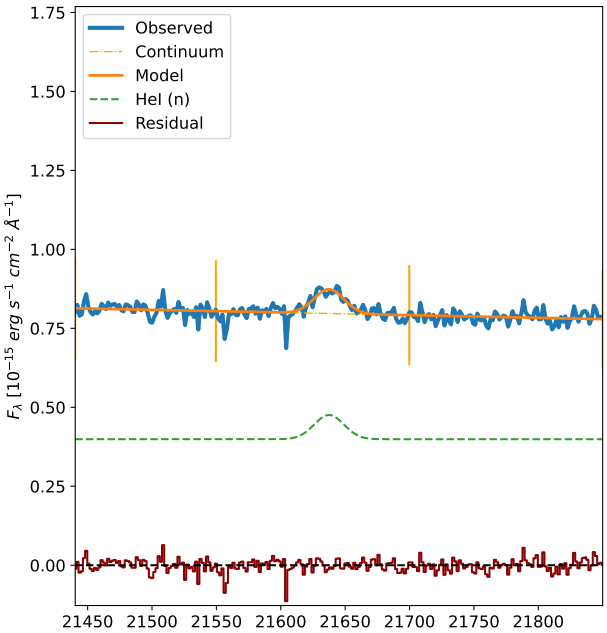

(c) Gaussian fit of HeI

Figure 24: Gaussian fits for the molecular lines H_2 $1-0$ $S(1)$, H_2 $1-0$ $S(2)$ and HeI for the J1034+60 EMIR spectrum.

4.4 J1440+53

J1440+53 (SDSS identifier J144038.09+533016.2) is a QSO2 with a redshift of z=0.03761±0.00144 estimated spectroscopic measurements from SDSS's 7th data release (Abazajian et al., 2009 [40]), and a luminosity of $L_{bol} = 10^{46.07}\ erg\,s^{-1}$. It's also included in the Markarian galaxy survey of UV excess sources, with identifier Mrk 477. It is classified as an elliptical galaxy in the stage of pre-coalescence. The seeing during observations was 0.8". The comparison star used was HD 238495, an A5 spectral type star.

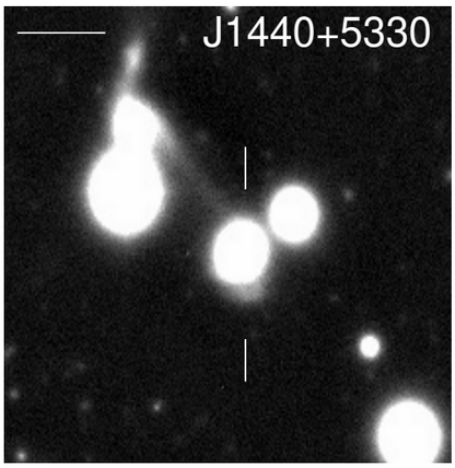

Figure 25: INT/WFC image of J1440+53 from J. Pierce et al., 2022[38].

J1440+53 was selected due to it presenting both broad components on its ionized lines as well as various molecular lines, and overall, a very rich emission-line spectrum (see figure 13d). Of all the observed objects, we were able to identify the largest amount of molecular lines (4) in its spectrum.

4.4.1 SDSS spectrum

The shape of the lines observed in the SDSS spectrum (see figure 26) made it clear the underlying broad component was blueshifted; a satisfying fit with three components was quickly reached for the [OIII] lines, and H β followed suit.

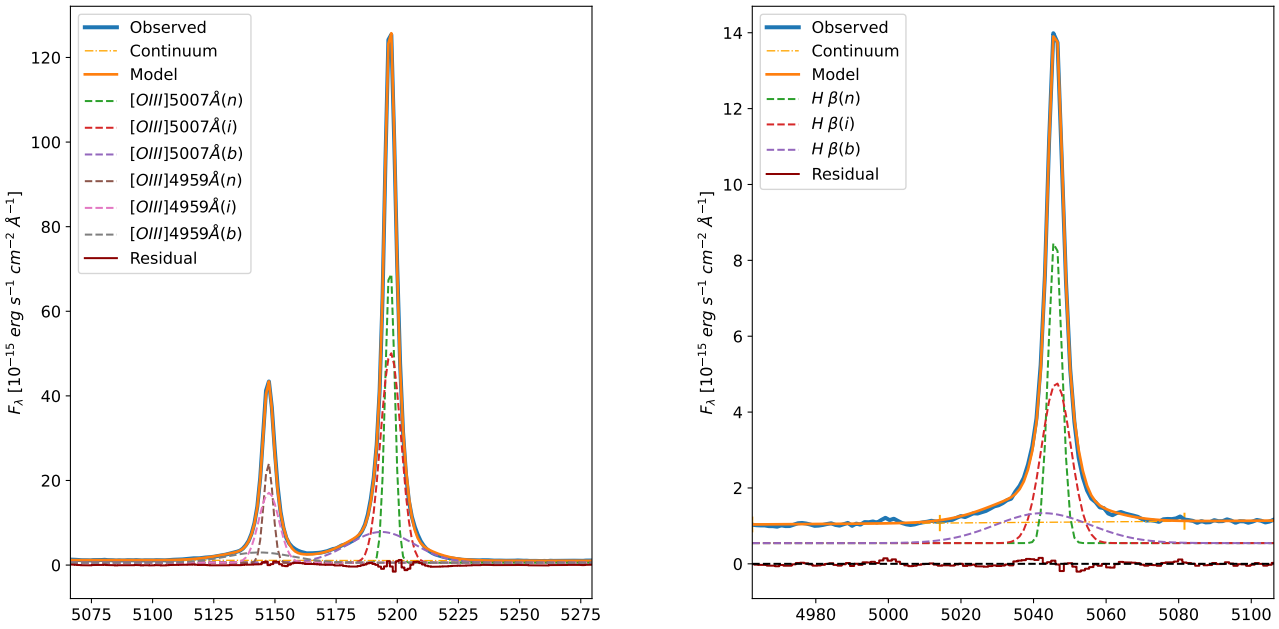

(a) Line profiles of OIII(4959Å) and OIII5007Å).

(b) Line profile of Hβ

Figure 26: Gaussian fits for the $H\beta$ and $[OIII]$ lines for the J1440+53 SDSS spectrum.

The fit parameters suggest a fast-moving ($\sim$ 200 km/s) and considerably disturbed (FWHM $\sim$ 1800 km/s) outflowing component of the ionized gas, while the intermediate component appears slightly redshifted from the center of the narrow line. With J1440+53 being the closest object, we observe the highest [OIII] and H β fluxes in its spectrum.

Table 9: Emission line properties measured from the J1440+53 SDSS spectrum. Uncertainties from tied parameters are marked with *.

Line	Center (Å)	Flux $\times 10^{-15}$(erg cm^{-2} s^{-1})	FWHM (km/s)	Velocity (km/s)
$[OIII]$ 5007Å(n)	5197.030±0.002	341.8±2.3	261±1	0±1
$[OIII]$ 5007Å(i)	5197.328±0.003	513.4±4.6	561±3	17±1
$[OIII]$ 5007Å(b)	5193.51±0.07	244.7±3.2	1820±10	-203±4
$[OIII]$ 4959Å(n)	5147.289±0.005	113.9±0.7	263±1*	5±1
$[OIII]$ 4959Å(i)	5147.512±0.008	171.2±1.5	566±3*	18±1
$[OIII]$ 4959Å(b)	5143.724±0.07*	81.4±1.1	1838±10*	-203±4*
$H\ \beta(n)$	5045.96	38.2±0.2	245	28
$H\ \beta(i)$	5046.26	42.4±0.4	554	46
$H\ \beta(b)$	5042.56	25.9±0.6	1832	-174

The widths of all three components of [OIII]4959Å as well as the center of the broad component were tied to [OIII]5007Å, and so were both the centers and widths of all components of H β.

4.4.2 EMIR spectrum

The EMIR spectrum of J1440+53 was the most populated in terms of spectral features, with a total of 8 lines, 4 of them tracing the ionized gas and the other 4, molecular H_2 tracers (figure 13d). We observe [SiVI], Br δ, Br γ, HeI(2058.7nm) and H_2 1-0 S(0) through S(3).

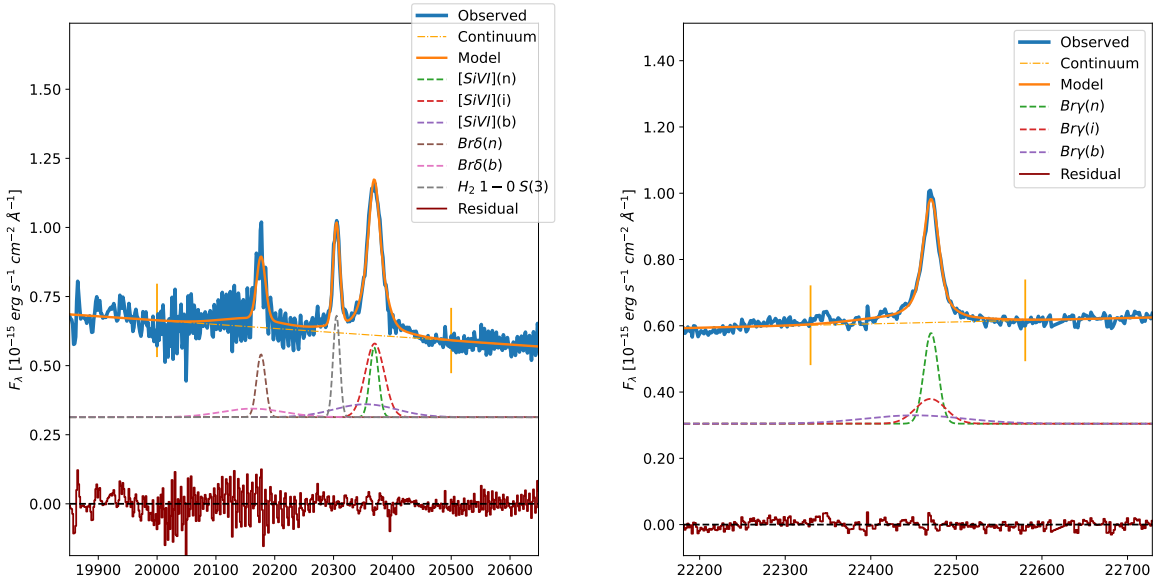

(a) Fits for Br δ, [SiVI] and H_2 1-0 S(3).

(b) Fits for Br γ.

Figure 27: Gaussian fits of Br δ, [SiVI] and H_2 1-0 S(3) and Br γ for the J1440+53 EMIR spectrum.

In terms of signal-to-noise ratio, the Br δ line (figure 27) presented the most problems despite J1440+53 having the highest overall signal on the entire subset of objects. This was due to its wavelength coinciding with a telluric absorption band, as a high frequency noise present in the blue end of the spectrum clearly affected the line profile. In spite of the correction performed in order to minimize the impact of this noise, it is still noticeable. This is part of the reason why, despite the broad component having lower amplitude and total flux than the intermediate in, for example, the [SiVI] line, the former is detected while the latter isn't.

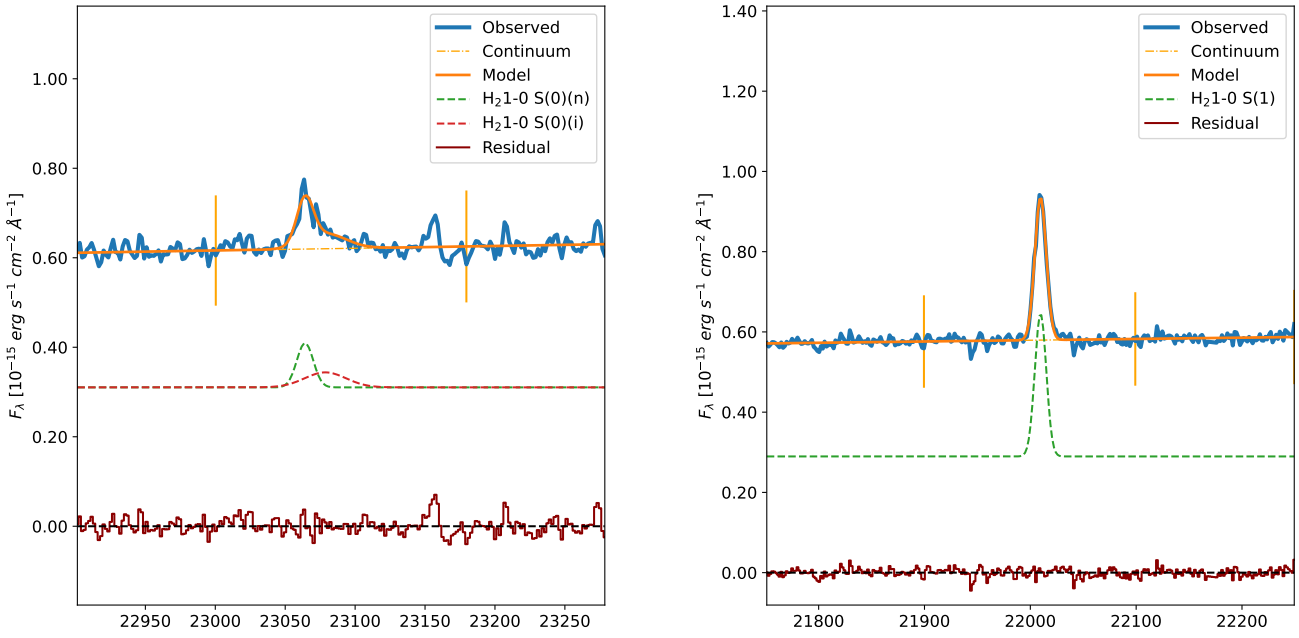

(a) Gaussian fit of H_2 $1-0$ $S(0)$.

(b) Gaussian fit of H_2 $1-0$ $S(1)$

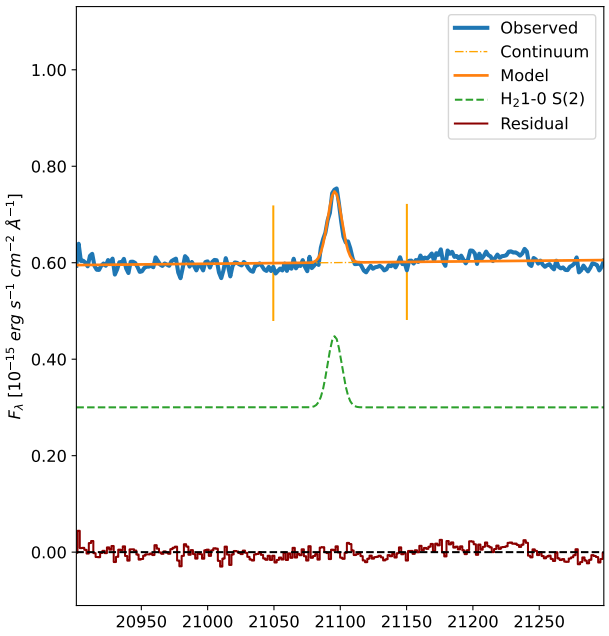

(c) Gaussian fit of H_2 $1-0$ $S(2)$.

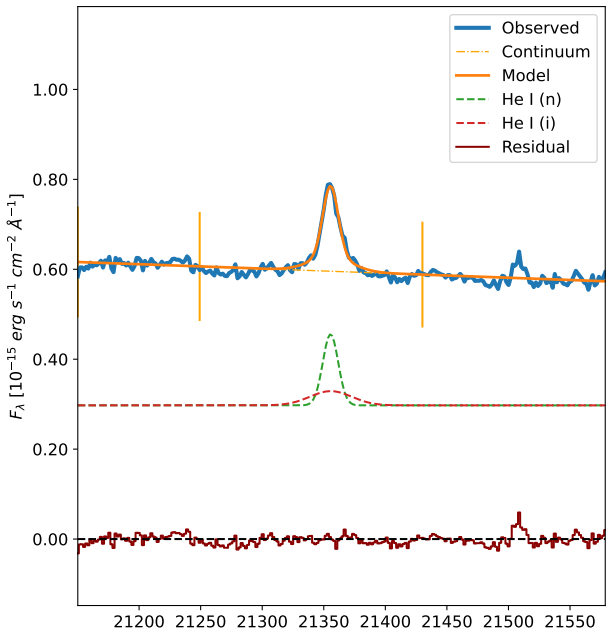

(d) Gaussian fit of HeI

Figure 28: Gaussian fits for the molecular lines H_2 1-0 S(0) to S(2) and the low ionization line HeI(2058.7nm) for the J1440+53 EMIR spectrum.

The rest of the observed lines all present comparably higher signal-to-noise ratio, and the models very clearly represent the line profiles. We estimate very similar kinematics to those in the SDSS spectrum for all the observed ionized lines, both in terms of FWHM and relative velocity of the gas (see tables 9 and 10). Most parameters in the [SiVI] profile had to be fixed to represent the profiles observed in SDSS, mostly due to blending with the H_2 line.

Table 10: Emission line properties measured from the J1440+53 EMIR spectrum. Uncertainties from tied parameters are marked with *.

Line	Center (Å)	Flux $\times 10^{-15}$(erg cm^{-2} s^{-1})	FWHM (km/s)	Velocity (km/s)	
$[SiVI]$(n)	20369.06±0.61	4.8±0.6	246	0±9	
$[SiVI]$(i)	20369.89	10.8±1.1	554	12	
$[SiVI]$(b)	20353.93	6.2±1.3	1833	-223	
$Br\delta(n)$	20176.70	4.3±0.3	248	-33	
$Br\delta(b)$	20161.71±0.60*	4.1±0.7	1851	-255±9*	
$Br\gamma(n)$	22470.42±0.18	5.70±0.19	246	-20±2	
$Br\gamma(i)$	22469.82	3.4±0.4	554	-28	
$Br\gamma(b)$	22451.26	3.7±0.3	1833	-276	
$H_2$1-0 S(3)	20304.89±0.36	5.2±0.5	177±14	-57±5	
$H_2$1-0 S(2)	21095.77±0.28	1.97±0.15	178±11	-49±4	
$H_2$1-0 S(1)	22009.64±0.10	4.83±0.10	174±3	-34±1	
$H_2$1-0 S(0)(n)	23064.19±0.70	1.5±0.2	158	-39±9	
$H_2$1-0 S(0)(i)	23078.68±10.10	1.24	1.20	443±415	149±131
He I (n)	21355.46±0.31	2.5±0.3	188±20	-28±4	
He I (i)	21355.68±2.79	1.4±0.4	554	-25±39	

All molecular lines were fit with a single gaussian function with the exception of $H_2$1-0 S(0); the widths and velocities were very for S(1) through S(3) and the narrow component of S(0). This is the only case in which we detect a second component in a molecular line, and only tentatively so; the uncertainties in the measurements of the flux, FWHM and relative velocity are all of the magnitude of the measurement. This, combined with the fact that this component is not observed in any of the other molecular lines, which are of higher or similar S/N to S(0), means it

is not possible to clearly confirm the presence of a warm molecular outflow in J1440+53. Nonetheless, the measured values of the FWHM and velocity, however large their uncertainties may be, are compatible with what is expected from warm molecular outflows.

4.5 J1455+32

J1455+32 (SDSS identifier J145519.41+322601.8) is a type 2 quasar galaxy with a redshift of z=0.08736 ±0.00002, estimated from spectroscopic measurements from SDSS's 8th data release (Aihara et al., 2011 [42]), and a luminosity of $L_{bol} = 10^{45.77}\ erg\,s^{-1}$. Its morphological classification is uncertain, with the most voted classes being spiral and elliptical, and it shows signs of disturbance, classified as a state of post-coalescence (Pierce et al., 2022 [38]). The seeing during the observation used for this analysis was 0.8". The other observation was not used in this case, since the signal-to-noise ratio was much poorer and the difference in conditions (seeing was 1.2" for the 2018B observation) meant it wasn't feasible to combine the spectra from both observations. The comparison star used was BD+33 2599, a G0 spectral type star.

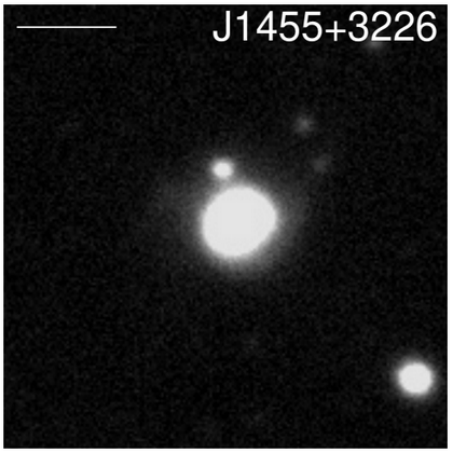

Figure 29: INT/WFC image of J1455+32 from J. Pierce et al., 2022[38]. Signs of disturbance are visible to the west of the galaxy's center.

J1455+32 was selected because it showed signs of outflowing ionized gas, as the visible lines were particularly wider towards the blue end of the spectrum (see figure 13e). It was also selected because a molecular gas tracer, H_2 1-0 S(3), was present, meaning a simultaneous characterization of both gas phases was possible.

4.5.1 SDSS spectrum

The SDSS spectrum showed what was visible in the ionized gas lines of the EMIR spectrum, that is, a broadened component bluewards of the amplitude peak. The [OIII] lines were fit first, and the resulting parameters were then used for the fitting of H β (see figure 30). We find an intermediate component which is moving away from us at $\sim$ 100 km/s in the direction of our LOS, and a broader component moving at a very similar velocity, but in our direction. These components are found in all three lines.

Table 11: Emission line properties measured from the J1455+32 SDSS spectrum. Uncertainties from tied parameters are marked with *.

Line	Center (Å)	Flux $\times 10^{-15}$(erg cm^{-2} s^{-1})	FWHM (km/s)	Velocity (km/s)
$[OIII]$5007Å(n)	5444.74±0.01	26.0±0.4	311±3	0± 1
$[OIII]$5007Å(i)	5446.68±0.13	48.6±3.4	811±18	107± 7
$[OIII]$5007Å(b)	5442.88±1.34	15.9±4.7	1260±67	-102 ± 74
$[OIII]$4959Å(n)	5392.63±0.03*	8.66±0.14	314±3*	5 ± 1*
$[OIII]$4959Å(i)	5394.47±0.13*	16.2±1.1	819±18*	107 ± 7*
$[OIII]$4959Å(b)	5390.70±1.32*	5.3±1.6	1272±67*	-102 ± 74*
H β(n)	5286.37	2.15±0.06	288	22
H β(i)	5288.37	3.84±0.14	797	136
H β(b)	5284.57	0.83±0.15	1270	-80

The fit parameters can be found in table 11. For the first fit, the FHWM of the different components [OIII] were tied together, and the relative velocity of the broad component [OIII]4959Å was also tied to that of [OIII]5007Å to improve the fit.

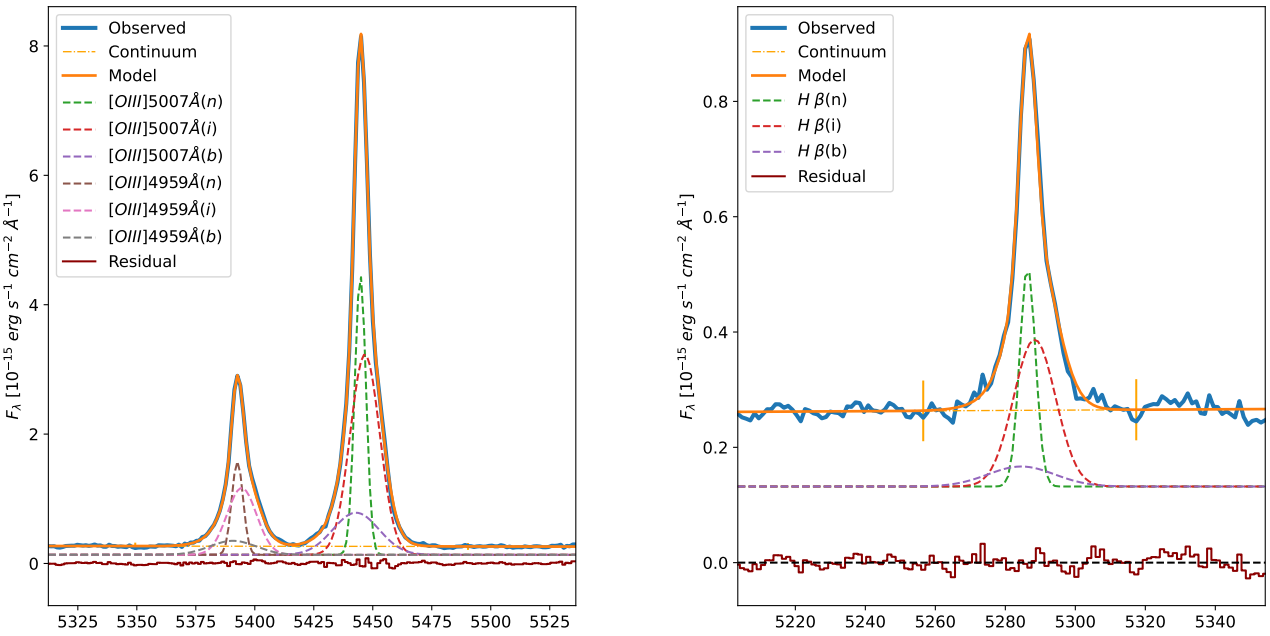

(a) Line profiles of OIII(4959Å) and OIII5007Å).

(b) Line profile of Hβ

Figure 30: Gaussian fits for the $H\beta$ and $[OIII]$ lines for the J1455+32 SDSS spectrum.

The estimated parameters suggest we are observing both the approaching and receding sides of an ionized outflow, with different widths ($\sim$ 810 km/s for the receding component and $\sim$ 1260 km/s for the approaching component) and similar relative velocities of $\sim$ 100 km/s.

4.5.2 EMIR spectrum

The EMIR spectrum of J1455+32 contained various ionized gas tracer lines, but only a single molecular tracer. Three components were used to fit both Pa α and [SiVI], while He I, He II and Br δ were fit with only a narrow and intermediate component and the molecular line H_2 1-0 S(3) only needed a narrow component to be fitted (figure 31).

Table 12: Emission line properties measured from the J1455+32 EMIR spectrum. Uncertainties from tied parameters are marked with *.

Line	Center (Å)	Flux $\times 10^{-15}$(erg cm^{-2} s^{-1})	FWHM (km/s)	Velocity (km/s)
Pa α(n)	20385.02±0.46	0.81±0.06	272	0±7
Pa α(i)	20391.77±2.21	1.08±0.19	742	99±33
Pa α(b)	20378.18	0.66±0.20	1164	-101
He I(n)	20315.11	0.052±0.005	273	11
He I(i)	20321.84±2.32*	0.14±0.01	744	110±34*
He II(n)	20256.40	0.052±0.007	274	11
He II(i)	20263.11±2.31*	0.22±0.05	747	110±34*
$[SiVI]$(n)	21341.32±1.58	0.17±0.03	298	27±22
$[SiVI]$(i)	21348.16	0.12±0.14	807	123
$[SiVI]$(b)	21334.16	0.36±0.17	1266	-73
Br δ(n)	21142.37±3.89	0.043±0.015	302	31±55
Br δ(i)	21149.14±4.02	0.077±0.005	815	127±57
H_2 1-0 S(3)	21278.71±4.13	0.1±0.08	303±238	35±58

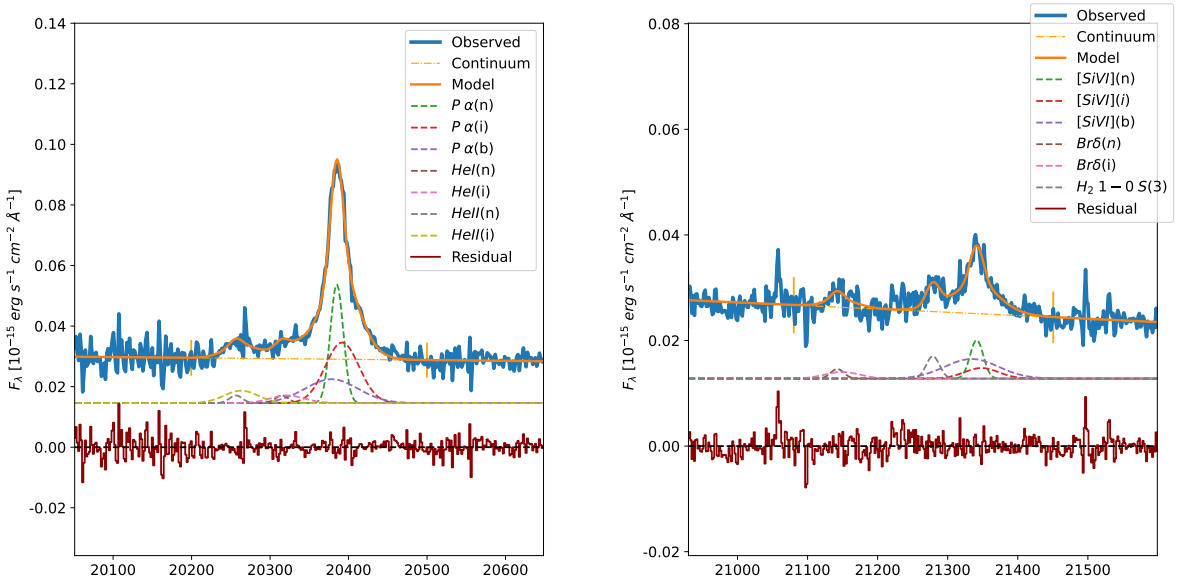

(a) Fits for Pa α, HeI (1869.1nm) and HeII (1863.7nm).

(b) Fits for Br δ, [SiVI] and H_2 1-0 S(3).

Figure 31: Gaussian fits of Pa α, HeI[1869.1nm], HeII[1863.7nm], Br δ, [SiVI] and H_2 1-0 S(3) for the J1455+32 EMIR spectrum.

After obtaining close to flat residuals, we confirm the findings from the SDSS spectrum. For all fits except H_2 1-0 S(3), the line widths were fixed. Additionally, the central wavelengths of the broad component of Pa α and of the intermediate and broad components of [SiVI] were fixed as well, to obtain a better fit. As is the case for some of the spectra with lower signal-to-noise ratios, many different combinations of Gaussian functions might yield relatively flat residuals; it's in those cases where the line properties measured using SDSS are of extreme value.

The molecular gas appears as a relatively undisturbed component, with FWHM similar to that of the narrow component of the ionized lines, while its relative velocity carries a considerably large uncertainty and includes zero in its uncertainty interval (see table 10).. These findings suggest the molecular emission is originated in the NLR and no clear outflowing war molecular gas is observed.

4.6 J1713+57

J1713+57 (SDSS identifier J171350.32+572954.9) is QSO2 with a redshift of z=0.11272 ± 0.00112 estimated from spectroscopic measurements from SDSS's 7th data release (K. Abazajian et al,. 2009 [40]), and a luminosity of $L_{bol} = 10^{46.12}\ erg\ s^{-1}$. It's morphologically classified as an elliptical galaxy and shows no signs of current disturbance due to merger processes (Pierce et al., 2022 [38]).

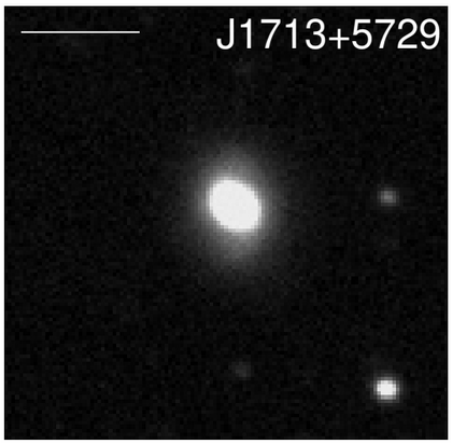

Figure 32: INT/WFC image of J1713+57 from J. Pierce et al., 2022[38]. The galaxy appears as a regular elliptical, showing no clear signs of disturbances.

The seeing during observation was 0.8" for the 2018A OB, 1.0" for the first 2019A OB and 0.9" for the second. The third 2019A observation presented very poor signal-to-noise ratio as well as worse seeing, at 1.1", so it wasn't used for the final analysis. The comparison star used for both 2018A and 2019A observations was HD 238926, an A5 spectral type star.

J1713+57 was selected as part of our final sample due to it showing clear broadened components, although the lines observed in EMIR appeared quite symmetrical, indicating the presence of low-velocity turbulent gas (see figure 13f).

4.6.1 SDSS spectrum

Table 13: Emission line properties measured from the J1713+57 SDSS spectrum. Uncertainties from tied parameters are marked with *.

Line	Center (Å)	Flux $\times 10^{-15}$(erg cm^{-2} s^{-1})	FWHM (km/s)	Velocity (km/s)
$[OIII]$5007Å(n)	5573.03±0.01	27.2±0.3	413±3	0±1
$[OIII]$5007Å(i)	5573.47±0.03	66.5±1.2	1242±18	24±2
$[OIII]$5007Å(b)	5572.30±0.35	27.9±2.6	2627±75	-39±19
$[OIII]$4959Å(n)	5519.72±0.03*	9.08±0.10	417±3*	6±2
$[OIII]$4959Å(i)	5520.04±0.03*	22.2±0.4	1254±18*	24±2*
$[OIII]$4959Å(b)	5518.88±0.35*	9.3±0.9	2653±76*	-39±19*
H β(n)	5410.62	1.87±0.10	391	5
H β(i)	5411.02	5.4±0.4	1199	27
H β(b)	5409.82	2.3±0.5	2605	-39

The analysis of J1713's SDSS spectrum was relatively simple, with the lines being fully characterized by 3 components of different amplitudes and widths, but very similar central wavelengths. The $[OIII]$ lines were fit first, since their signal to noise ratio is roughly twice that of $H\beta$, and the parameters from the aforementioned fit were used for fitting $H\beta$. As is visible in figure 33, all 3 components of each line are really close in terms of wavelength, with the intermediate component being responsible for most of the line's total flux.

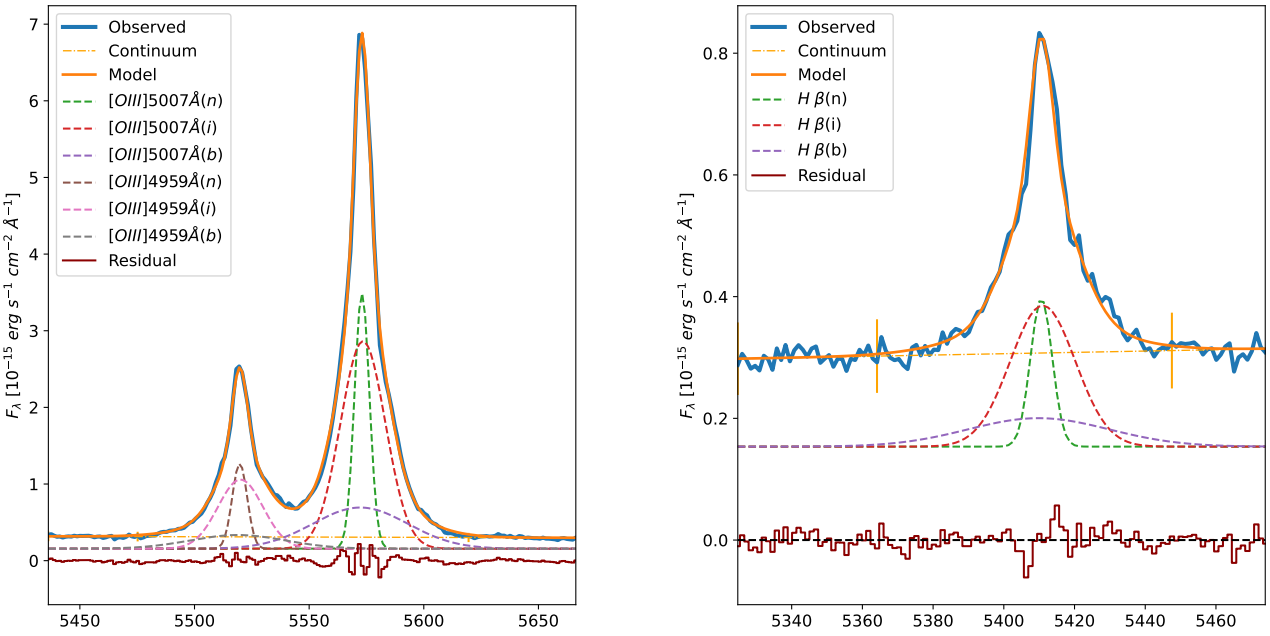

(a) Line profiles of OIII(4959Å) and OIII5007Å).

(b) Line profile of Hβ

Figure 33: Gaussian fits for the $H\beta$ and $[OIII]$ lines for the J1713+57 SDSS spectrum.

The fit parameters can be found in table 13. The estimated velocities for both the intermediate and broad component are small enough to include zero within their respective error interval, meaning we find no clear evidence of fast outflowing ionized gas in our line of sight in this case, despite clearly observing broad components in the emission lines.

4.6.2 EMIR spectrum

Similar to the case for the optical spectrum, we find three components for Pa α and two for each helium line, since these are much dimmer and the contribution from the broad component is too small to be clearly detected (see figure 34). The parameters obtained for this fit, presented in table 14 are very similar to those obtained for the SDSS spectrum. Both the widths of all components and the central wavelengths of the narrow components of both helium lines were fixed before fitting. The relative velocities measured for these lines are compatible with those measured in the SDSS spectrum within their uncertainty intervals.

Regarding the analysis of the ionized gas tracers [SiVI] and Br δ, we find applying similar restrictions as those used for Pa α and the helium lines yield similar results, in spite of the lines' lower S/N ratio. These lines are analyzed alongside a molecular gas tracer, H_2 1-0 S(3), which we can use to estimate the blueshift of the molecular phase. This line is fit with a single component, as will be the case for the rest of H_2 lines for this object (see figure 35). Like the ionized component, the molecular phase seems to be moving quite slowly relative to our line of sight.

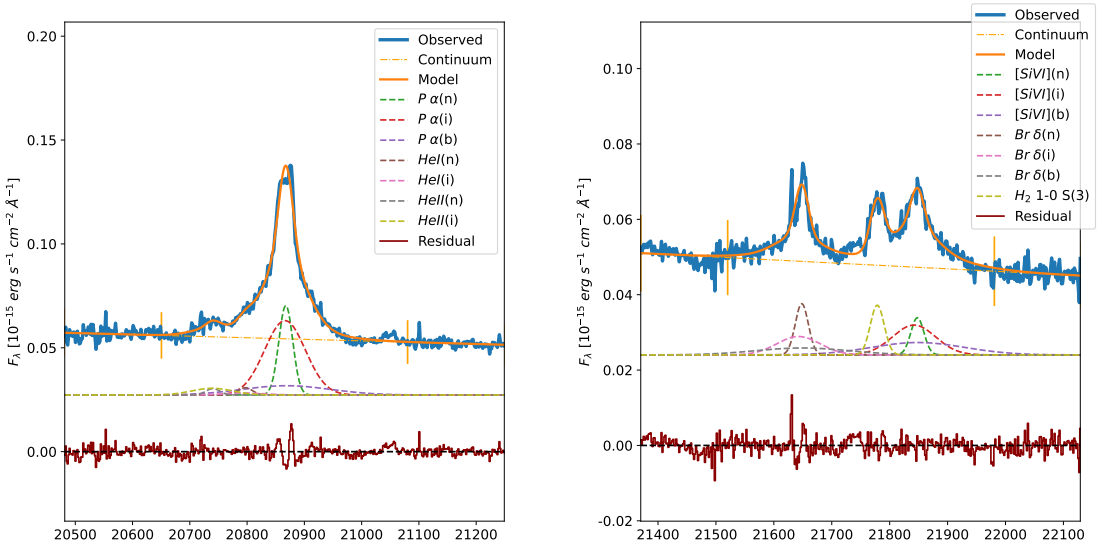

(a) Fits for Pa α, HeI (1869.1nm) and HeII (1863.7nm).

(b) Fits for Br δ, [SiVI] and H_2 1-0 S(3).

Figure 34: Gaussian fits of Pa α, HeI[1869.1nm], HeII[1863.7nm], Br δ, [SiVI] and H_2 1-0 S(3) for the J1713+57 EMIR spectrum.

Both the intermediate and broad components seem to trace a considerably disturbed gas phase, with the intermediate component having an FWHM of $\sim$ 1200 km/s and the broad $\sim$ 2600 km/s, which is the overall highest FHWM observed for these components in the entire subset of objects studied in this project. This, combined with very strong line blending (see figure 34) is the reason behind the large uncertainties in the measurement of both line component centers and, as a direct consequence, relative velocities.

Table 14: Emission line properties measured from the J1713+57 EMIR spectrum. Uncertainties from tied parameters are marked with *.

Line	Center (Å)	Flux $\times 10^{-15}$(erg cm^{-2} s^{-1})	FWHM (km/s)	Velocity (km/s)
Pa α(n)	20867.59±0.26	1.31±0.04	402	0±4
Pa α(i)	20866.20±0.81	3.19±0.12	1200	-20±12
Pa α(b)	20868.34	0.86±0.18	2605	11
He I(n)	20797.12	0.11±0.03	403	27
He I(i)	20795.74±0.95*	0.086±0.088	1204	7±14
He II(n)	20740.37	0.095±0.032	404	11
He II(i)	20738.99±0.95*	0.29±0.07	1208	-9±14*
$[SiVI]$(n)	21847.83±1.08	0.28±0.05	354±43	-34±15
$[SiVI]$(i)	21842.03±4.04	0.74±0.17	1200	-114±55
$[SiVI]$(b)	21848.83	0.67±0.20	2605	-20
Br δ(n)	21648.24±0.87	0.38±0.05	357±44	27±12
Br δ(i)	21642.49±4.18*	0.46±0.01	1211	-53±58*
Br δ(b)	21649.22±1.20*	0.37±0.08	2629	40±17*
H_2 1-0 S(3)	21778.56±0.89	0.40±0.04	377±32	-98±12
H_2 1-0 S(1)	23610.75±1.59	0.43±0.07	403±49	-29±20
H_2 1-0 S(2)	22628.90±.03	0.19±0.03	454±44	-63±27

To complete our study of the molecular component of the gas, we use the H_2 $1-0$ $S(1)$ and H_2 $1-0$ $S(2)$ lines as tracers. Both lines are fit with a single Gaussian function (figure 35), yielding similar widths to that of the narrow component of the ionized lines. From their velocities relative to the narrow component of Pa α, we confirm what we found from studying H_2 $1-0$ $S(3)$, which is that the warm molecular gas responsible for the emission of these lines is moving very slowly in our line of sight, similar to the ionized component; as such, no warm molecular outflow is detected.

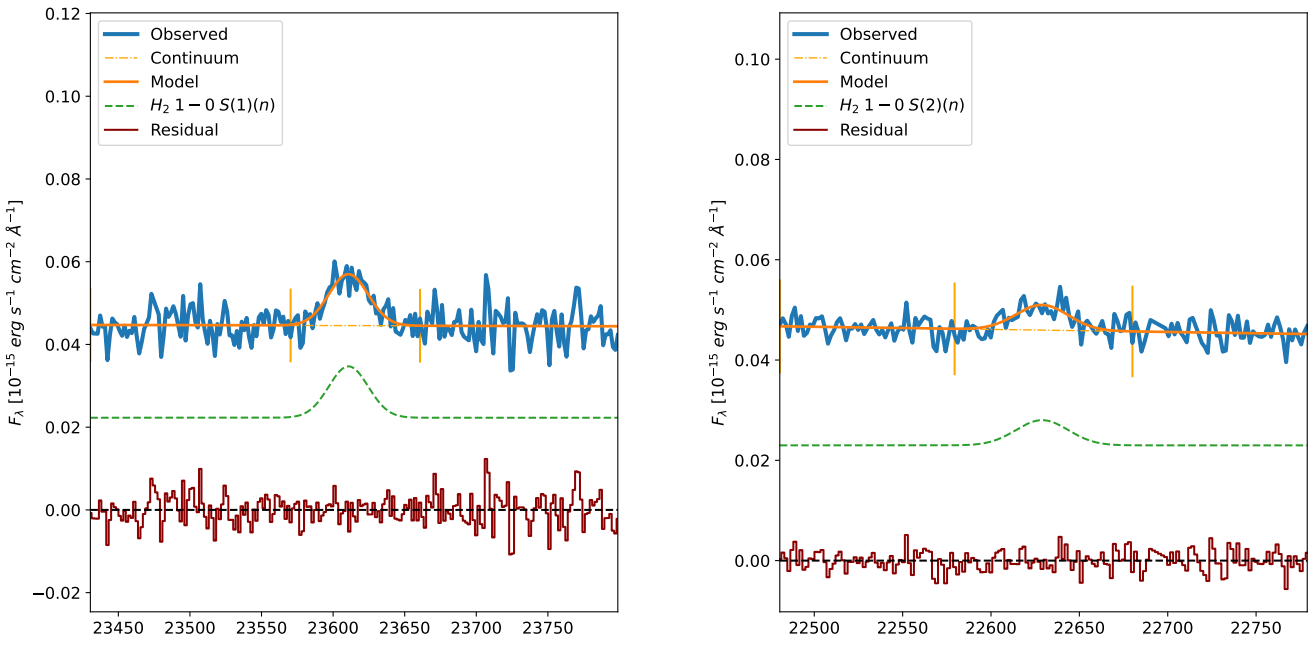

(a) Gaussian fit of H_2 $1-0$ $S(1)$.

(b) Gaussian fit of H_2 $1-0$ $S(2)$

Figure 35: Gaussian fits for the molecular lines H_2 $1-0$ $S(1)$ and H_2 $1-0$ $S(2)$ for the J1713+57 EMIR spectrum.

4.7 Discussion

Throughout the study of this subsample of objects, we have found gas components with disturbances that result in line widths of up to 2600 km/s in the most extreme case, while the detected moving gas components range in velocities from 70 km/s to 980 km/s. This shows the extreme variety of kinematics present in QSO2 outflows, as the driving mechanisms in conjunction with the different coupling efficiencies of said mechanisms result in phenomena that are almost particular to each galaxy, from only detecting blueshifted components to detections of both sides of a biconical outflow.

No clear warm molecular outflow is detected on any of these objects; while this result can be taken as it is at face value, it could also be attributed to the low signal generated by the molecular tracers, which is, for all the studied objects, considerably lower than that of the ionized lines. It is most definitely possible to detect warm molecular outflows using NIR observations, as was done for J1509 (C. Ramos et al., 2019 [23]) using the EMIR spectrum found in the Appendix. This low signal might mean that any potential broad components are blending into the AGN continuum, rendering them undetectable for the S/N levels of some of our spectra. This is accentuated by the fact that the warm component of molecular outflows represents a very small fraction of the total molecular gas in terms of mass, and as a direct consequence, also in terms of emission. We do, however, find a tentative detection of a warm molecular outflow in J1440+53, as a broad and redshifted component can be found in one of its molecular lines.

The next step is to estimate the outflow mass, outflow mass rate and kinetic energy from density and size measurements, which can be performed with the data at hand. The SDSS spectra can be used to estimate the electron density and reddening, and the EMIR spectra can be used to constrain the spatial extent of the outflow, leading to its full characterization.

5 Conclusions

When considering what the aims of this project would be, our approach was two-pronged: on the one hand, we aimed to reduce all the data from the 4 semesters used for observing the QSOFEED sample objects, transforming the raw data from EMIR into clean, usable spectra. This was achieved, as the entire sample was reduced, combined and flux calibrated. While a sample size of 40 objects might not seem too large, one has to take into consideration both the fact that every object observation is accompanied by a comparison star, and for each of these, two spectra were extracted. Add to this the relatively long reduction process required by NIR observations, and generating analysis-ready data turns out to be a very time-consuming procedure. The code developed in this project makes use of the Python implementation of IRAF as well as its *Lirisdr* package to turn the reduction process into a single code cell that only requires input at spectra extraction.

The reduced sample, viewable in the Appendix, contains high-resolution K-band spectra of 40 optically-selected QSO2 objects showing a variety of spectral features, both in the slope of the continuum and the numbers and shapes of emission lines. We observe objects with very few narrow emission lines and flat continua as well as objects with very rich spectra in terms of emission lines, broad emission components and sloped continua. While only 6 objects were studied in depth, a characterization of the entire sample would be desirable, as many of these objects show clear molecular lines and broad components.

The second aim of this project was to characterize the kinematics of outflowing gas in the observed QSO2s. A small subset of objects was chosen, all of which showed clear broad components in their ionized lines, as well as molecular emission lines. As such, we have shown the feasibility of simultaneously characterizing the ionized and warm molecular gas kinematics using NIR observations. To fully characterize the complete kinematics of these objects, complementary observations in millimeter wavelengths capable of tracing the cold molecular component would be ideal, as the warm-to-cold molecular gas mass ratio is an average rather than a constant throughout all QSO2s.

We utilize J0945+17, which has already been studied in the NIR using this same spectrum, to check the correctness of the procedure used to characterize the lines from the EMIR spectrum, while we can also compare the results from the study of J1034+60 in the optical range with the estimates obtained in this project. This same procedure is then used to analyse the remaining objects. We will now outline the general kinematic characteristics of these objects. The velocities reported are rough values used for comparison; for a more thorough examination, see the results section (4).

- For J0802+25 we report outflowing intermediate (FWHM $\sim$ 480 km/s, v $\sim$ 130 km/s) and broad (FWHM $\sim$ 1330 km/s, v $\sim$ -160 km/s) ionized components. Two other rapidly moving ionized gas components are detected, with intermediate widths. One of them moving toward our direction (FWHM $\sim$ 410 km/s, v $\sim$ -600 km/s), while the other moves away (FWHM $\sim$ 580 km/s, v $\sim$ 750 km/s km/s). Considering their uncertainty intervals, they appear to be the receding and approaching sides of a biconical outflow.

- For J0945+17 we confirm the reported outflow components, with both the intermediate (FWHM $\sim$ 830 km/s, v $\sim$ -150 km/s) and broad (FWHM $\sim$ 1340 km/s, v $\sim$ -260 km/s) ionized components outflowing. These findings are in line with those reported by Speranza et al., 2022 ([24]), for both the NIFS and EMIR observations.
- For J1034+60 we report two outflowing ionized gas components, both the intermediate (FWHM $\sim$ 600 km/s, v $\sim$ -70 km/s) and broad (FWHM $\sim$ 1500 km/s, v $\sim$ -190 km/s), while another component with close to intermediate width is detected moving away from us (FWHM $\sim$ 460 km/s, v $\sim$ 980 km/s).
- For J1440+53, we report a clear outflow for the broad ionized component (FWHM $\sim$ 1800 km/s, v $\sim$ -220 km/s), while the intermediate (FWHM $\sim$ 550 km/s) component's estimated velocity is very close to 0 for both spectra, and there are discrepancies among the different tracers, meaning no clear outflow is detected for the intermediate ionized gas component. We make a tentative detection of a warm molecular outflow (FWHM $\sim$ 440 km/s, v $\sim$ 150 km/s), although only a single line appears to trace this component and the uncertainties are of the magnitude of the measurement for both parameters.
- For J1455+32 we report both the intermediate (FWHM $\sim$ 740 km/s, v $\sim$ 100 km/s) and broad (FWHM $\sim$ 1200 km/s, v $\sim$ -100 km/s) ionized components to be clearly outflowing. The relative similarity in their widths and velocities suggest we are observing the receding and approaching sides of a biconical outflow.
- For J1713+57, the intermediate (FWHM $\sim$ 1200 km/s) and broad (FWHM $\sim$ 2600 km/s) ionized components appear to be moving very slowly in our line of sight, suggesting a very turbulent gas that doesn't appear to have a clear proper motion relative to our line of sight. This might imply an outflow occurring in the plane of the sky.

As previously discussed, no warm molecular outflows are clearly detected throughout the subsample, most likely due to the relatively low signal presented by these molecular lines. However, as proven in C. Ramos et al., 2019 ([23]), it is possible to detected warm molecular outflows using NIR spectra.

The continuation of this research, which is already underway, begins with the characterization of [SII] and [OIII] lines from the SDSS spectra; from their flux ratios it is possible to estimate the conditions of the different gas phases in terms of the electron density and electron temperature using *PyNeb* (Luridiana et al., 2014 [43]), and simultaneously estimate the electron density (which can be used for comparison) and reddening using a grid of photoionization models computed with *Cloudy* (Ferland et al., 2013[44]). The size of the outflow can be constrained even when performing long slit spectroscopy, and these parameters can be combined to obtain estimates of the outflow mass, the outflow mass rate and kinetic power, the latter of which we can compare to the total AGN power as its bolometric luminosity. The procedures followed to obtain these estimates as well as the conditions for considering an outflow as spatially resolved are described in detail in Rose et al., 2018 ([45]).

Once the entire subsample is characterized, there will still be another 34 objects to work with, a few of which show clear signs of hosting ionized outflows. The full characterization of the QSOFEED sample will hopefully lead to a better understanding of the role outflows play in AGN feedback, star formation and galaxy evolution as a whole.

References

[1] K. Schawinski, M. Koss, S. Berney, and L. F. Sartori, "Active galactic nuclei flicker: an observational estimate of the duration of black hole growth phases of $\sim 10^5$ yr," *Monthly Notices of the Royal Astronomical Society*, vol. 451, no. 3, pp. 2517–2523, 06 2015. [Online]. Available: https://doi.org/10.1093/mnras/stv1136

[2] C. K. Seyfert, "Nuclear Emission in Spiral Nebulae." *Astrophysical Journal*, vol. 97, p. 28, Jan. 1943.

[3] R. Reyes, N. L. Zakamska, M. A. Strauss, J. Green *et al.*, "Space density of optically selected type 2 quasars," *The Astronomical Journal*, vol. 136, no. 6, pp. 2373–2390, nov 2008.

[4] O. González-Martín, J. Masegosa, I. Márquez *et al.*, "An x-ray view of 82 liners with chandra and xmm-newton data," *Astronomy & Astrophysics*, vol. 506, no. 3, pp. 1107–1121, jul 2009. [Online]. Available: https://doi.org/10.1051%2F0004-6361%2F200912288

[5] R. J. McLure and M. J. Jarvis, "The relationship between radio luminosity and black hole mass in optically selected quasars," *Monthly Notices of the Royal Astronomical Society*, vol. 353, no. 4, pp. L45–L49, oct 2004. [Online]. Available: https://doi.org/10.1111%2Fj.1365-2966.2004.08305.x

[6] R. Antonucci, "Unified models for active galactic nuclei and quasars." *Annual Review of Astronomy and Astrophysics*, vol. 31, pp. 473–521, Jan. 1993.

[7] C. M. Urry and P. Padovani, "Unified schemes for radio-loud active galactic nuclei," *Publications of the Astronomical Society of the Pacific*, vol. 107, p. 803, sep 1995. [Online]. Available: https://doi.org/10.1086/133630

[8] Y.-C. Chen and C.-Y. Hwang, "Morphology of seyfert galaxies," *Astrophysics and Space Science*, vol. 362, 11 2017.

[9] J. Kormendy and L. C. Ho, "Coevolution (or not) of supermassive black holes and host galaxies," *Annual Review of Astronomy and Astrophysics*, vol. 51, no. 1, pp. 511–653, aug 2013. [Online]. Available: https://doi.org/10.1146%2Fannurev-astro-082708-101811

[10] F. Shankar, P. Salucci, G. L. Granato *et al.*, "Supermassive black hole demography: the match between the local and accreted mass functions," *Monthly Notices of the Royal Astronomical Society*, vol. 354, no. 4, pp. 1020–1030, 11 2004. [Online]. Available: https://doi.org/10.1111/j.1365-2966.2004.08261.x

[11] Y. Dubois, S. Peirani, C. Pichon *et al.*, "The horizon-AGN simulation: morphological diversity of galaxies promoted by AGN feedback," *Monthly Notices of the Royal Astronomical Society*, vol. 463, no. 4, pp. 3948–3964, sep 2016. [Online]. Available: https://doi.org/10.1093%2Fmnras%2Fstw2265

[12] B. McNamara and P. Nulsen, "Heating hot atmospheres with active galactic nuclei," *Annual Review of Astronomy and Astrophysics*, vol. 45, no. 1, pp. 117–175, sep 2007. [Online]. Available: https://doi.org/10.1146%2Fannurev.astro.45.051806.110625

[13] A. Fabian, "Observational evidence of active galactic nuclei feedback," *Annual Review of Astronomy and Astrophysics*, vol. 50, no. 1, pp. 455–489, sep 2012. [Online]. Available: https://doi.org/10.1146%2Fannurev-astro-081811-125521

[14] P. S. Bessiere and C. Ramos Almeida, "Spatially resolved evidence of the impact of quasar-driven outflows on recent star formation: the case of Mrk 34," *Monthly Notices of the Astronomical Royal Society*, vol. 512, no. 1, pp. L54–L59, May 2022.

[15] C. M. Harrison, T. Costa, C. N. Tadhunter *et al.*, "AGN outflows and feedback twenty years on," *Nature Astronomy*, vol. 2, no. 3, pp. 198–205, feb 2018. [Online]. Available: https://doi.org/10.1038%2Fs41550-018-0403-6

[16] R. Tanner and K. A. Weaver, "Simulations of AGN-driven galactic outflow morphology and content," *The Astronomical Journal*, vol. 163, no. 3, p. 134, feb 2022. [Online]. Available: https://doi.org/10.3847%2F1538-3881%2Fac4d23

[17] F. Fiore, C. Feruglio, F. Shankar, M. Bischetti, A. Bongiorno, M. Brusa, S. Carniani, C. Cicone, F. Duras, A. Lamastra, V. Mainieri, A. Marconi, N. Menci, R. Maiolino, E. Piconcelli, G. Vietri, and L. Zappacosta, "AGN wind scaling relations and the co-evolution of black holes and galaxies," *Astronomy & Astrophysics*, vol. 601, p. A143, may 2017. [Online]. Available: https://doi.org/10.1051%2F0004-6361%2F201629478

[18] A. Fluetsch, R. Maiolino, S. Carniani *et al.*, "Properties of the multiphase outflows in local (ultra)luminous infrared galaxies," *Monthly Notices of the Royal Astronomical Society*, vol. 505, no. 4, pp. 5753–5783, jun 2021. [Online]. Available: https://doi.org/10.1093%2Fmnras%2Fstab1666

[19] C. R. Almeida and C. Ricci, "Nuclear obscuration in active galactic nuclei," *Nature*, 2017. [Online]. Available: https://arxiv.org/abs/1709.00019

[20] D. S. N. Rupke and S. Veilleux, "BREAKING THE OBSCURING SCREEN: A RESOLVED MOLECULAR OUTFLOW IN a BURIED QSO," *The Astrophysical Journal*, vol. 775, no. 1, p. L15, sep 2013. [Online]. Available: https://doi.org/10.1088%2F2041-8205%2F775%2F1%2Fl15

[21] M. Villar-Martín, E. Bellocchi, J. Stern *et al.*, "Deconstructing the narrow-line region of the nearest obscured quasar," *Monthly Notices of the Royal Astronomical Society*, vol. 454, no. 1, pp. 439–456, sep 2015. [Online]. Available: https://doi.org/10.1093%2Fmnras%2Fstv1864

[22] C. Ramos Almeida, J. Piqueras López, M. Villar-Martín, and P. S. Bessiere, "An infrared view of AGN feedback in a type-2 quasar: the case of the Teacup galaxy," *Monthly Notices of the Royal Astronomical Society*, vol. 470, no. 1, pp. 964–976, Sep. 2017.

[23] C. R. Almeida, J. A. Acosta-Pulido, C. N. Tadhunter *et al.*, "A near-infrared study of the multiphase outflow in the type-2 quasar j1509+0434," *Monthly Notices of the Royal Astronomical Society: Letters*, vol. 487, no. 1, pp. L18–L23, may 2019. [Online]. Available: https://doi.org/10.1093%2Fmnrasl%2Fslz072

[24] G. Speranza, C. Ramos Almeida, J. Acosta Pulido *et al.*, "Warm molecular and ionized gas kinematics in the type-2 quasar J0945+1737," *Submitted to Astronomy & Astrophysics*, 2022.

[25] M. E. Jarvis, C. M. Harrison, A. P. Thomson *et al.*, "Prevalence of radio jets associated with galactic outflows and feedback from quasars," *Monthly Notices of the Royal Astronomical Society*, vol. 485, no. 2, pp. 2710–2730, feb 2019. [Online]. Available: https://doi.org/10.1093%2Fmnras%2Fstz556

[26] G. Speranza, B. Balmaverde, A. Capetti *et al.*, "The MURALES survey. iv. searching for nuclear outflows in 3c radio galaxies at z $<$ 0.3 with muse observations," *Astronomy & Astrophysics*, vol. 653, p. A150, sep 2021. [Online]. Available: https://doi.org/10.1051%2F0004-6361%2F202140686

[27] Emonts, B. H. C., Colina, L., Piqueras-López, J. *et al.*, "Outflows of hot molecular gas in ultra-luminous infrared galaxies mapped with vlt-sinfoni," *A&A*, vol. 607, p. A116, 2017. [Online]. Available: https://doi.org/10.1051/0004-6361/201731508

[28] M. R. Blanton, M. A. Bershady, B. Abolfathi *et al.*, "Sloan Digital Sky Survey IV: Mapping the Milky Way, Nearby Galaxies, and the Distant Universe," *Astronomical Journal*, vol. 154, no. 1, p. 28, Jul. 2017.

[29] T. M. Heckman, G. Kauffmann, J. Brinchmann *et al.*, "Present-day growth of black holes and bulges: The sloan digital sky survey perspective," *The Astrophysical Journal*, vol. 613, no. 1, pp. 109–118, sep 2004. [Online]. Available: https://doi.org/10.1086%2F422872

[30] C. Ramos Almeida, M. Bischetti, S. García-Burillo *et al.*, "The diverse cold molecular gas contents, morphologies, and kinematics of type-2 quasars as seen by ALMA," *Astronomy & Astrophysics*, vol. 658, p. A155, Feb. 2022.

[31] F. Garzón, D. Abreu, S. Barrera *et al.*, "EMIR: the GTC NIR multi-object imager-spectrograph," in *Ground-based and Airborne Instrumentation for Astronomy*, I. S. McLean and M. Iye, Eds., vol. 6269, International Society for Optics and Photonics. SPIE, 2006, pp. 421 – 430. [Online]. Available: https://doi.org/10.1117/12.671302

[32] F. Garzón, N. Castro-Rodríguez, M. Insausti *et al.*, "Results of the verification of the NIR MOS EMIR," in *Ground-based and Airborne Instrumentation for Astronomy V*, S. K. Ramsay, I. S. McLean, and H. Takami, Eds., vol. 9147, International Society for Optics and Photonics. SPIE, 2014, pp. 304 – 313. [Online]. Available: https://doi.org/10.1117/12.2054804

[33] S. Moehler, A. Modigliani, W. Freudling *et al.*, "Flux calibration of medium-resolution spectra from 300 nm to 2500 nm: Model reference spectra and telluric correction," *Astronomy & Astrophysics*, vol. 568, p. A9, Aug. 2014.

[34] A. Smette, H. Sana, S. Noll *et al.*, "Molecfit: A general tool for telluric absorption correction," *Astronomy & Astrophysics*, vol. 576, p. A77, apr 2015. [Online]. Available: https://doi.org/10.1051%2F0004-6361%2F201423932

[35] T. P. Robitaille, E. J. Tollerud, P. Greenfield *et al.*, "Astropy: A community Python package for astronomy," *Astronomy & Astrophysics*, vol. 558, p. A33, Oct. 2013.

[36] A. M. Price-Whelan, B. M. Sipőcz, H. M. Günther *et al.*, "The Astropy Project: Building an Open-science Project and Status of the v2.0 Core Package," *Astronomical Journal*, vol. 156, no. 3, p. 123, Sep. 2018.

[37] M. S. Dimitrijevic, L. C. Popovic, J. Kovacevic *et al.*, "The flux ratio of the [o III] 5007, 4959 lines in AGN: comparison with theoretical calculations," *Monthly Notices of the Royal Astronomical Society*, vol. 374, no. 3, pp. 1181–1184, jan 2007. [Online]. Available: https://doi.org/10.1111%2Fj.1365-2966.2006.11238.x

[38] J. Pierce, C. Tadhunter, C. Ramos Almeida *et al.*, "Galaxy interactions are the dominant trigger for local type 2 quasars," *Submitted to Monthly Notices of the Royal Astronomical Society*, 2022.

[39] S. Alam, F. D. Albareti, C. A. Prieto *et al.*, "THE ELEVENTH AND TWELFTH DATA RELEASES OF THE SLOAN DIGITAL SKY SURVEY: FINAL DATA FROM SDSS-III," *The Astrophysical Journal Supplement Series*, vol. 219, no. 1, p. 12, jul 2015. [Online]. Available: https://doi.org/10.1088%2F0067-0049%2F219%2F1%2F12

[40] K. N. Abazajian, J. K. Adelman-McCarthy, M. A. Agüeros *et al.*, "The seventh data release of the sloan digital sky survey," *The Astrophysical Journal Supplement Series*, vol. 182, no. 2, pp. 543–558, may 2009. [Online]. Available: https://doi.org/10.1088%2F0067-0049%2F182%2F2%2F543

[41] P. S. Bessiere and C. R. Almeida, "Spatially resolved evidence of the impact of quasar-driven outflows on recent star formation: the case of mrk 34," *Monthly Notices of the Royal Astronomical Society: Letters*, vol. 512, no. 1, pp. L54–L59, feb 2022. [Online]. Available: https://doi.org/10.1093%2Fmnrasl%2Fslac016

[42] H. Aihara, C. A. Prieto, D. An *et al.*, "THE EIGHTH DATA RELEASE OF THE SLOAN DIGITAL SKY SURVEY: FIRST DATA FROM SDSS-III," *The Astrophysical Journal Supplement Series*, vol. 193, no. 2, p. 29, mar 2011. [Online]. Available: https://doi.org/10.1088%2F0067-0049%2F193%2F2%2F29

[43] V. Luridiana, C. Morisset, and R. A. Shaw, "PyNeb: a new tool for analyzing emission lines," *Astronomy & Astrophysics*, vol. 573, p. A42, dec 2014. [Online]. Available: https://doi.org/10.1051%2F0004-6361%2F201323152

[44] G. J. Ferland, R. L. Porter, P. A. M. van Hoof *et al.*, "The 2013 release of cloudy," 2013. [Online]. Available: https://arxiv.org/abs/1302.4485

[45] M. Rose, C. Tadhunter, C. R. Almeida *et al.*, "Quantifying the AGN-driven outflows in ULIRGs (QUADROS) – i: VLT/xshooter observations of nine nearby objects," *Monthly Notices of the Royal Astronomical Society*, vol. 474, no. 1, pp. 128–156, oct 2017. [Online]. Available: https://doi.org/10.1093%2Fmnras%2Fstx2590

Appendix: Sample spectra

This appendix includes the calibrated spectra for all observations spanning from May of 2018 to June of 2020. Every figure includes, in the upper panel, the reference star spectrum used for flux calibration and telluric correction, and in the lower panel, the QSO2 spectrum. The objects are ordered in accordance to their observation blocks, beginning with 2018A and ending with 2020A.

Some commonly observed lines are included in the upper part of the QSO2's spectrum to help better understand the characteristics of the object. The object spectra are not corrected for telluric absorption; its effects can be seen in both the reference stars and objects spectra.

2018A

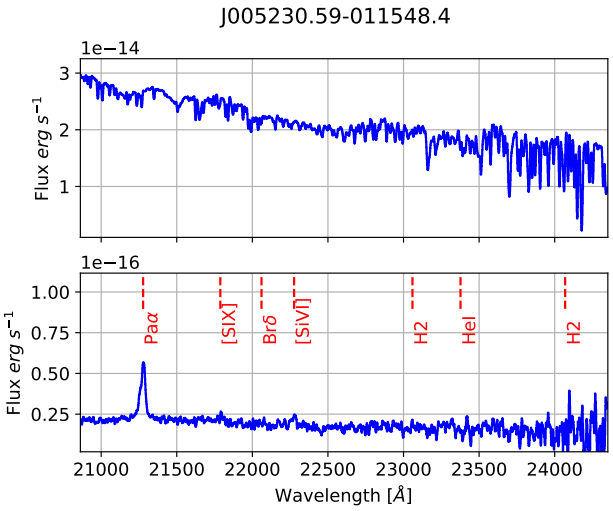

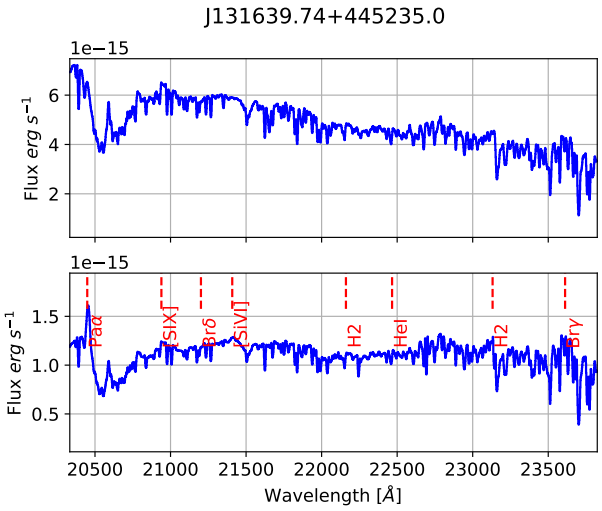

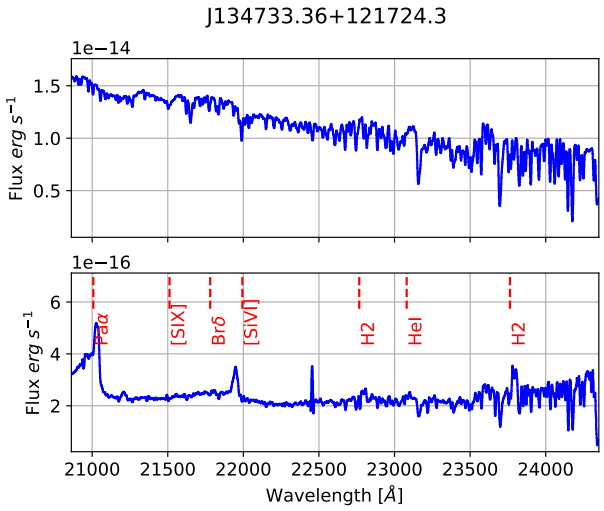

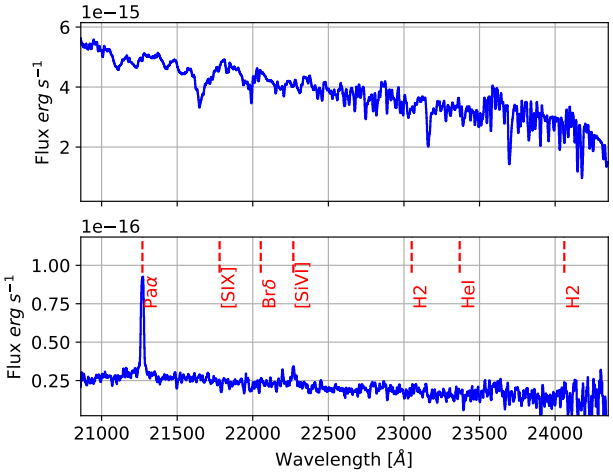

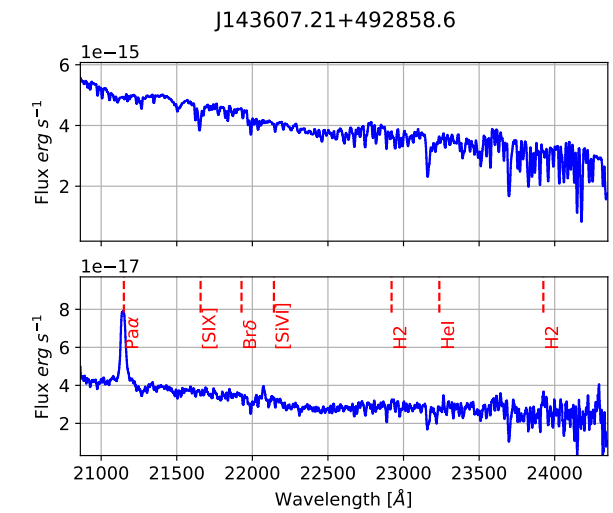
J143607.21+492858.6
1e−15
Flux erg s⁻¹
1e−17
Paα
[SIX]
Brδ
[SiVI]
H2
HeI
H2
Wavelength [Å]

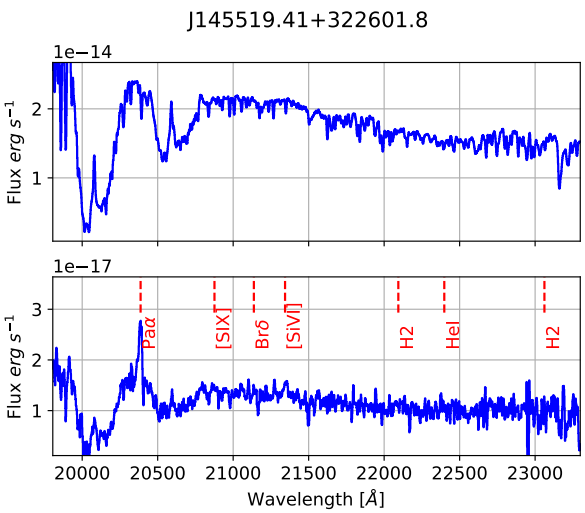
J145519.41+322601.8
1e−14
Flux erg s⁻¹
1e−17
Paα
[SIX]
Brδ
[SiVI]
H2
HeI
H2
Wavelength [Å]

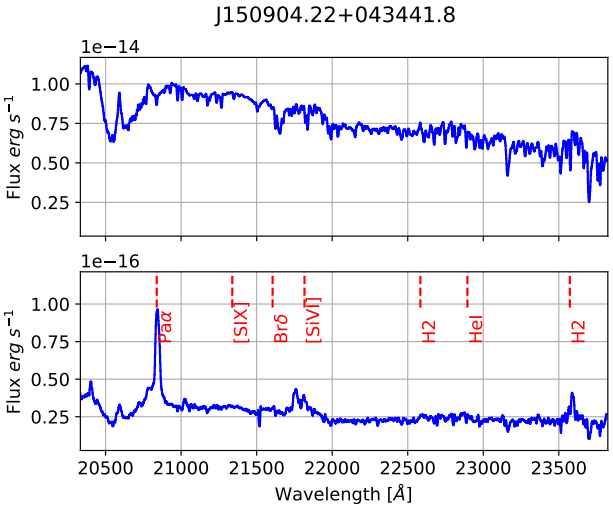
J150904.22+043441.8
1e−14
Flux erg s⁻¹
1e−16
Paα
[SIX]
Brδ
[SiVI]
H2
HeI
H2
Wavelength [Å]

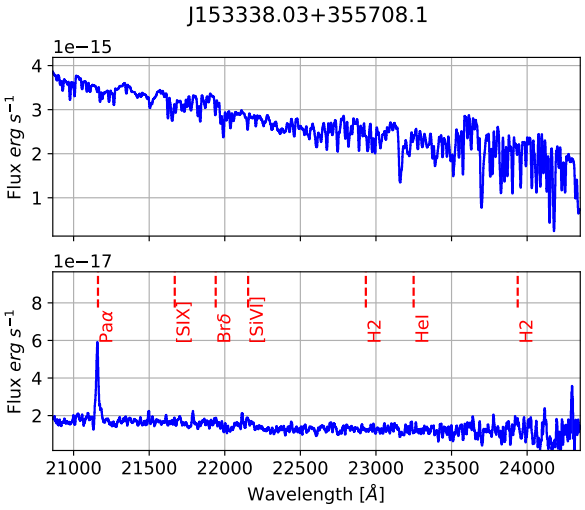
J153338.03+355708.1
1e−15
Flux erg s⁻¹
1e−17
Paα
[SIX]
Brδ
[SiVI]
H2
HeI
H2
Wavelength [Å]

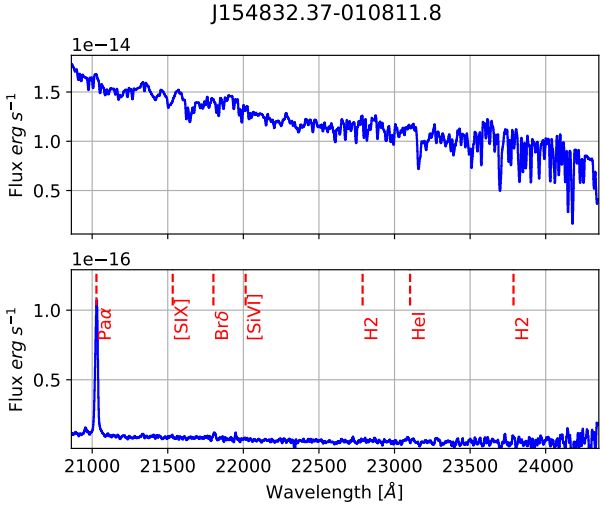
J154832.37-010811.8
1e−14
Flux erg s⁻¹
1e−16
Paα
[SIX]
Brδ
[SiVI]
H2
HeI
H2
Wavelength [Å]

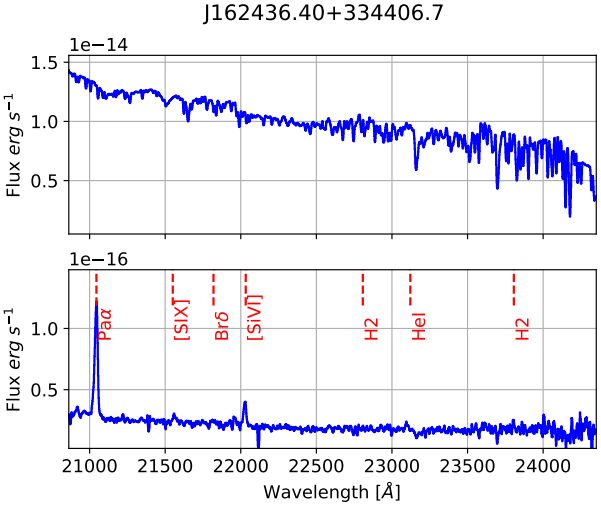
J162436.40+334406.7
1e−14
Flux erg s⁻¹
1e−16
Paα
[SIX]
Brδ
[SiVI]
H2
HeI
H2
Wavelength [Å]

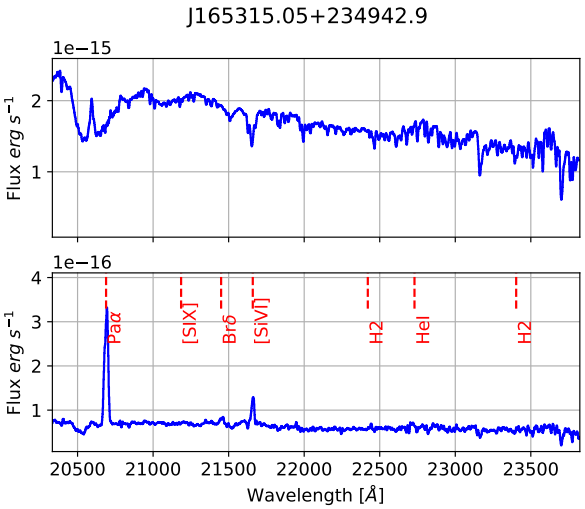
J165315.05+234942.9
1e−15
Flux erg s⁻¹
1e−16
Paα
[SIX]
Brδ
[SiVI]
H2
HeI
H2
Wavelength [Å]

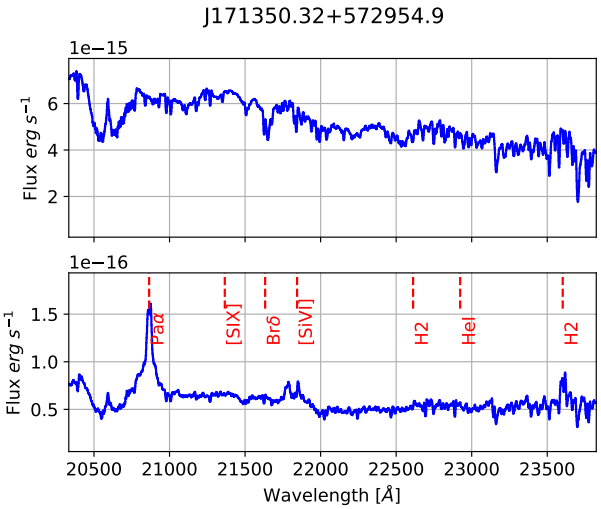
J171350.32+572954.9
1e−15
Flux erg s⁻¹
1e−16
Paα
[SIX]
Brδ
[SiVI]
H2
HeI
H2
Wavelength [Å]

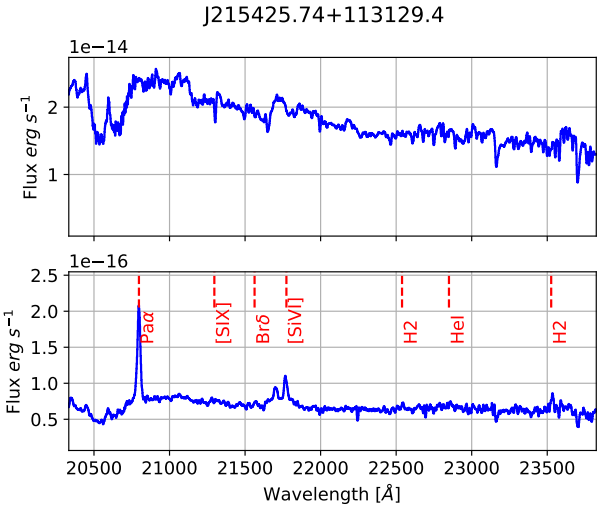
J215425.74+113129.4
1e−14
Flux erg s⁻¹
1e−16
Paα
[SIX]
Brδ
[SiVI]
H2
HeI
H2
Wavelength [Å]

2018B

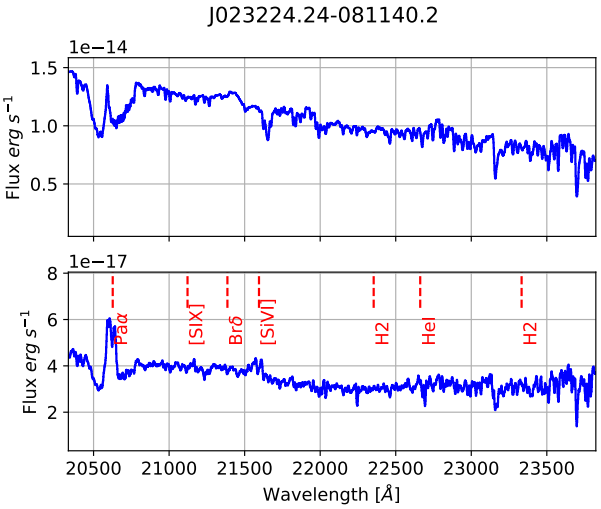
J023224.24-081140.2
1e−14
Flux erg s⁻¹
1e−17
Paα
[SIX]
Brδ
[SiVI]
H2
HeI
H2
Wavelength [Å]

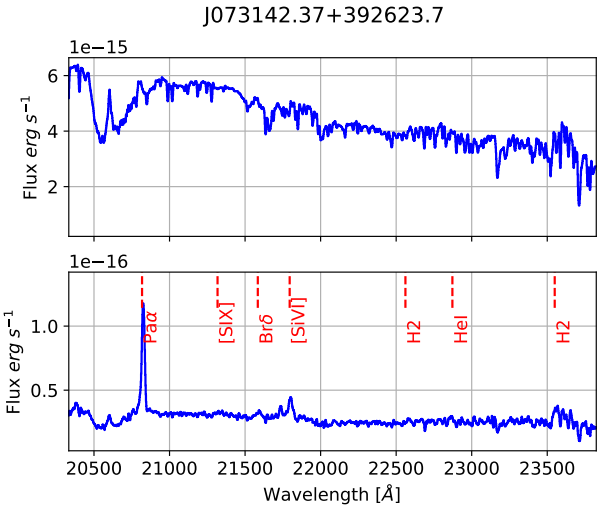
J073142.37+392623.7
1e−15
Flux erg s⁻¹
1e−16
Paα
[SIX]
Brδ
[SiVI]
H2
HeI
H2
Wavelength [Å]

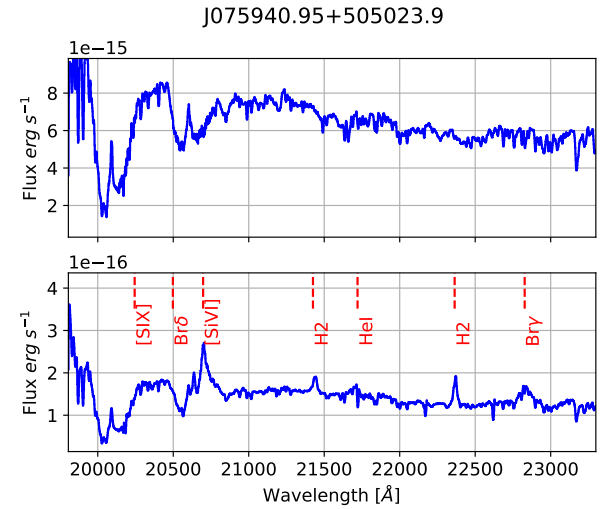
J075940.95+505023.9
1e−15
Flux erg s⁻¹
1e−16
[SIX]
Brδ
[SiVI]
H2
HeI
H2
Brγ
Wavelength [Å]

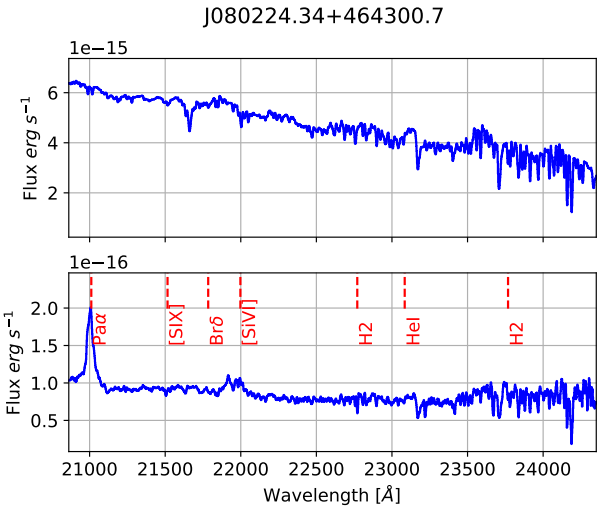
J080224.34+464300.7
1e−15
Flux erg s⁻¹
1e−16
Paα
[SIX]
Brδ
[SiVI]
H2
HeI
H2
Wavelength [Å]

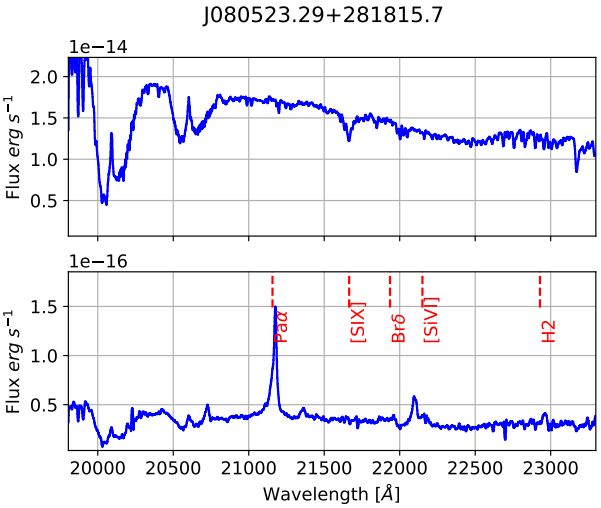
J080523.29+281815.7
1e−14
Flux erg s⁻¹
1e−16
Paα
[SIX]
Brδ
[SiVI]
H2
Wavelength [Å]

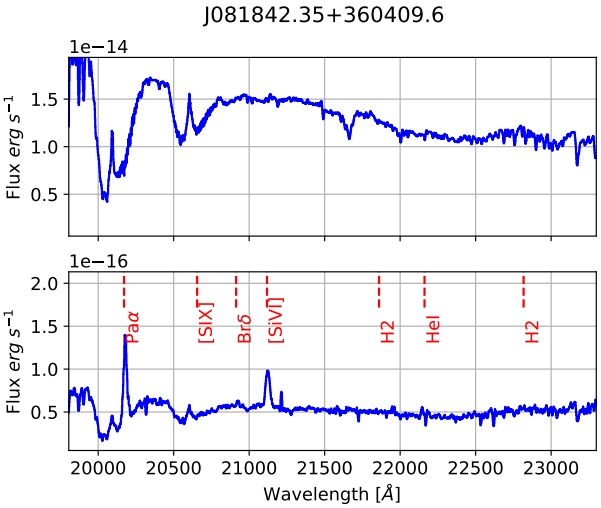
J081842.35+360409.6
1e−14
Flux erg s⁻¹
1e−16
Paα
[SIX]
Brδ
[SiVI]
H2
HeI
H2
Wavelength [Å]

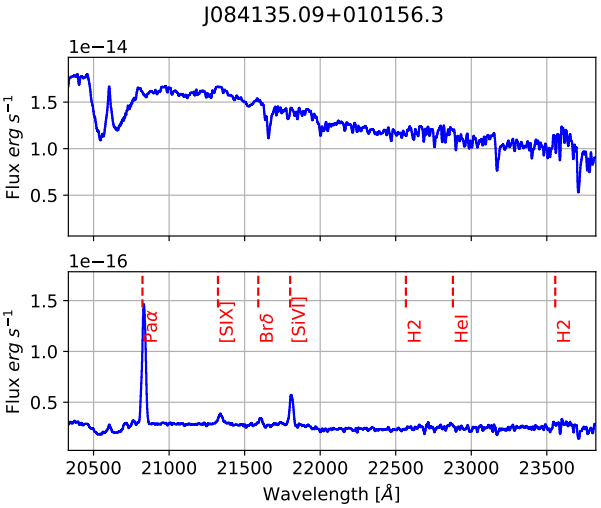
J084135.09+010156.3
1e−14
Flux erg s⁻¹
1e−16
Paα
[SIX]
Brδ
[SiVI]
H2
HeI
H2
Wavelength [Å]

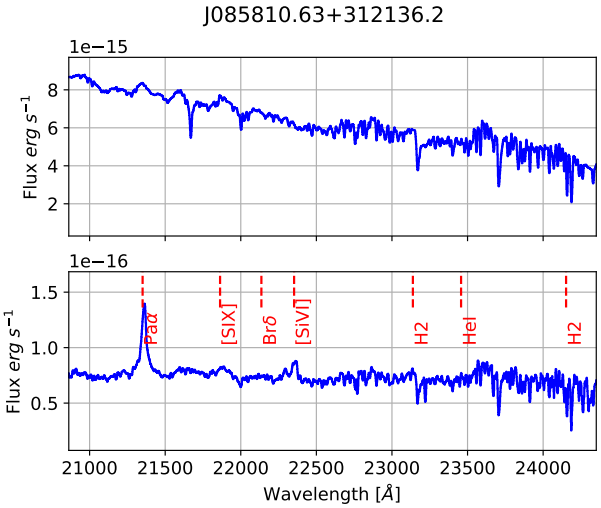
J085810.63+312136.2
1e−15
Flux erg s⁻¹
1e−16
Paα
[SIX]
Brδ
[SiVI]
H2
HeI
H2
Wavelength [Å]

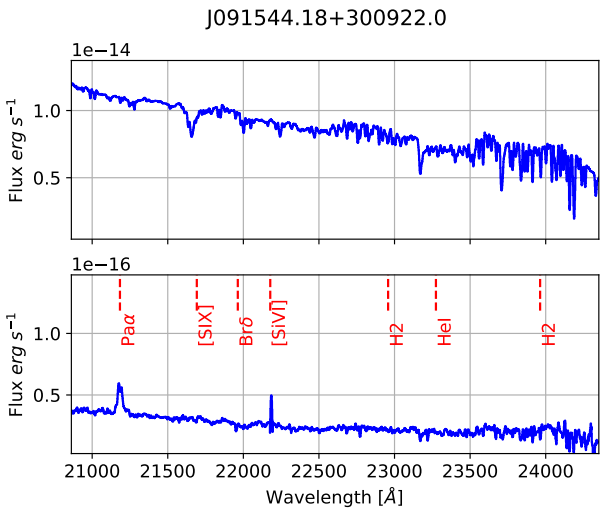
J091544.18+300922.0
1e−14
Flux erg s⁻¹
1e−16
Flux erg s⁻¹
Paα
[SiX]
Brδ
[SiVI]
H2
HeI
H2
21000 21500 22000 22500 23000 23500 24000
Wavelength [Å]

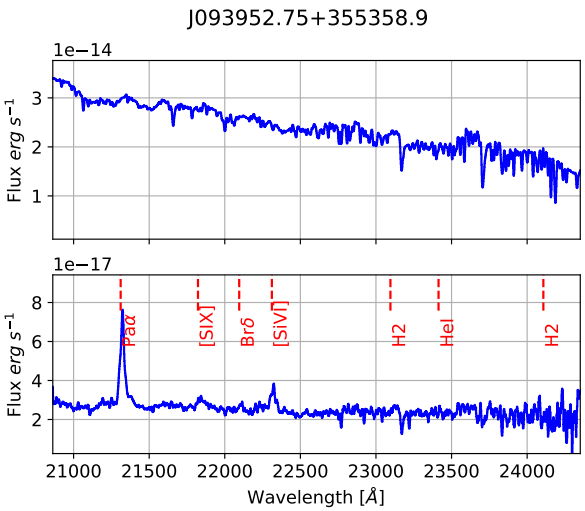
J093952.75+355358.9
1e−14
Flux erg s⁻¹
1e−17
Flux erg s⁻¹
Paα
[SiX]
Brδ
[SiVI]
H2
HeI
H2
21000 21500 22000 22500 23000 23500 24000
Wavelength [Å]

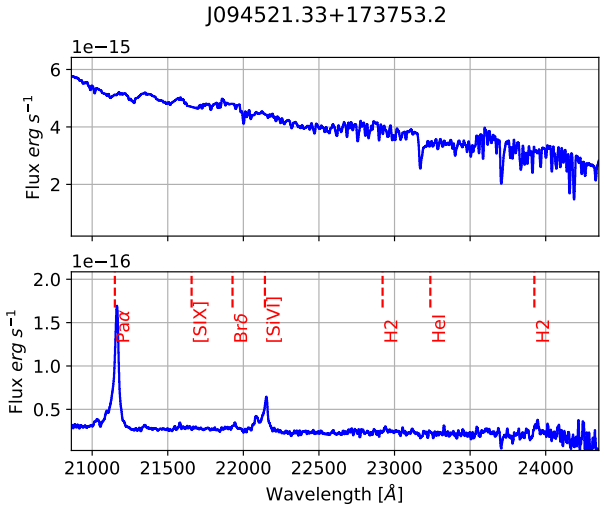
J094521.33+173753.2
1e−15
Flux erg s⁻¹
1e−16
Flux erg s⁻¹
Paα
[SiX]
Brδ
[SiVI]
H2
HeI
H2
21000 21500 22000 22500 23000 23500 24000
Wavelength [Å]

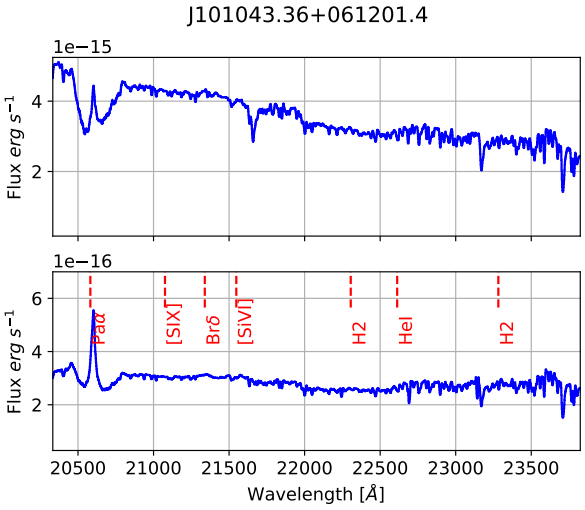
J101043.36+061201.4
1e−15
Flux erg s⁻¹
1e−16
Flux erg s⁻¹
Paα
[SiX]
Brδ
[SiVI]
H2
HeI
H2
20500 21000 21500 22000 22500 23000 23500
Wavelength [Å]

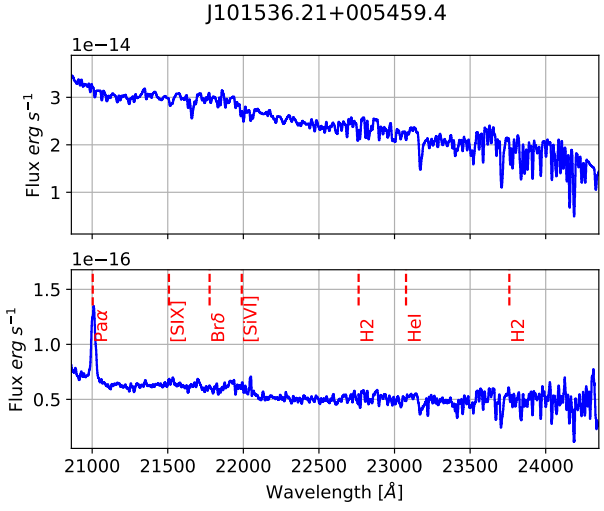
J101536.21+005459.4
1e−14
Flux erg s⁻¹
1e−16
Flux erg s⁻¹
Paα
[SiX]
Brδ
[SiVI]
H2
HeI
H2
21000 21500 22000 22500 23000 23500 24000
Wavelength [Å]

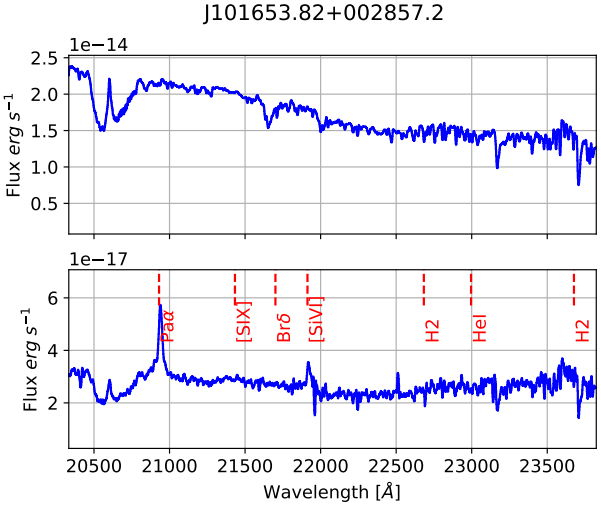
J101653.82+002857.2
1e−14
Flux erg s⁻¹
1e−17
Flux erg s⁻¹
Paα
[SiX]
Brδ
[SiVI]
H2
HeI
H2
20500 21000 21500 22000 22500 23000 23500
Wavelength [Å]

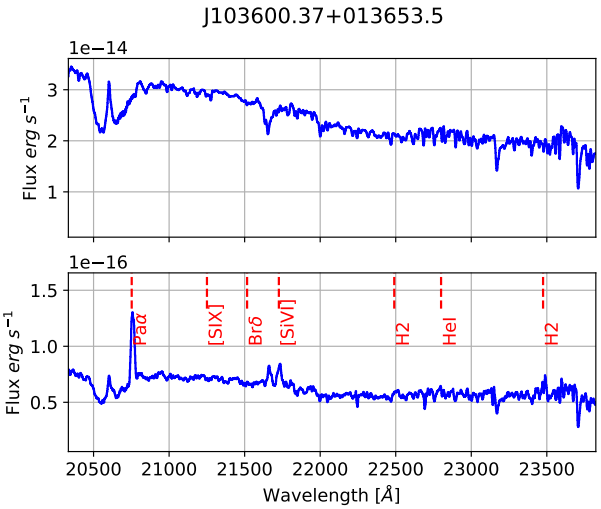
J103600.37+013653.5
1e−14
Flux erg s⁻¹
1e−16
Paα
[SIX]
Brδ
[SiVI]
H2
HeI
H2
Wavelength [Å]

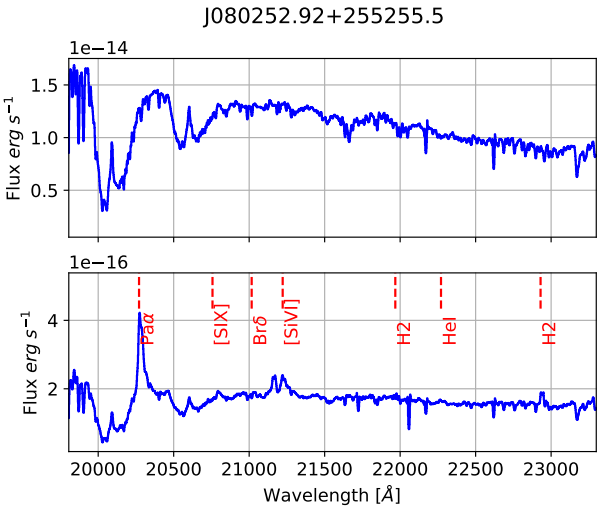
J080252.92+255255.5
1e−14
Flux erg s⁻¹
1e−16
Paα
[SIX]
Brδ
[SiVI]
H2
HeI
H2
Wavelength [Å]

2019A

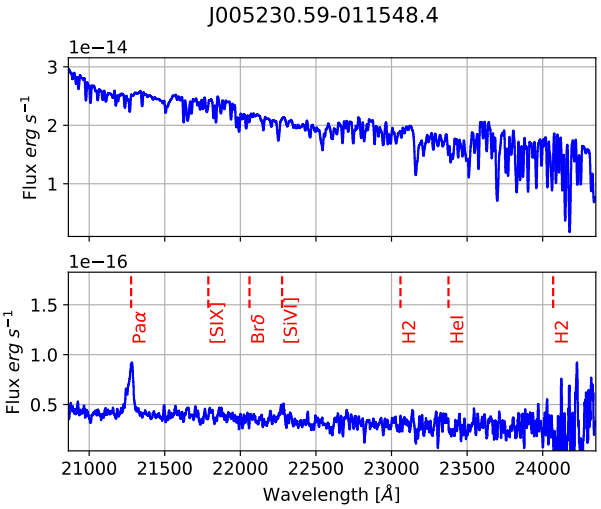
J005230.59-011548.4
1e−14
Flux erg s⁻¹
1e−16
Paα
[SIX]
Brδ
[SiVI]
H2
HeI
H2
Wavelength [Å]

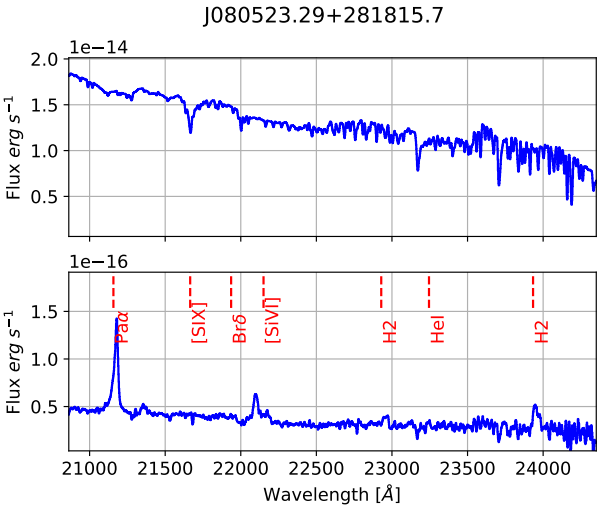
J080523.29+281815.7
1e−14
Flux erg s⁻¹
1e−16
Paα
[SIX]
Brδ
[SiVI]
H2
HeI
H2
Wavelength [Å]

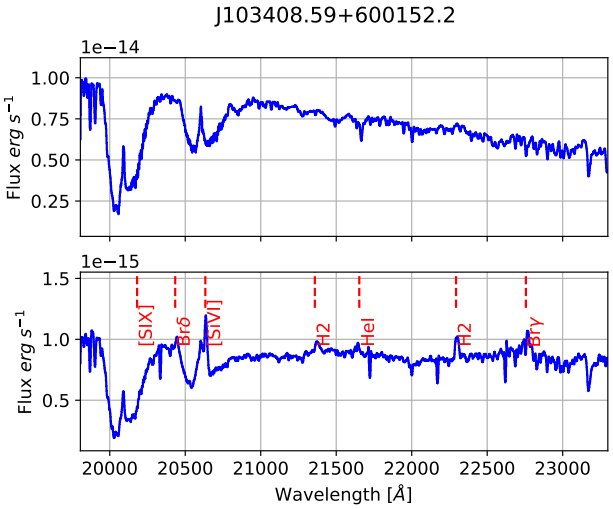
J103408.59+600152.2
1e−14
Flux erg s⁻¹
1e−15
[SIX]
Brδ
[SiVI]
H2
HeI
H2
BrγWavelength [Å]

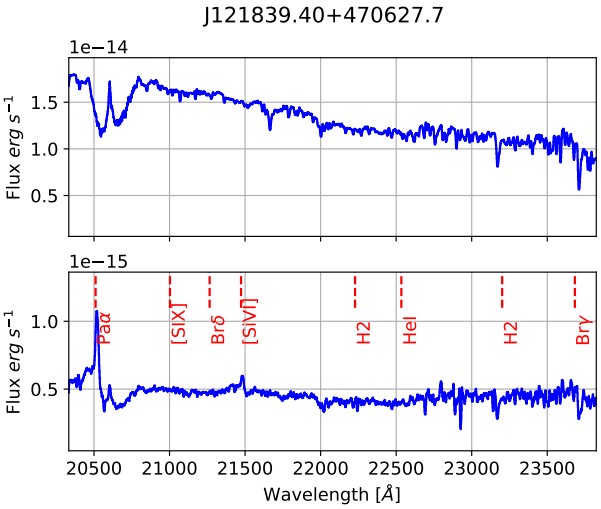
J121839.40+470627.7
1e−14
Flux erg s⁻¹
1e−15
Paα
[SIX]
Brδ
[SiVI]
H2
HeI
H2
BrγWavelength [Å]

J135617.79-023101.5

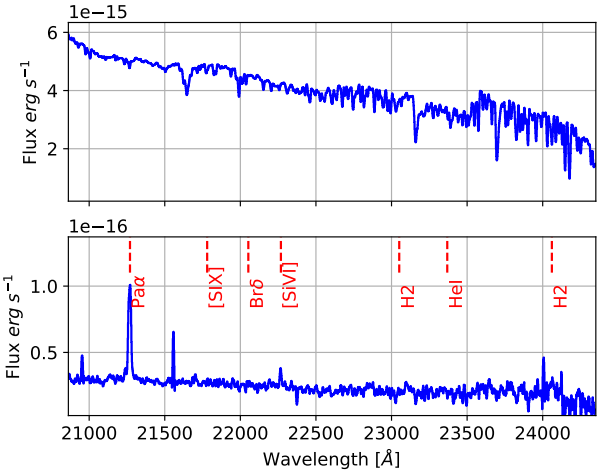

J140541.21+402632.6

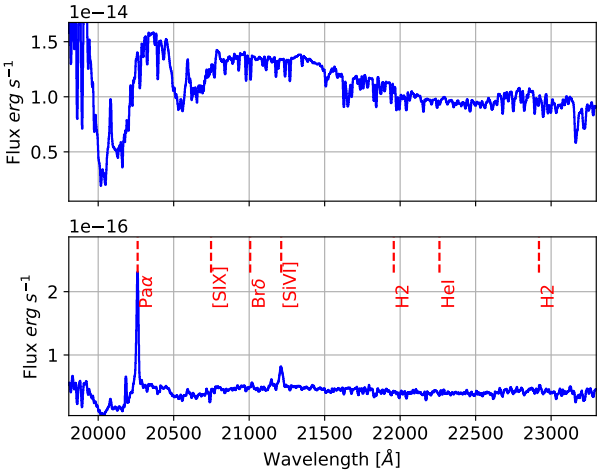

J143607.21+492858.6

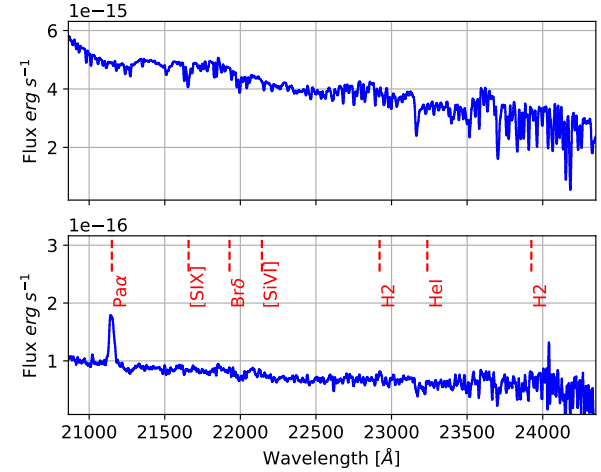

J143737.85+301101.1

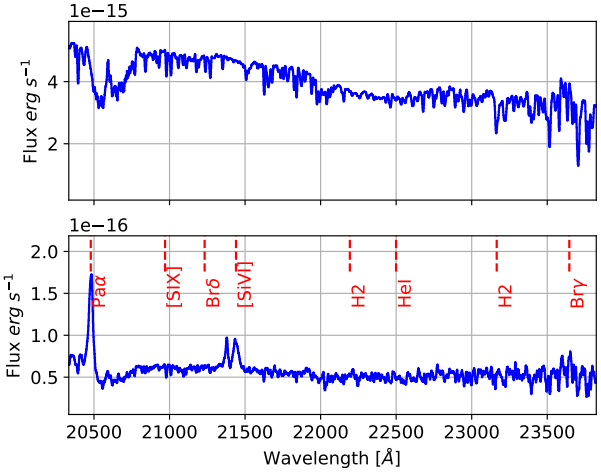

J144038.10+533015.9

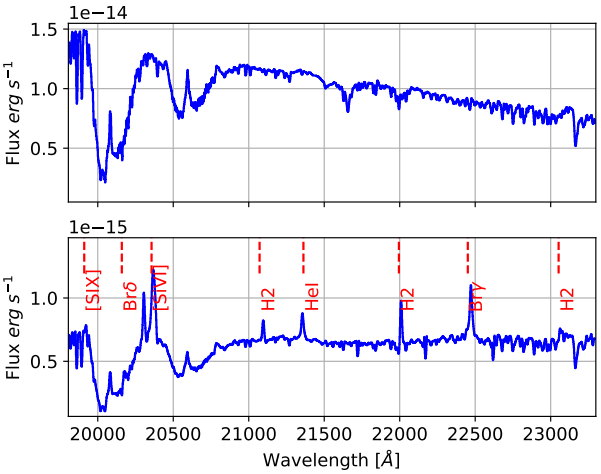

J145519.41+322601.8

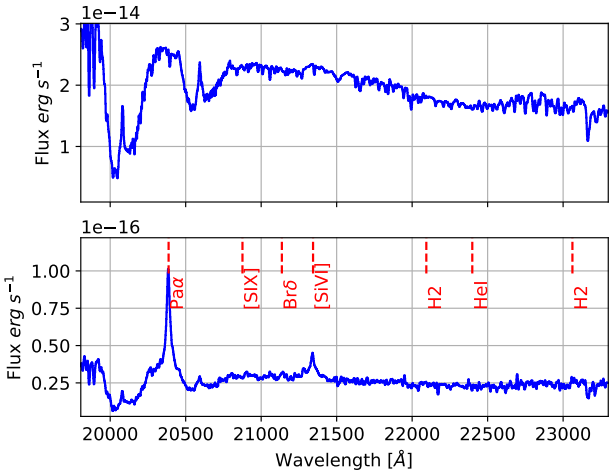

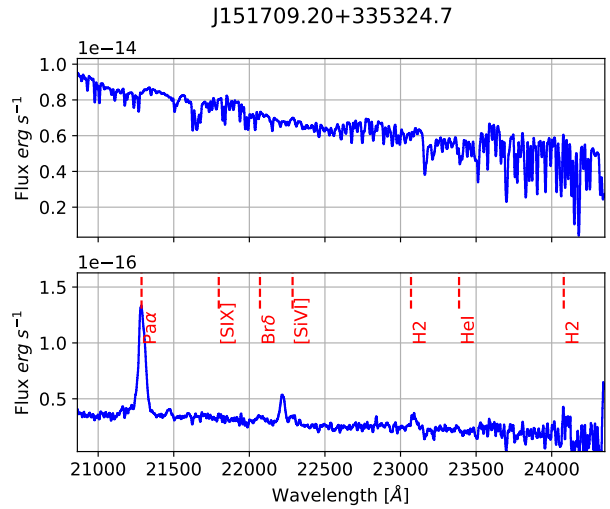
J151709.20+335324.7
1e−14
Flux erg s⁻¹
1e−16
Paα
[SiX]
Brδ
[SiVI]
H2
HeI
H2
Wavelength [Å]

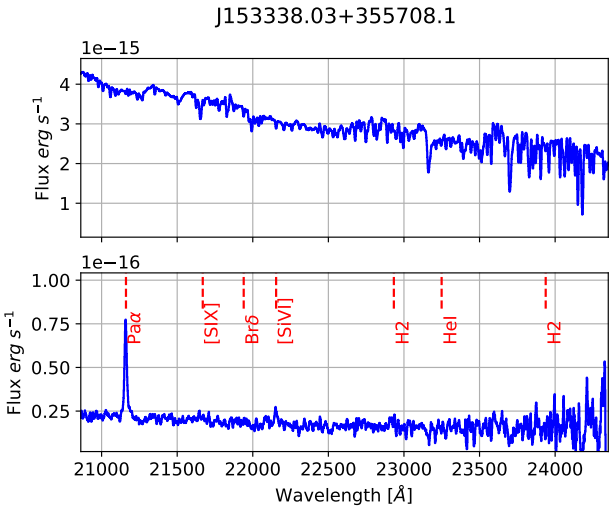
J153338.03+355708.1
1e−15
Flux erg s⁻¹
1e−16
Paα
[SiX]
Brδ
[SiVI]
H2
HeI
H2
Wavelength [Å]

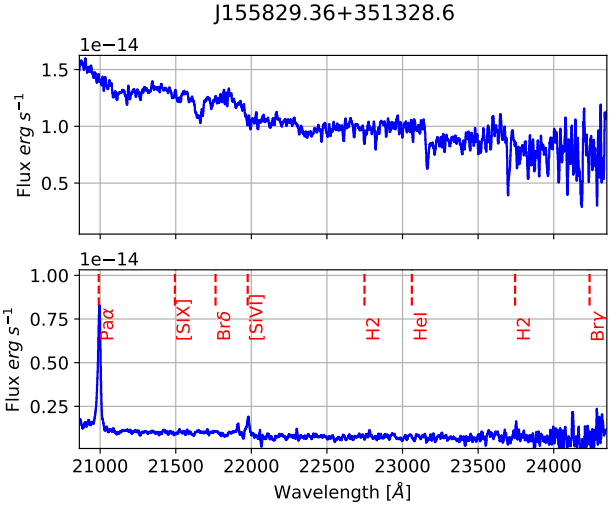
J155829.36+351328.6
1e−14
Flux erg s⁻¹
1e−14
Paα
[SiX]
Brδ
[SiVI]
H2
HeI
H2
Bry
Wavelength [Å]

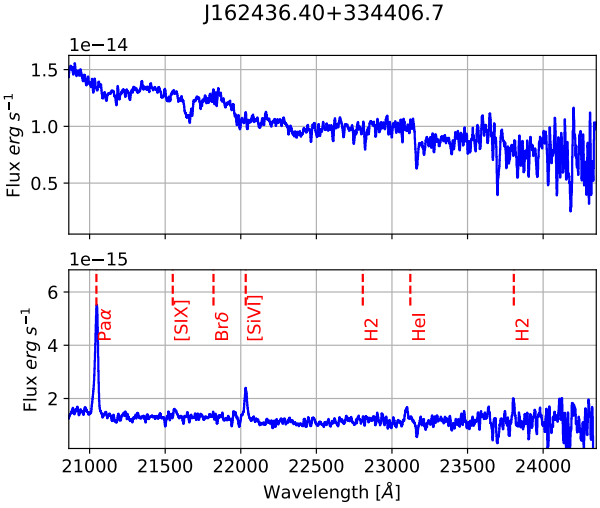
J162436.40+334406.7
1e−14
Flux erg s⁻¹
1e−15
Paα
[SiX]
Brδ
[SiVI]
H2
HeI
H2
Wavelength [Å]

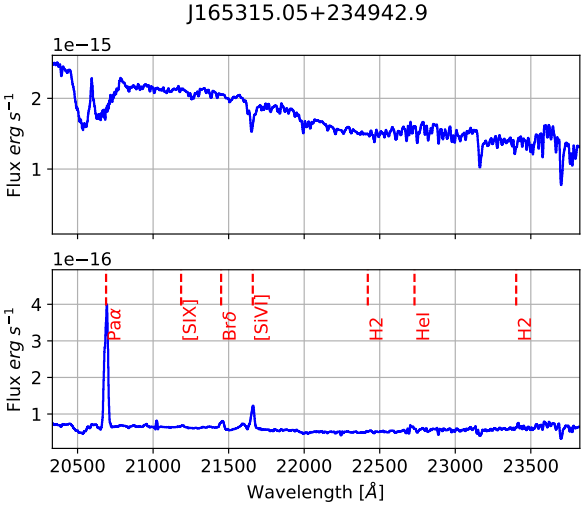
J165315.05+234942.9
1e−15
Flux erg s⁻¹
1e−16
Paα
[SiX]
Brδ
[SiVI]
H2
HeI
H2
Wavelength [Å]

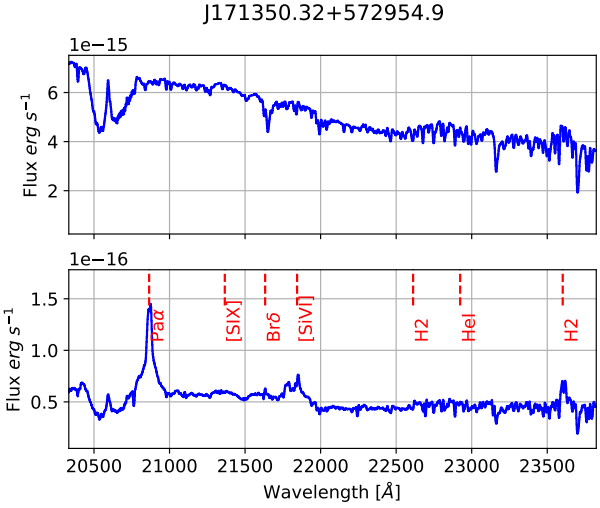
J171350.32+572954.9
1e−15
Flux erg s⁻¹
1e−16
Paα
[SiX]
Brδ
[SiVI]
H2
HeI
H2
Wavelength [Å]

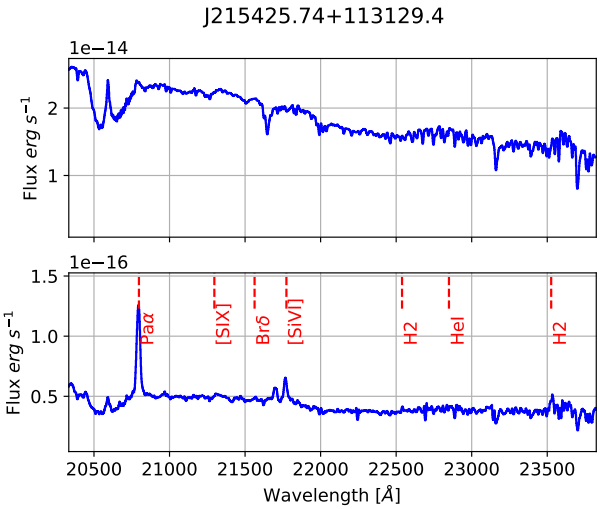
J215425.74+113129.4
1e−14
Flux erg s−1
1e−16
Flux erg s−1
Paα
[SIX]
Brδ
[SiVI]
H2
HeI
H2
Wavelength [Å]

2020A

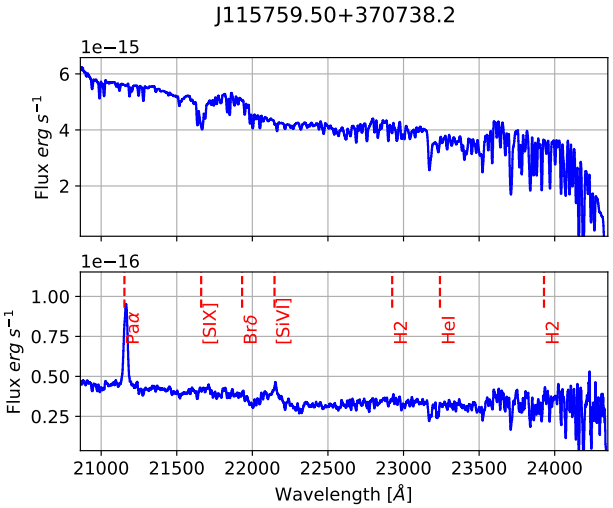
J115759.50+370738.2
1e−15
Flux erg s−1
1e−16
Flux erg s−1
Paα
[SIX]
Brδ
[SiVI]
H2
HeI
H2
Wavelength [Å]

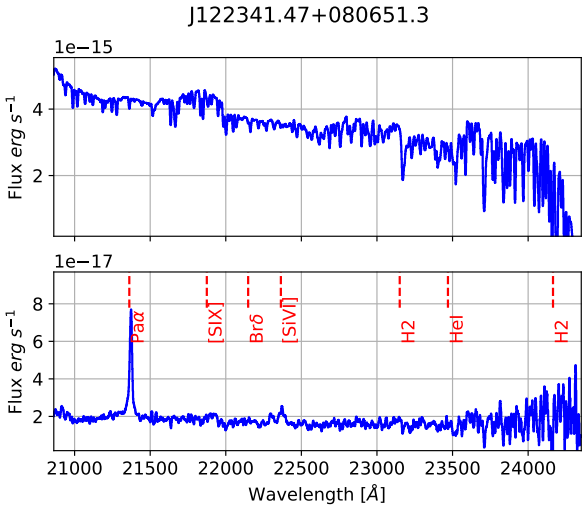
J122341.47+080651.3
1e−15
Flux erg s−1
1e−17
Flux erg s−1
Paα
[SIX]
Brδ
[SiVI]
H2
HeI
H2
Wavelength [Å]

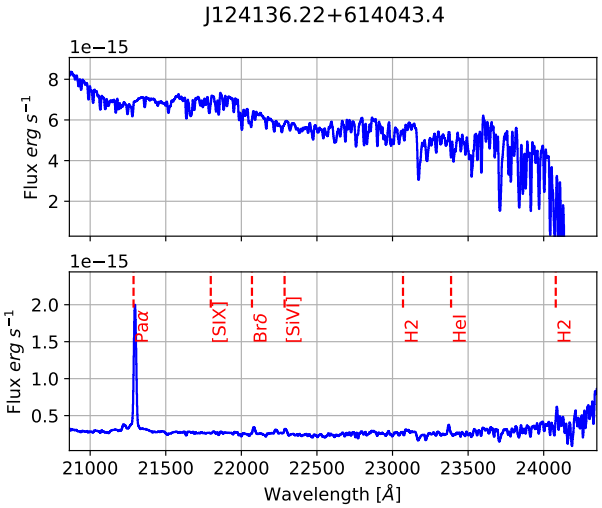
J124136.22+614043.4
1e−15
Flux erg s−1
1e−15
Flux erg s−1
Paα
[SIX]
Brδ
[SiVI]
H2
HeI
H2
Wavelength [Å]

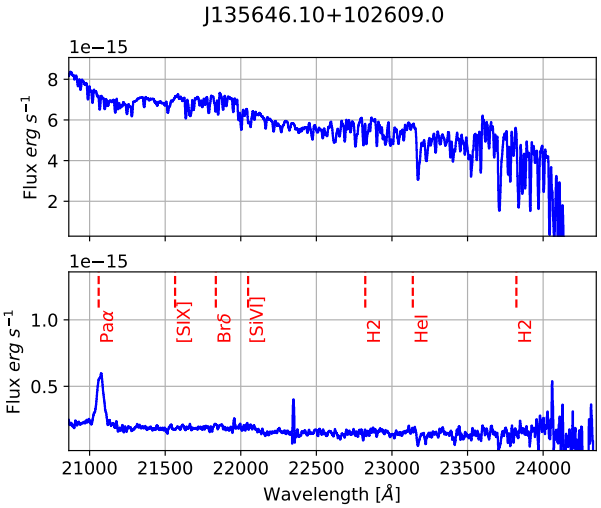
J135646.10+102609.0
1e−15
Flux erg s−1
1e−15
Flux erg s−1
Paα
[SIX]
Brδ
[SiVI]
H2
HeI
H2
Wavelength [Å]